

University of Nevada, Reno

**Thermal Behavior of the TN-32B Spent Nuclear Fuel Cask under Storage and Vacuum Drying Conditions**

A dissertation submitted in partial fulfillment of the requirements for the degree of Doctor of Philosophy in  
Mechanical Engineering

by

Megan Higley

Dr. Mustafa Hadj-Nacer/Dissertation Advisor

August, 2024



THE GRADUATE SCHOOL

We recommend that the dissertation  
prepared under our supervision by

**Megan Higley**

entitled

**Thermal Behavior of the TN-32B Spent Nuclear Fuel Cask under  
Storage and Vacuum Drying Conditions**

be accepted in partial fulfillment of the  
requirements for the degree of

**Doctor of Philosophy**

Mustafa Hadj-Nacer, Ph.D.  
*Advisor*

Miles Greiner, Ph.D.  
*Co-advisor*

Yan Wang, Ph.D.  
*Committee Member*

Dev Chidambaram, Ph.D.  
*Committee Member*

Nicholas Tsoufanidis, Ph.D.  
*Graduate School Representative*

Markus Kemmelmeier, Ph.D., Dean  
*Graduate School*

August, 2024

## ABSTRACT

In this work, computational models are developed to predict the temperatures in a spent fuel cask under storage and vacuum drying conditions. In particular, the TN-32 spent nuclear fuel cask was modeled because it is one of the few demonstration casks with publicly available experimental data to validate computational models for storage and vacuum drying conditions. Computational fluid dynamics models of this cask were developed to investigate common modeling techniques, assumptions, and uncertainties to identify and quantify their effects on temperature predictions.

Two-dimensional and three-dimensional models of the TN-32 spent nuclear fuel cask are constructed and simulated in the ANSYS package for comparison with experimental data. The gaps between the cask components were found to have a strong influence on assembly temperatures. The size of these gaps is unknown due to the potential shifting of fuel and cask components, manufacturing tolerancing, and thermal expansion. During vacuum drying, the effect of rarefaction at the helium-solid interfaces caused significant temperature increases in the fuel region. This effect is strongly dependent on pressure, gas species, and gap sizes, which are all unknown during the vacuum drying process.

This dissertation was divided into three main sections, each one is a stand-alone journal paper. In the first paper, two-dimensional detailed models of the TN-32B were used to investigate different peripheral basket/rail gap geometries and their effect on temperatures under storage and vacuum drying conditions. The basket/rail gap is explicitly modeled to have three different widths, 0 mm, 2.54 mm, and 4.78 mm. The basket and fuel assemblies are also explicitly shifted within the model to investigate two leaning geometries where the basket contacts one or two sides. Fuel region temperatures are shown to be very sensitive to gap width

and pressure with vacuum drying induced rarefaction potentially causing as much as a 51°C increase in fuel region temperatures.

In the second paper, full homogenous three-dimensional models were developed and used to conduct an uncertainty quantification (UQ) analysis of the collective and individual effects of nine gaps, between solid components in the TN-32B, on temperature prediction. A global UQ method that uses the Latin Hypercube Sampling technique is used to quantify uncertainty in temperature prediction due to uncertainty in gap widths at all locations of internal temperature measurement in the TN-32B from the High Burnup Demonstration cask. Results indicate that the effects of different gaps are location-dependent with the total effect ranging from  $\pm 12^\circ\text{C}$  to  $\pm 21^\circ\text{C}$  and that uncertainty in the basket/rail gap accounts for approximately 50% of all uncertainty in temperature predictions due to uncertainty in gap widths.

In the third and final paper, a one-eighth three-dimensional model of the TN-32B is constructed with a detailed representation of the fuel assemblies. The same computational mesh was used to generate a homogenous model, with the fuel regions represented as porous heat-generating blocks. An assembly-of-interest fuel region heat loading that allows for reasonable comparisons with experimental data is proposed and used in the simulations. Effective thermal and flow properties for homogenous model were derived from sub-models. The temperature and flow velocity predictions were compared on a point-to-point basis between the detailed and homogenous models throughout the fuel region. The temperatures at 63 locations obtained from the detailed model are compared to data from the High Burnup Demonstration project and the results showed a difference ranging from  $-7^\circ\text{C}$  to  $+10^\circ\text{C}$ . The homogenous model accurately predicts temperatures relative to the detailed model, with the most notable differences observed

at lower elevations within the fuel regions. 95% of fuel region temperatures are within 2°C between the models.

## ACKNOWLEDGEMENTS

First and foremost, I want to thank my advisor, Dr. Hadj-Nacer. He's been a gentle encourager of my success through the years. He presented opportunities that I wasn't sure that I would be able to achieve, but he insisted I could. His belief drove many of the first and last steps of this work. Dr. Hadj-Nacer has always taken the time and effort to guide my understanding and has given me tools I will continue to use in my future work. None of this would have been possible without Dr. Hadj-Nacer and I will forever be grateful to have been his student.

I want to thank Dr. Greiner, my co-advisor, for opening my view of this work. Not only did Dr. Greiner provide some of the foundational ideas and concepts of this work, but he always provided a viewpoint much different than my natural inclination. This viewpoint has led to a much deeper analysis and understanding of the work.

I want to thank Dr. Tsoulfanidis for introducing me to nuclear science and engineering. His calm and casual style of teaching made the subject accessible and interesting. I will always be thankful for the opportunity I had to learn from him. I want to thank Dr. Chidambaram and Dr. Wang for being a part of this committee, for managing funding of this work, and for their support of this work.

I want to thank my parents for their constant love and support. Their emphasis on hard work and education started far before any of this work and provided a foundation on which I could rely. I want to thank my family for their encouragement and for reminding me what I am capable of.

I met some of the most wonderful people during this time. Cody, Austin, and Bruno have the most unselfish commitment to making the people around them feel better. Ashish, Subin, Thulani, and Saeed exemplified a personal resilience, but also a willingness to support others.

Frank and Brandon guided me toward valuable ideas, demonstrated the importance of seeing things through, and could always be relied upon. Iffat, Tan, Burak, and Greg showed me a deep commitment to friendship with remarkable openness and familiarity. Lily and Laura were the pillars of reason and provided me with countless moments of laughter.

## TABLE OF CONTENTS

<b>Chapter 1: Introduction .....</b>	<b>1</b>
<b>Chapter 2: Effect of basket/rail gap on temperature prediction in the TN-32 cask under storage and drying conditions.....</b>	<b>6</b>
1. Introduction.....	8
2. Two-dimensional computational model .....	13
a. Geometric Variations.....	15
i. Centered Basket Configurations.....	16
ii. Shifted Basket Configurations.....	16
3. Computational methods .....	17
a. Vacuum Drying Modeling.....	19
4. Simulation Results .....	22
a. Centered Basket Configurations .....	25
b. Peak Cladding and Surface Temperatures.....	30
5. Summary and Conclusions .....	33
<b>Chapter 3: Uncertainty quantification of thermal gap widths on internal temperatures in the TN-32B HBU demo cask .....</b>	<b>41</b>
1. Introduction.....	44
2. Computational Model and Boundary Conditions .....	47
a. Thermal Gaps .....	52
3. Results.....	55
a. Nominal Configuration .....	56
b. Effects of Uncertainties.....	63
i. Uncertainty Quantification Methods.....	63
ii. Best-Estimate Temperature Predictions .....	65
4. Summary and Conclusions .....	74
<b>Chapter 4: Detailed and Homogenous Modeling of the TN-32B Spent Nuclear Fuel Demo Cask.....</b>	<b>80</b>
1. Introduction.....	83
2. Computational Model .....	87
3. Simulation Conditions .....	91
a. Homogenous Model Properties.....	94
4. Results.....	97

a. Detailed Model Results and Comparison with Experimental Data.....	97
b. Comparison of Homogenous and Detailed Model Results .....	106
5. Conclusion .....	112
<b>Chapter 5: Summary and Conclusions.....</b>	<b>118</b>

## List of Tables

Table 3.1. Thermal gaps considered in this work (illustrated in Fig. 2) with their assigned number, description, abbreviation, fill gas, and maximum width.....	54
Table 4.1. Porous flow coefficients of the homogenous fuel region.....	96

## List of Figures

Figure 2.1. TN-32 DSC cross-section model color coded by material. Detailed views showing basket/rail gaps and mesh are included. ....	14
Figure 2.2. Simulated temperature contours for average gap width $W = 4.78$ mm. The common temperature scale and five-pointed stars at the hottest locations are included. Left-side $P = 223$ kPa and right-side $P = 100$ Pa.....	23
Figure 2.3. Centered-basket internal temperature profiles along the $x$ -axis. (a) Nominal gap width ( $W = 4.78$ mm) for $P = 0.1, 0.4$ and $223$ kPa. (b) Continuum conditions ( $P = 223$ kPa) with $W = 0, 2.54$ and $4.78$ mm and representation of Eq. 4. ....	27
Figure 2.4. Centered-basket component temperature difference versus gap width for different pressures (a) Gap temperature difference. (b) Basket temperature difference.....	29
Figure 2.5. Peak cladding temperature versus average gap width for three internal pressures. The solid and open symbols show centered-basket and shifted-basket results, respectively. The open symbols with an “X” in the center are for the side-shifted configuration, while the completely open symbols are for the diagonal-shifted configuration. ....	31
Figure 2.6. Surface temperature variation versus basket displacement for three internal pressures for all average wall spacings considered in this work. ....	33
Figure 3.1. TN-32B SNF cask 3D model showing components, internal thermocouple locations, mesh, and coordinate system from (a) vertical and (b) horizontal cross-sections. ...	48
Figure 3.2. Heat generation rates and numbering convention for each of the 32 fuel assemblies of the HBU project cask. Instrumented fuel assemblies are highlighted.....	51
Figure 3.3. Details of (a) Region 1 and (b) Region (2) shown in Fig. 1, depicting the nine gaps considered in this study.....	53

Figure 3.4. Simulation temperature at three thermocouple locations versus iteration for the nominal configuration. Dashed and dotted lines show the average temperature within two sample sets. ....	57
Figure 3.5. Temperature contours for the nominal gap configuration in the (a) B-B and (b) A-A planes shown in Fig. 1 at iteration 350.....	59
Figure 3.6. 3D Axial velocity plot with a temperature contour overlay at iteration 350 in the A-A plane shown in Fig. 1 for the nominal gap configuration for (a) all open regions and (b) only fuel regions. ....	61
Figure 3.7. Comparison of the temperature predictions between simulations with and without natural convection at all thermocouple locations for the nominal configuration. Error bars represent the iterative uncertainties. ....	63
Figure 3.8. Simulated and experimental temperature profiles for assemblies a) 2, b) 6, c) 14, and d) 28. The solid line is for simulation results and the dotted line is for experimental results. The simulation and experimental uncertainties are shown with error bars.....	66
Figure 3.9. Best-estimate simulated temperatures as a function of experimental temperatures.....	68
Figure 3.10. Iterative, gap, and total temperature uncertainties as a function of best estimate temperatures.....	70
Figure 3.11. Linear regression model temperature prediction as a function of CFD simulation temperature for all gap configurations and thermocouple locations.....	72
Figure 3.12. Contribution to temperature uncertainty of selected gaps at selected assemblies.....	74
Figure 4.1. Color-coded computational domain of the TN-32B detailed model. (a) Isometric	

view of the 3D model with a detailed region of drain holes, and (b) a horizontal cross-section with a detailed region showing the mesh. Indicators of the axial position of the thermocouples in the instrumented assemblies are shown in (a). .....	89
Figure 4.2. Heat generation rates and labeling scheme for (a) the HBU demonstration cask loading, (b) symmetric one-eighth loading used to approximate the HBU loading, and (c) normalized axial heat generation profile. The instrumented assemblies are highlighted in (a).	93
Figure 4.3. (a) Radial effective thermal conductivity and (b) axial effective thermal conductivity of the homogenous fuel regions. ....	95
Figure 4.4. Detailed model predicted temperature profiles compared with experimentally measured temperatures along the instrumented assemblies. ....	98
Figure 4.5. Temperature residual from the experimental data for the (a) detailed model with natural convection, and (b) detailed model without natural convection. ....	99
Figure 4.6. Assembly and supporting rail mass flow rates versus radial distance for the detailed and homogenous models. ....	101
Figure 4.7. Mid-plane ( $z = 2.134$ m) axial velocity profiles for (a) the detailed and (b) the homogenous models. ....	103
Figure 4.8. Point-to-point comparison of temperature predicted by the detailed model without natural convection versus temperature predicted by the detailed model with natural convection. ....	105
Figure 4.9. Contours of the temperature difference between the detailed and homogenous models at three axial locations, (a) bottom ( $z = -0.007$ m), (b) middle ( $z = 2.134$ m), and (c) top ( $z = 3.745$ m). ....	108
Figure 4.10. Domain point-to-point temperature comparison between detailed and	

homogenous models..... 110

Figure 4.11. Probability distribution functions for each fuel region component (fuel, cladding, or gas), for both model types (detailed and homogenous). ..... 112

## **FUNDING**

This work was supported by the U.S. Department of Energy Office of Nuclear Energy University Program under award number DE-NE0008713 and by the United States Nuclear Regulatory Commission (NRC) under Contract NRC-HQ-84-16-G-0033. Ms. Nancy Hebron-Israel serves as the NRC award program manager.

# Chapter 1: Introduction

---

Spent nuclear fuel (SNF) assemblies discharged from light water reactors consist of highly radioactive, heat-generating fuel pellets stacked inside long sealed zircaloy cladding tubes that are held in square arrays by spacer plates (Saling and Fentiman 2001). When SNF assemblies are first removed from a reactor, they are stored in a water-filled pool while their heat generation rate and radioactivity decrease. After sufficient time (typically a few years), several SNF assemblies may be moved to a dry storage cask (DSC) (Areva 2002), or other packaging. To transfer the SNF, the DSC is lowered into the pool and the SNF is loaded into square-cross-section tubes of a support basket within the DSC containment region. It is then covered, lifted out of the pool, and drained. Moisture remaining in the internal crevices and surfaces after draining must be removed to reduce the risk of future corrosion and/or flammable gas formation (Miller et al. 2013).

The most common method to remove moisture from SNF packages is vacuum drying (Miller et al. 2013; Large 1999). During this process, the package's internal pressure is reduced in stages to as low as 0.067 kPa to promote water evaporation and vapor diffusion out of the system (Large 1999). A sealed package is considered dry when it can maintain a pressure of less than 0.4 kPa for 30 minutes. After drying, the package is typically filled with helium or another non-oxidizing gas to pressures between 100 and 800 kPa and sealed. It may then be stored on-site or transported to another location.

The peak cladding temperature,  $T_{PC}$ , is the maximum allowable temperature the cladding material that surrounds the fuel may experience and is one of the most commonly investigated parameters, because it is a strong indication of cask performance.

During all normal post-reactor operations, the  $T_{PC}$  and temperatures of specific package components must be maintained below specified limits (NRC 2003, 2010). Package component temperatures may experience their highest temperatures while or soon after being transferred to a dry package, because it is the first time the SNF is not directly water-cooled, and its heat generation rate is still relatively high. Additionally, the low pressures employed during vacuum drying may cause the gas in the narrow gaps to become rarefied (Bird 1983; Hadj-Nacer et al. 2017). This can reduce conduction heat transfer at the gas-solid interfaces and eliminate natural convection, which increases internal temperatures compared to non-rarefied (continuum) conditions.

Computational fluid dynamics (CFD) simulations have been used to predict  $T_{PC}$  and other component temperatures and their uncertainties in a variety of package designs to assure they do not exceed required limits for a range of fuel heat generation rates and storage conditions. These simulations model conduction within package solid components, as well as surface-to-surface radiation, conduction, and natural convection heat transfer across gas-filled regions, assuming the gas acts as a continuum. In some simulations, the fuel assemblies are modeled as solid blocks or porous media with effective properties, while others model the fuel rods explicitly.

To validate thermal models, researchers use experimental temperature measurements from DSCs to compare with CFD models. The only experiment with available data for both storage and vacuum drying conditions that is loaded with high burnup fuel is conducted for the TN-32B cask. The Electric Power Research Institute (EPRI), in a project called the High Burnup (HBU) Spent Fuel Data Project, has loaded a TN-32B cask with characterized SNF assemblies and subjected the cask to all the storage

operations, including vacuum drying (EPRI 2014). Researchers have been continuously monitoring the temperatures within seven selected fuel assemblies at nine elevations and 15 external cask locations after removal from the spent fuel pool. Steady-state data from a two-week “thermal soak” wherein the cask reached thermal equilibrium in a monitored decontamination pit is used for comparison with thermal models (Fort, Richmond, Cuta, et al. 2019; Akkurt and Csontos 2020; Higley, Hadj-Nacer, and Greiner 2021; Hall and Zigh 2019).

The TN-32 has a 2.5-m outer diameter and is designed to have a 4.78-millimeter gap between the basket structure that supports the SNF and the containment boundary. The thermal resistance across this narrow gas-filled gap is potentially large compared to that of metal package components, and rarefaction during vacuum drying significantly increases it compared to continuum storage conditions. The gap thermal resistance is proportional to its width, whose value is uncertain due to manufacturing tolerances, basket shifting, and thermal expansion. This uncertainty in gap width is the most significant source of input uncertainty, and has led to significant uncertainty in temperature predictions (Hall and Zigh 2019).

The overall objective of this work is to create accurate computational methods to predict cask temperatures under storage and vacuum drying conditions. To develop these methods, CFD models of the TN-32B SNF are created and simulated for comparison with the experimental data for both storage and vacuum drying conditions. This dissertation was divided into three main sections, each one is a stand-alone journal paper.

In the first paper, the effect of basket/rail gap width and its non-uniformity on  $T_{PC}$ , under both continuum storage and rarefied vacuum drying conditions was

investigated. Two-dimensional (2D) simulations of a TN-32 cross-section are conducted, because they can predict the effects of basket/rail gap variations and rarefaction but require fewer resources than three-dimensional simulations. To the extent possible, the conditions of recent TN-32 high burnup DSC measurements (Akkurt and Csontos 2020) are utilized to make the results relevant to future validation efforts.

In the second paper, three-dimensional (3D) homogenous fuel region models of the TN-32B are developed in which the fuel assemblies are modeled as porous media with effective properties. The storage conditions of the HBU project are applied for comparisons between experimentally measure temperatures in the fuel region and computationally predicted temperatures at the same locations. Uncertainty in the widths of nine gaps, including the basket/rail gap, are investigated using a global uncertainty quantification method. Latin Hypercube Sampling is used to choose the gap widths in 40 simulations to generate confidence intervals on temperature prediction and estimate temperature uncertainty attributable to each gap. In the third and final paper, a one-eighth 3D model of the TN-32B is constructed with a detailed representation of the fuel assemblies. The same computational mesh was used to generate a homogenous model, with the fuel regions represented as porous heat-generating blocks. An assembly-of-interest fuel region heat loading that allows for reasonable comparisons with experimental data is proposed and used in the simulations. Effective thermal and flow properties for homogenous model were derived from sub-models. The temperature and flow velocity predictions were compared on a point-to-point basis between the detailed and homogenous models throughout the fuel region. The temperatures at 63 locations

obtained from the detailed model are compared to data from the High Burnup Demonstration project.

## Chapter 2: Effect of basket/rail gap on temperature prediction in the TN-32 cask under storage and drying conditions

---

### ABSTRACT

This paper investigates the effect of the variation in the gap width between the basket and rails on predicted temperatures in the TN-32 dry storage cask. Two-dimensional (2D) cross-section models of the TN-32 containing thirty-two spent nuclear fuel assemblies generating 30.5 kW of thermal energy are constructed. Storage and vacuum drying pressures, a range of basket/rail gap widths, and shifting of the basket from the cask center, are considered. The simulations include surface-to-surface radiation and gas conduction (including rarefaction), but do not consider natural convection due to the 2D assumption. Results show that the peak cladding temperature,  $T_{PC}$ , increases as the gap width increases and as the pressure decreases to vacuum drying (rarefied) levels. As a result, analysis using the nominal unloaded design gap width may overpredict  $T_{PC}$  by up to 40°C under storage conditions and up to 75°C under vacuum drying conditions. The sensitivity of  $T_{PC}$  on pressure is found to decrease as the gap width decreases, and as the basket shifts from the cask center. This paper demonstrates that reducing the uncertainty in the basket/rail gap width by, for example, calculating predictable thermal expansion, and/or statistically quantifying unpredictable manufacturing tolerances and basket shifting, may significantly reduce the uncertainty of peak cladding temperature prediction.

**Key Words:** *SNF Cask, Heat Transfer, Basket/rail Gap, CFD, Storage Conditions, Vacuum Drying Conditions, Rarefaction.*

## **NOMENCLATURE**

$D$	Displacement distance [mm]
$k_B$	Boltzmann constant ( $1.38 \times 10^{-23}$ [J K <sup>-1</sup> ])
$Kn$	Knudsen number
$L_c$	Characteristic length [m]
$m$	Mass [kg]
$P$	Pressure [kPa]
$Pr$	Prandtl number
$R$	Thermal resistance [K m <sup>2</sup> W <sup>-1</sup> ]
$T$	Temperature [°C]
$W$	Gap width [mm]
$x$	$x$ -coordinate [m]

### ***Subscripts***

$0$	Reference
$avg$	Average
$CR$	Corner Rail
$env$	Environment
$in$	Inner surface
$out$	Outer surface
$PC$	Peak Cladding

*TJ* Temperature-Jump

***Greek***

Thermal Accommodation Coefficient

Specific heat ratio

*T* Temperature-jump coefficient

Thermal conductivity [ $\text{W m}^{-1} \text{K}^{-1}$ ]

Mean free path [m]

Dynamic viscosity [ $\text{kg m}^{-1} \text{s}^{-1}$ ]

***Abbreviations***

2D Two-dimensional

CFD Computational Fluid Dynamics

DSC Dry Storage Cask

PWR Pressurized Water Reactor

SNF Spent Nuclear Fuel

**1. Introduction**

Spent nuclear fuel (SNF) assemblies discharged from light water reactors consist of highly radioactive, heat-generating fuel pellets stacked inside square arrays of sealed zircaloy cladding tubes (Saling and Fentiman 2001). When SNF assemblies are first removed from a reactor, they are stored in water-filled pools while their heat generation rate and radioactivity decrease. After sufficient time, several SNF assemblies are moved to a dry storage cask (DSC) such as the TN-32 (Areva 2002), or other packaging. Most

DSCs consist of an inner basket with square-cross section openings for the SNF assemblies, and an outer structure (Areva 2002; McKinnon et al. 1989). The basket supports the fuel, provides a heat conduction path, and controls neutrons. The outer structure provides containment and shielding. Rails connected to the inner surface of the outer structure hold the basket in place. To facilitate assembly, many DSCs have a millimeter-scale gap between the basket and the rails. This is referred to as the basket/rail gap.

To load a DSC, it is lowered into the pool and the SNF is placed into the basket openings while it is underwater. The DSC is then covered, lifted out of the pool, and drained. Remaining moisture must be removed to reduce the risk of future corrosion and/or flammable gas formation (Miller et al. 2013; Large 1999). The most common method to remove moisture is vacuum drying. During this process over a 6 to 129 hour period, the package internal pressure is reduced in stages to as low as 0.067 kPa to promote water evaporation and vapor diffusion out of the system (Bracey and Smith 2012). A sealed package is considered dry when it can maintain a pressure of less than 0.4 kPa for 30 minutes (ASTM 2016). After drying, the package is filled with helium or another non-oxidizing gas to pressures between 100 and 800 kPa and sealed. It may then be stored on-site or transported to another location.

During all normal post-reactor operations, the peak cladding temperature,  $T_{PC}$ , and temperatures of specific package components must be maintained below specified limits (NRC 2003, 2010). For example, the limit for  $T_{PC}$  is dependent on specific conditions, but is nominally 400°C. SNF may experience its highest temperature while or

soon after being transferred to a dry package. This is because it is the first time it is not directly water-cooled, and its heat generation rate is still relatively high. Additionally, the low pressures employed during vacuum drying may cause the gas in the narrow package gaps to become rarefied (Bird 1983; Hadj-Nacer et al. 2017). This reduces conduction heat transfer at the gas-solid interfaces, which increases internal temperatures compared to non-rarefied (continuum) conditions.

Two- and three-dimensional computational fluid dynamics (CFD) simulations have been used to predict  $T_{PC}$  and other component temperatures and their uncertainties to assure they do not exceed required limits (Suffield et al. 2012; Areva 2002; Yoo et al. 2010; Lee et al. 2009; Brewster et al. 2012). Across gas-filled voids between solid surfaces, they model surface-to-surface radiation, conduction, and in some cases, natural convection heat transfer. In some simulations, the fuel assemblies are modeled as solid or porous blocks with effective properties (Kamichetty, Venigalla, and Greiner 2014; Hall, Zigh, and Solis), while geometrically accurate simulations model the fuel rods and surrounding gas explicitly (Manzo, Nacer, and Greiner 2015; Brewster et al. 2012; Yoo et al. 2010).

Most of the heat generated by the SNF is conducted across the gas within the basket/rail gap. Natural convection and radiation heat transfer across the gap are low compared to conduction due to the relatively cool surface temperatures and narrow gap width. Even though the gap width is small compared to the ~2.5-m DSC outer diameter, the gas thermal conductivity is small compared to the metal DSC components. As a result, the conduction thermal resistance across the gap can strongly affect  $T_{PC}$  (Higley,

Hadj-Nacer, and Greiner 2019a, b). Since gap thermal resistance is proportional to its width, uncertainty in the width can lead to significant uncertainty in  $T_{PC}$ .

Manufacturers may specify a nominal designed gap width, which may correspond to when the DSC is unloaded or “cold.” However, during operation, the gap width may be reduced or become non-uniform due to predictable thermal expansion as well as unpredictable manufacturing tolerances or basket shifting. When the operating gap width is unknown, analysts may employ the nominal manufactured gap width to conservatively overpredict package temperatures. However, this may lead to loading DSCs with lower heat-generating fuel, or fuel that has spent more time in the spent fuel pool, than would be required for safety.

During vacuum drying, the package void spaces are filled with a mixture of helium and water vapor. As the pressure is reduced, the gas density decreases, and natural convection is effectively eliminated. To predict temperatures during that process, some analysts assume the voids are filled with pure water vapor (Fort, Richmond, Jensen, et al. 2019) or air (Areva 2002). Conduction is modeled across the gas, but surface-to-surface radiation heat transfer may (Fort, Richmond, Jensen, et al. 2019) or may not be included (Areva 2002). These methods may conservatively predict higher temperatures than exist during drying, because the thermal conductivities of water vapor and air are lower than the helium-water vapor mixture that likely fills the cask during vacuum drying. Also, neglecting radiation heat transfer (which is a significant heat transfer mechanism within the fuel region of the cask) may lead to over-conservatism in

temperature prediction. However, those studies do not include gas rarefaction, which is active during drying, and may significantly decrease conduction heat transfer.

The current authors used Direct Simulation Monte Carlo methods to numerically verify (Hadj-Nacer et al. 2017), and then experimentally validated (Maharjan, Hadj-Nacer, and Greiner 2020a) an existing kinetic-theory-based method (Lin and Willis 1972) to predict reduced gas conduction in the slip-flow rarefied gas regime. They implemented the validated model into geometrically accurate two-dimensional simulations of a TN-24 DSC (McKinnon et al. 1989), assuming its basket/rail gap was filled with dry helium and had the nominal manufactured width. The researchers found that rarefaction during vacuum drying has the potential to markedly increase that gap thermal resistance and  $T_{PC}$  (Hadj-Nacer et al. 2016).

Bench scale and mockup fuel assembly data are available to quantitatively validate CFD thermal models used to calculate heat transfer effects within DSCs (Hadj-Nacer et al. 2017; Maharjan, Hadj-Nacer, and Greiner 2020b; Durbin and Lindgren 2017). However, temperature measurements within loaded DSCs are limited (Unterzuber et al. 1982), especially for high burnup fuel.

In 2017, thirty-two well-characterized high-burnup SNF assemblies, with an initial total thermal generating of  $Q = 30.464$  kW, were loaded into a TN-32 DSC (EPRI 2014). The DSC was instrumented with thermocouples to measure fuel region and exterior surface temperatures during both vacuum drying and storage operations. The measurements showed that the fuel region temperature increased rapidly when the DSC water was drained and vacuum dried. The temperatures then decreased and reached a

quasi-steady state after the package was filled with helium to a pressure of 223 kPa. Initial storage simulations predicted fuel region temperatures that were consistently hotter than the measured values, believed to be due to the assumed basket/rail gap being larger than its experimental width. Those authors postulated that the effective basket/rail gap width may have been smaller than originally assumed (Fort, Richmond, Cuta, et al. 2019). This data showed that relatively small geometrical variation in the basket/rail gap, may considerably affect the temperatures within the DSC. However, due to geometric uncertainties and other factors, the TN-32 high burnup DSC data is not considered suitable for statistically based model validation (Hall and Zigh 2019).

The current work is unique from previous work in its explicit treatment of the basket/rail gap and its uncertainty in addition to consideration of rarefaction effects within the basket/rail gap for vacuum drying pressures. The goal of this paper is to quantify the effects of basket/rail gap width and non-uniformity on  $T_{PC}$ , under both continuum storage and rarefied vacuum drying conditions. In this paper, two-dimensional (2D) simulations of a TN-32 cross-section are conducted, because they can predict the effects of basket/rail gap variations and rarefaction but require fewer resources than three-dimensional simulations. To the extent possible, the conditions of recent TN-32 high burnup DSC measurements (Akkurt and Csontos 2020) are utilized to make the results relevant to future validation efforts.

## **2. Two-dimensional computational model**

Figure 2.1 shows a 2D cross-section model of a loaded TN-32 (Areva 2002) generated using the ANSYS package (ANSYSInc. 2009). All 32 PWR assemblies consist

of 17x17 array of fuel rods and 25 hollow instrument/guide tubes, all with a center-to-center pitch of 12.6 mm. The fuel rods are 8.36-mm-diameter uranium dioxide pellets surrounded by 0.572-mm-thick zircaloy cladding. The zircaloy instrument/guide tubes are hollow and have a 12.24-mm outer diameter and the same wall thickness as the cladding. Each fuel assembly is centered within a square basket tube, whose interior sides are 22.1-cm  $\times$  22.1-cm. The basket is formed from 2.667 mm thick stainless steel plates that encapsulate aluminum and BORAL® neutron poison plates, 12.7 and 1.016 mm in thickness, respectively, which are sandwiched together to form the square grid structure.

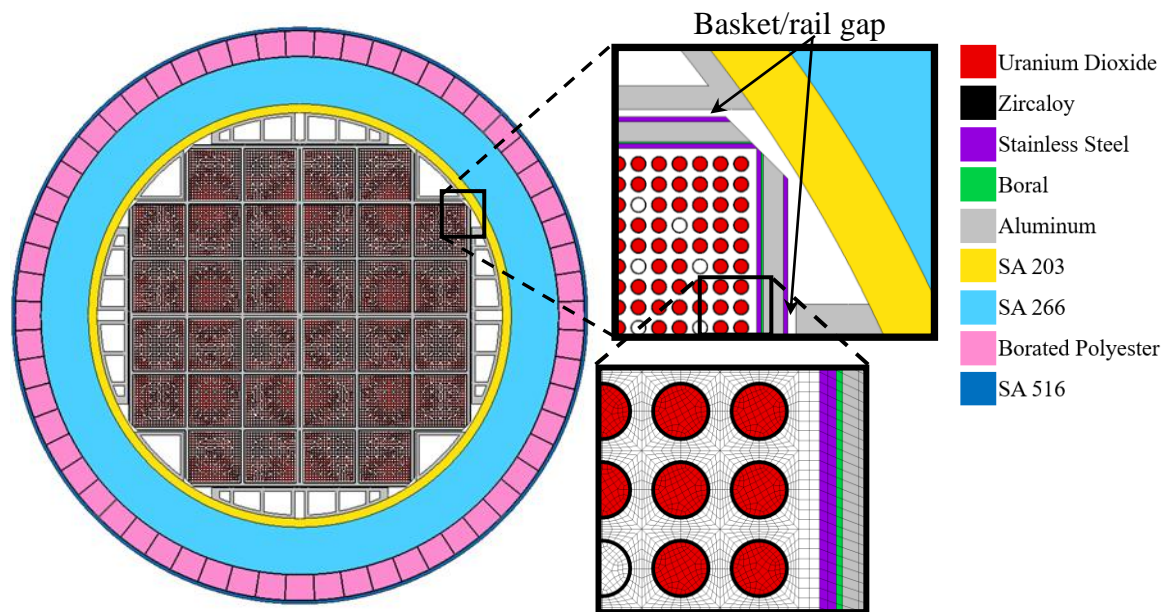


Figure 2.1. TN-32 DSC cross-section model color coded by material. Detailed views showing basket/rail gaps and mesh are included.

Eight aluminum rails are located on the four sides and four corners of the basket to provide structural support to the basket and a conduction heat path. The thickness of its plates varies from 14.29 to 15.9 mm. The current work uses approximations of their

shape due to the lack of accurate dimensions and to facilitate meshing. The rails are fastened to the SA-203 carbon steel inner shell. That shell is 38.1-mm-thick, has an inner diameter of 174.6 cm, and serves as the primary confinement barrier. The gamma shield, made of 203.2-mm-thick carbon steel (SA-266), surrounds the inner shell. Thin (6.35 mm) aluminum walled boxes filled with 101.6 mm of borated polyester resin are attached to the outer surface of the gamma shield and form a neutron shield. The final layer is the 12.7 mm SA 516 carbon steel outer shell that is coated with a high emissivity paint to help dissipate heat to the environment. The outer diameter of the cask is 2.483 m. The basket and assemblies within it are referred to as the *basket structure*. The aluminum rails, inner shell, gamma shield, and neutron shield together are referred to as the *outer structure*.

The expanded view in Fig. 2.1 shows two gaps, between the basket and a corner-rail (horizontal gap), and between the basket and a side-rail (vertical gap). This paper considers a range of uniform and non-uniform basket/rail gap widths. In addition to these gaps, there are void spaces within the instrument/guide tubes, between the rods and fuel basket, and within the rail structures. In this work, all void spaces are filled with dry helium. However, during actual drying operations, the gas may contain some moisture.

#### **a. Geometric Variations**

Before the TN-32 is loaded with heat generating spent fuel, the basket rail gap thickness,  $W$ , may be uniform on all sides of the basket. The nominal design gap width is  $W = 4.78$  mm, but no uncertainty in this value is reported (Areva 2002). Due to differential thermal expansion, the basket/rail gap width may be substantially reduced

during drying and storage. Moreover, due to manufacturing tolerances, shifting of the basket structure, and other uncontrolled factors, the gap width may be neither uniform nor predictable. This section describes six geometric variations to the TN-32 model with different basket/rail gap configurations. These variations are used to evaluate the effect of basket/rail gap on  $T_{PC}$ .

### **i. Centered Basket Configurations**

If the basket remains centered within the outer structure, the basket/rail gap width  $W$  will be uniform on all sides. In addition to the design gap width,  $W = 4.78$  mm, three configurations with smaller uniform gap widths of  $W = 2.54$ ,  $1.27$ , and  $0$  mm are considered. The gapless model ( $W = 0$ ) is a bounding case where the basket-rail gap is entirely closed. However, further research must be conducted to determine if thermal expansion or other factors could cause the gap to completely close.

For all centered basket configurations, the domain in Fig. 2.1 is symmetric about vertical, horizontal, and diagonal lines that pass through the package basket center. To reduce computational resources, pie-shaped domains are created that represent one-eighth of the full domain (see Fig. 2.2a) and symmetry boundary conditions are applied along the radial edges. The basket/rail gaps are reduced by uniformly increasing the thickness of the stainless-steel tube surrounding the outermost basket structure surface.

### **ii. Shifted Basket Configurations**

Even if the basket dimensions do not expand, the gap width distribution around the basket may be affected if the basket structure shifts (translates) relative to the outer structure. To bound this, two models are generated. The side-shifted model assumes that

the basket in Fig. 2.1 translates 4.78 mm to the left, closing the basket-rail gaps on the left side and doubling them on the right side. In this model, the top and bottom gaps remain at the nominal value of 4.78 mm. Based on symmetry, this condition is modeled using a semi-circular mesh that includes the top half of Fig. 2.1 and employs symmetry along the horizontal line that passes through the basket center (see Fig. 2.2b). The diagonal-shift model translates the basket in Fig. 2.1 by 4.78 mm to the left and 4.78 mm down. This closes the left and bottom gaps and doubles the gaps on the opposite sides. The diagonal-shifted model is symmetric along the diagonal line that passes through the basket center in Fig. 2.1 from the lower left to the upper right (see Fig. 2.2c).

To model both these shifted configurations, the entire basket structure is moved relative to the outer structure. While shifting the basket increases the gap width on some sides and decreases it on others, the *average* basket/rail gap remains at the nominal value  $W = 4.78$  mm. The basket displacement,  $D$ , is defined as the distance between the centers of the outer and basket structures. For the centered, side-shifted, and diagonal-shifted models, the displacements are, respectively,  $D = 0$ , 4.78, and 6.76 mm.

### 3. Computational methods

Steady-state simulations of the six model domains (four centered and two shifted basket configurations) described in the last section were conducted using ANSYS/Fluent (ANSYSInc. 2009). The number of elements in the models is 0.3 million for the centered basket configurations and 1.5 million for the shifted configurations. An expanded view of the mesh is shown in Fig. 2.1. The mesh comprised almost entirely of highly structured, hexahedra elements with an average element quality of 0.7. Earlier work (Higley 2019)

using the Grid Convergence Index (Roache 2009) estimated spatial discretization error to be approximately 1% for these meshes.

The length of the heat generating region of the fuel rods in the direction normal to Fig. 2.1 is 3.66 m, but the TN-32 is 4.67 m long in that direction. Most of the heat generated by the SNF transfers radially to the round outer surface of the DSC. However, a fraction also transfers out through its two ends and the side surfaces near the ends. As a result, temperatures predicted from the current two-dimensional model are likely warmer than values that would be predicted from three-dimensional models.

Consistent with the TN-32 DSC high-burnup experiment conditions (Akkurt and Csontos 2020), the air environment is modeled at 24°C. At steady-state, all generated heat transfers from the TN-32's curved outer surface to the surroundings by natural convection (calculated based on a vertical flat plate correlation (Holman 1997)) and radiation heat transfer, using an exterior surface emissivity of 0.9. The heat generation rate of all fuel rods is assumed to be identical. However, it varies in the direction normal to the plane of Fig. 2.1 and peaks near the axial center of the assemblies, with a peaking factor at  $PF = 1.1$  times the average rate. Based on these assumptions, for all simulations in this work, the pellet volumetric heat generation rate is calculated as

\_\_\_\_\_ .....

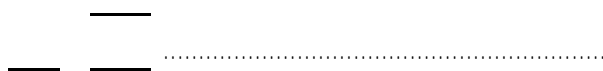
Based on the number, length and diameter of the fuel pellets stated earlier, in each of the 32 assembly, total fuel pellet volume is  $V = 1.684 \text{ m}^3$  and the pellet volumetric heat generation rate is  $\dot{q} = 19,895 \text{ W/m}^3$  (Areva 2002; Akkurt and Csontos 2020).

In all simulations, conduction heat transfer is modeled across all solid components using temperature-dependent thermal conductivities (Akkurt and Csontos 2020). Across the gas-filled regions surface-to-surface radiation is modeled using the Discrete Ordinates Radiation model (ANSYSInc. 2009). The surface emissivity of zircaloy, stainless steel, aluminum, and carbon steel are respectively, 0.8, 0.3, 0.2, and 0.45 (Akkurt and Csontos 2020). Gas conduction (and effect of rarefaction) are modeled using an explicit representation of gas regions with an applied temperature-dependent thermal conductivity described in the next section. All solid components that touch (including the basket and rails for the  $W = 0$  simulations, and the shifted models) are assumed to be in intimate contact, with no thermal resistance between them.

During drying and storage operations, the plane of Fig. 2.1 is horizontal (perpendicular to gravity). As a result, the effect of internal natural convection is not admissible in this 2D model. However, some other works (Fort, Richmond, Cuta, et al. 2019; Hall and Zigh 2019) that simulated the TN-32 using 3D models indicate that natural convection does not significantly affect the temperatures. Also, during vacuum drying, buoyancy-induced gas motion is effectively eliminated due to the low gas pressure and density.

#### **a. Vacuum Drying Modeling**

Kinetic theory shows that the mean free path between ideal gas molecule collisions increases as the gas pressure,  $P$ , decreases and temperature,  $T$ , increases, according to (Bird 1983)



In this expression,  $\mu_0$  is the gas dynamic viscosity at a reference temperature,  $m$  is the mass of the gas molecule, and  $k_B$  is Boltzmann's constant. For a gas constrained in a volume with characteristic wall-to-wall dimension,  $L_c$ , the Knudsen number is the dimensionless ratio of the mean free path to the containment volume characteristic length,  $Kn = \lambda / L_c$  (Schnaaf and Chambré 1961).

In typical (continuum) engineering applications,  $Kn < 0.001$ , and molecules at most all locations within an enclosed domain are bombarded by other molecules nearly uniformly from all directions. Molecules within a thin Knudsen Layer near the wall, whose thickness is of the order of  $\lambda$ , are struck by other molecules traveling toward the wall more frequently than they are by molecules traveling away from the wall. However, for  $Kn < 0.001$ , this layer is very small compared to the enclosure. Under these conditions, the gas acts as a continuum. As a result, conduction and momentum transport are accurately characterized using local thermal conductivity and viscosity, and the gas temperature and velocity at the interface with a solid wall are essentially equal to those of the wall (no-slip conditions).

For the DSC configurations considered in this work, the smallest finite wall-to-wall spacings are either between the basket and rails ( $L_c = W = 4.78, 2.54, \text{ or } 1.27 \text{ mm}$ ) or when  $W = 0$ , between fuel rods,  $L_c = 8.32 \text{ mm}$ . Under *storage conditions*, the dry helium within all TN-32 gaps is at an internal pressure of  $P = 223 \text{ kPa}$ , and the gas temperatures are presented later in this work (see Figs. 2.3 and 2.5). Based on the dimensions,

pressure, and temperatures during DSC storage,  $Kn < 0.001$  and “normal” continuum conditions apply.

For vacuum drying, we consider pressures of  $P = 0.4$  and  $0.1$  kPa. The first is chosen because sealed packages must remain below that pressure for 30 minutes before they can be considered dry[5](“ASTM C1553-16, Standard Guide for Drying Behavior of Spent Nuclear Fuel, ASTM International, West Conshohocken, PA, 2016, www.astm.org”)[5][5]. The second pressure is near the lowest pressure used during vacuum drying (Large 1999). For the relevant DSC vacuum drying conditions, the Knudsen number for the DSC package is within  $Kn = 0.01 - 0.27$ , so that the Knudsen layer thickness is not insignificant compared to the enclosed space. In this range, slip-flow rarefied gas regime methods may be used (Maharjan et al. 2015). In that model, gas outside the Knudsen layer continues to act as a continuum. However, the gas temperature near heated walls is not the same as that of the wall, and the wall/gas temperature difference (jump) increases with increasing heat flux at the wall.

To model the effect of temperature-jump rarefaction during vacuum drying, a heat flux thermal resistance at all solid/gas interfaces is implemented(Hadj-Nacer et al. 2016)

$$\text{---} \quad (2.3)$$

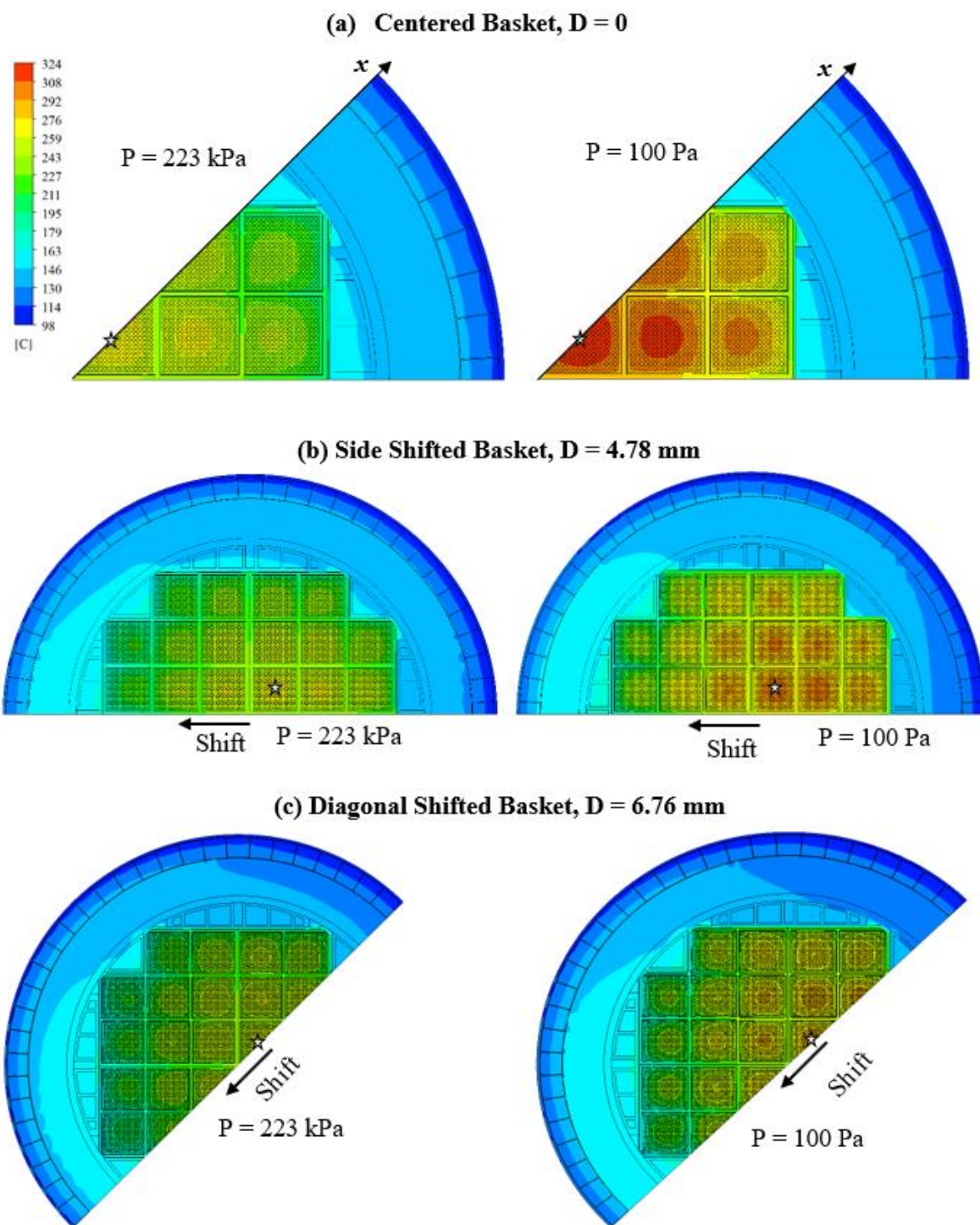
In this expression,  $\kappa_g$  is the gas thermal conductivity near the surface. The temperature jump coefficient for monoatomic and polyatomic gases may be found as (Lin and Willis 1972; Bird 1994)

$$\text{---} \quad \text{---} \quad (2.4)$$

In this expression, the gas/surface thermal accommodation coefficient is  $\alpha$ , the gas Prandtl number is  $Pr$ , and the gas specific heat ratio is  $\gamma$ . Equations 2-4 show that both the mean free path and the temperature jump-thermal resistances increase as the pressure decreases. The literature shows that  $\alpha$  for helium on stainless steel decreases from 0.4 to 0.2 as the temperature increases from 10°C to 495°C (Song and Yovanovich 1987). For helium on a zircaloy surface,  $\alpha = 0.34$  was reported at a temperature of 25°C (Thomas and Loyalka 1982). In this work, a constant value of  $\alpha = 0.3$  is used for all vacuum drying simulations. As described earlier, this simulation method was verified and quantitatively validated in bench-scale vacuum experiments (Maharjan, Hadj-Nacer, and Greiner 2020b, a).

#### 4. Simulation Results

Figure 2.2 shows six TN-32 temperature contours for centered ( $D = 0$ , Fig. 2.2a), side-shifted ( $D = 4.78$  mm, Fig. 2.2b), and diagonal-shifted ( $D = 6.76$  mm, Fig. 2.2c) baskets. All these contours have the same average gap spacing of  $W = 4.78$  mm. The left- and right-hand contours show results for  $P = 223$  kPa (continuum regime) and 0.1 kPa (rarefied regime), respectively. Arrows in Figs. 2.2b and 2.2c show the direction the basket is shifted relative to the outer structure. As described earlier, symmetry conditions are imposed along the radial boundaries. To recreate the temperature distribution within the full round cross-section, the reader may imagine reflecting the contours in Fig. 2.2 about those boundaries.



All six contours use the same temperature scale, and the five-pointed stars show the hottest locations in each. For all six, each fuel assembly exhibits a local temperature maximum, and the basket walls surrounding each assembly are cooler. The temperature varies strongly in all directions within the basket structure, but weakly in the circumferential direction in outer structure. For each configuration, the continuum and rarefied contours exhibit nearly identical temperature contours in the outer structure. However, the basket structure is significantly hotter under rarefied conditions ( $P = 0.1$  kPa) than for  $P = 223$  kPa.

For the centered basket configuration in Fig. 2.2a, due to symmetry, the four centermost assemblies have the same temperatures, and each contains a rod that has the peak cladding temperature,  $T_{cl}$ . The peak cladding temperatures at  $P = 223$  kPa and 0.1 kPa are, respectively,  $272^{\circ}\text{C}$  and  $324^{\circ}\text{C}$ . For both pressures, the TN-32 outer surface is nearly isothermal due to the uniformity of the outer structure and its boundary condition. Temperature contours for centered basket configurations with smaller gap widths of 2.54, 1.27, and 0 mm are qualitatively like the ones in Fig. 2.2a, and so are not included.

Figure 2.2b shows that when the basket is shifted to the left side, the two assemblies just to the right of the package center become the hottest within the DSC. However, the left side of the outer surface becomes hotter than the right side. Similarly, Fig. 2.2c shows that when the assembly is shifted diagonally to the lower left, the assembly to the upper right of the center is the hottest, and the hottest outer surface temperature is on the bottom left.

Overall, Fig. 2.2 shows that shifting the basket by small amounts ( $D = 4.78$  or  $6.76$  mm) decreases the peak cladding temperature even though the average basket/rail gap width remains unchanged. The average outer surface temperature for all configurations in this work is  $109^{\circ}\text{C}$ , which is  $85^{\circ}\text{C}$  warmer than the environment. This is because all simulations consider the same fuel heat generation rate and employ the same environment temperature and heat transfer modes. However, the outer surface becomes less isothermal as the shifting amount,  $D$ , increases.

### a. Centered Basket Configurations

For centered-basket simulations ( $D = 0$ ), Fig. 2.3 presents the interior temperature,  $T$ , along the  $x$ -axis, whose location is shown in Fig. 2.2a. Figure 2.3a shows results for  $W = 4.78$  mm and three pressures ( $P = 223, 0.4,$  and  $0.1$  kPa). Figure 2.3b exhibits results for,  $P = 223$  kPa and three basket/rail gap widths ( $W = 0, 2.54,$  and  $4.78$  mm). The  $x$ -axis lies on a diagonal symmetry line of the TN-32, and its origin is at the basket center. Based on symmetry, the location of the peak cladding temperature  $T_{PC}$  is along the  $x$ -axis. For reference, the inner surface of the corner rail, which is on the outer surface of the basket/rail gap, is at  $x = 70.8$  cm. The location of the thin basket/rail gap is identified in Fig. 2.3.

All profiles in Fig. 2.3 exhibit undulations within the basket as the  $x$ -axis passes through the warm rods and gas of two fuel assemblies and three cooler basket walls. Within each assembly, the rods are relatively isothermal. However, temperature gradients within the gas are visible. For all centered-basket simulations in this work, the peak cladding temperature is located near  $x = 16.9$  cm. Most of the profiles exhibit abrupt

temperature differences across the basket/rail gap. Finally, within the outer structure, the profile exhibits mild gradients as it passes through the corner rail, inner shell, gamma shield, and neutron shield. All profiles are nearly identical in the outer structure. This is because the conduction heat transfer in the outer structure, and transport mechanisms between the DSC outer surface and environment are unaffected by the  $P$  and  $W$ . Within the basket, the profile shape and the difference between the peak cladding temperature and the minimum basket temperature are similar for all the simulations. However, Fig. 2.3a shows that the temperature difference across the basket/rail gap increases significantly as the pressure decreases into the rarefied regime. Figure 2.3b shows that this difference also increases as the gap width increases.

The difference between the peak cladding and environment temperatures can be broken into the sum of three parts:

.....

In this expression, the environment/outer structure temperature difference is defined as  $T_{env} - T_{DSC}$ , where  $T_{DSC}$  is the corner rail inner surface temperature on the  $x$ -axis. The gap temperature difference is  $T_{gap} - T_{DSC}$ , where  $T_{gap}$  is the basket outer surface temperature on the  $x$ -axis. The basket temperature difference is  $T_{DSC} - T_{min}$ . For all centered basket simulations in this work,  $T_{DSC}$  is  $223 \text{ kPa}$ ,  $0.4 \text{ kPa}$ , and  $0.1 \text{ kPa}$ , and  $T_{min}$  is  $223 \text{ kPa}$ ,  $0.4 \text{ kPa}$ , and  $0.1 \text{ kPa}$ . Figure 2.4a and 2.4b show, respectively,  $T_{gap} - T_{DSC}$  and  $T_{DSC} - T_{min}$  versus gap width,  $W$ , for  $P = 223 \text{ kPa}$ ,  $0.4 \text{ kPa}$ , and  $0.1 \text{ kPa}$ . The results are connected by straight lines for ease of visualization, but no results are obtained between the symbols.

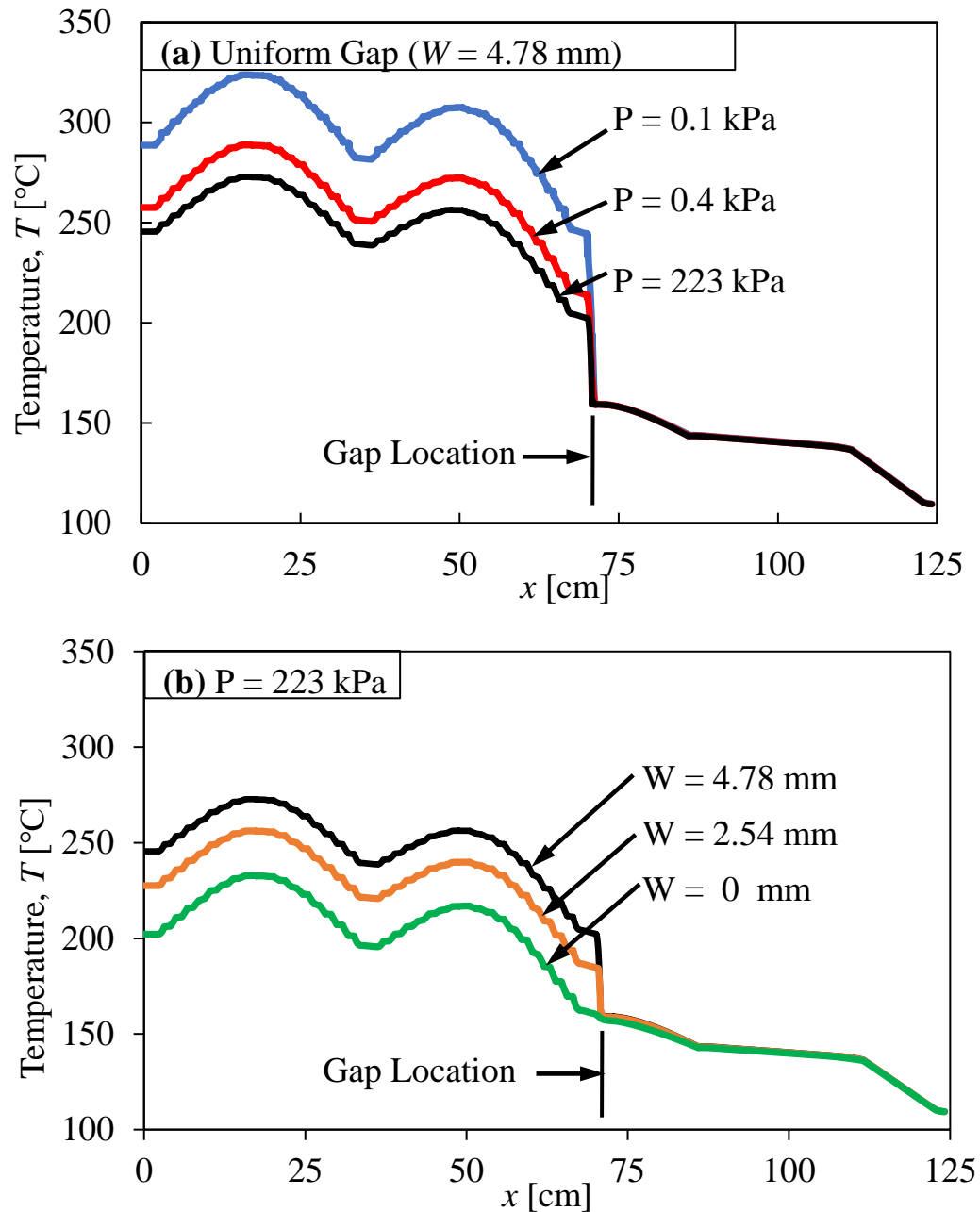


Figure 2.3. Centered-basket internal temperature profiles along the  $x$ -axis. (a) Nominal gap width ( $W = 4.78$  mm) for  $P = 0.1, 0.4$  and  $223$  kPa. (b) Continuum conditions ( $P = 223$  kPa) with  $W = 0, 2.54$  and  $4.78$  mm and representation of Eq. 4.

For the continuum condition ( $P = 223$  kPa), Fig. 2.4a shows that  $T$  increases nearly linearly with  $W$ . This is because conduction thermal resistance across the gas-filled

gap increases linearly with gap width. Conduction transports much more heat across the gap than surface-to-surface radiation due to its low surface emissivity and temperatures. For  $W > 0$ ,  $\dot{Q}$  increases significantly as the pressure decreases to 0.4 and 0.1 kPa. This is because, at these pressures, the temperature-jump thermal resistance at the gap surfaces significantly increases. Overall, Fig. 2.4a shows that, depending on the gap width and internal pressure,  $\dot{Q}$  can vary between 0 and 85 W.

Figure 2.4b shows that, for the continuum condition ( $P = 223$  kPa),  $\dot{Q}$  decreases mildly as  $W$  increases. This is because increasing  $W$  increases the fuel rod and basket surface temperatures, and this increases the surface-to-surface radiation heat transfer. Figure 2.4b also shows that, for a given gap width  $W$ ,  $\dot{Q}$  increases due to rarefaction as the pressure decreases to  $P = 0.4$  and 0.1 kPa. However, the increase is much smaller than the increase caused by rarefaction in the basket/rail gap (Fig. 2.4a). This is because the fuel rod and basket surface temperatures are hot enough so that radiation transports a large fraction of the heat between those surfaces. As a result, the basket temperature difference is not strongly affected by rarefaction (which only affects gas conduction). Overall, Fig. 2.4b shows that, depending on the gap width and internal pressure,  $\dot{Q}$  can vary between 71 and 91 W.

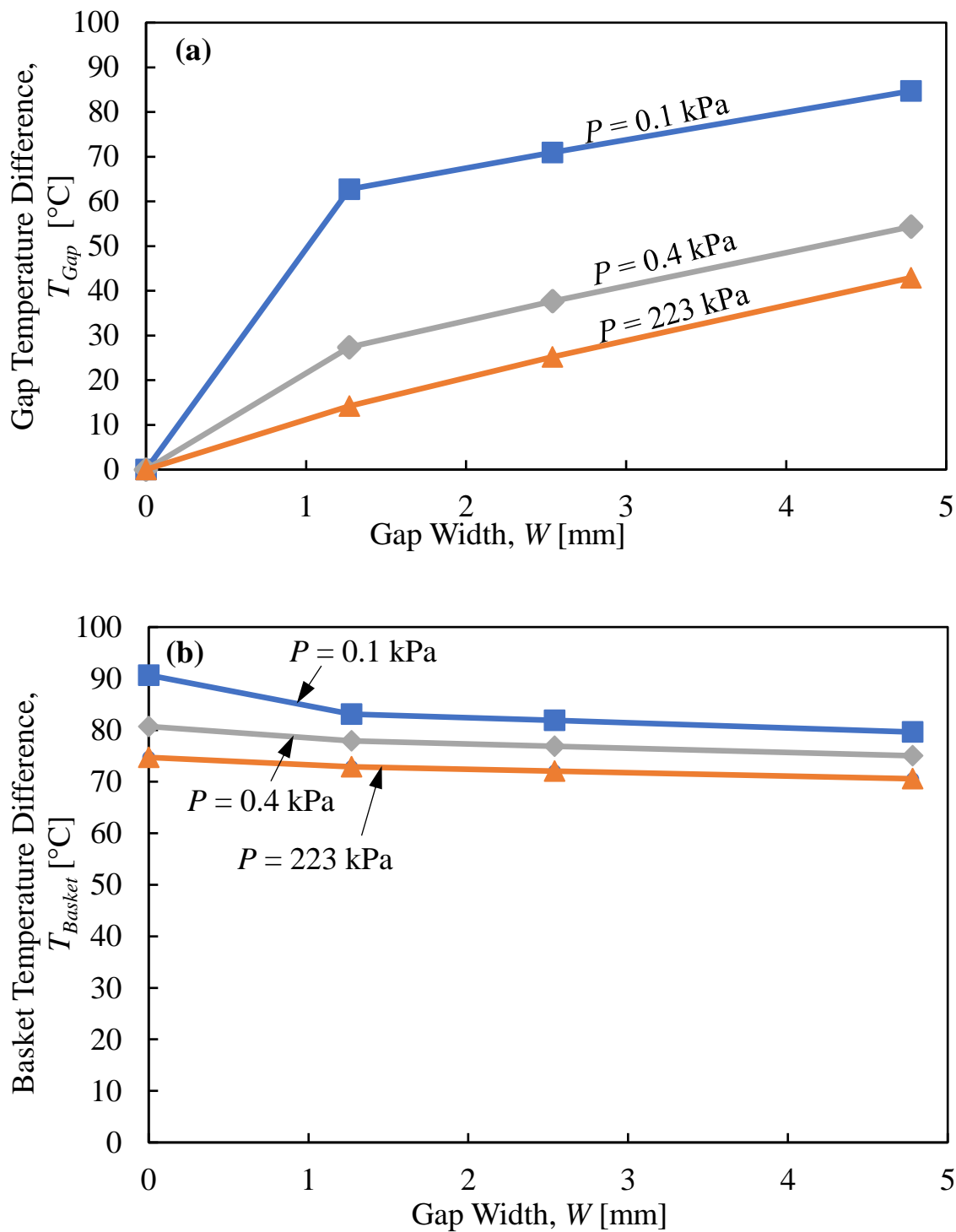


Figure 2.4. Centered-basket component temperature difference versus gap width for different pressures (a) Gap temperature difference. (b) Basket temperature difference.

### b. Peak Cladding and Surface Temperatures

Figure 2.5 shows the peak cladding temperature versus the average gap width,  $W$ , for  $P = 223, 0.4, \text{ and } 0.1$  kPa. Centered basket results are shown with solid symbols connected by solid lines. For the centered-basket configuration, the dependence of the peak cladding temperature on basket/rail gap width and internal pressure is like that of in Fig. 2.4a. This is because the variation of on  $W$  and  $P$  (Fig. 2.4a) is much stronger than that of either (which is constant) and (Fig. 2.4b). This demonstrates the importance of accurately modeling the effects of gap width and rarefaction within the basket/rail gap when determining the peak cladding temperature.

The open symbols connected by dotted lines in Fig. 2.5 show peak cladding temperatures for the shifted basket configurations. The side-shifted basket results have an “X” within the symbols, while the diagonal shifted results are fully open. The *average* gap width for the shifted configurations is  $W = 4.78$  mm. Even though the average basket/rail gap width is the same,  $T_{PC}$  for the diagonal-shifted configuration is less than that for the side-shifted configuration, which is less than that for the centered basket configuration.

For  $W = 4.78$  mm, the centered-basket peak cladding temperature at  $P = 0.1$  kPa is 51 hotter than it is at  $P = 223$  kPa. However, this difference is only 34 and 23 for the side-shifted and diagonal-shifted configurations. This shows that shifting the basket decreases the effect of rarefaction on the peak cladding temperature.

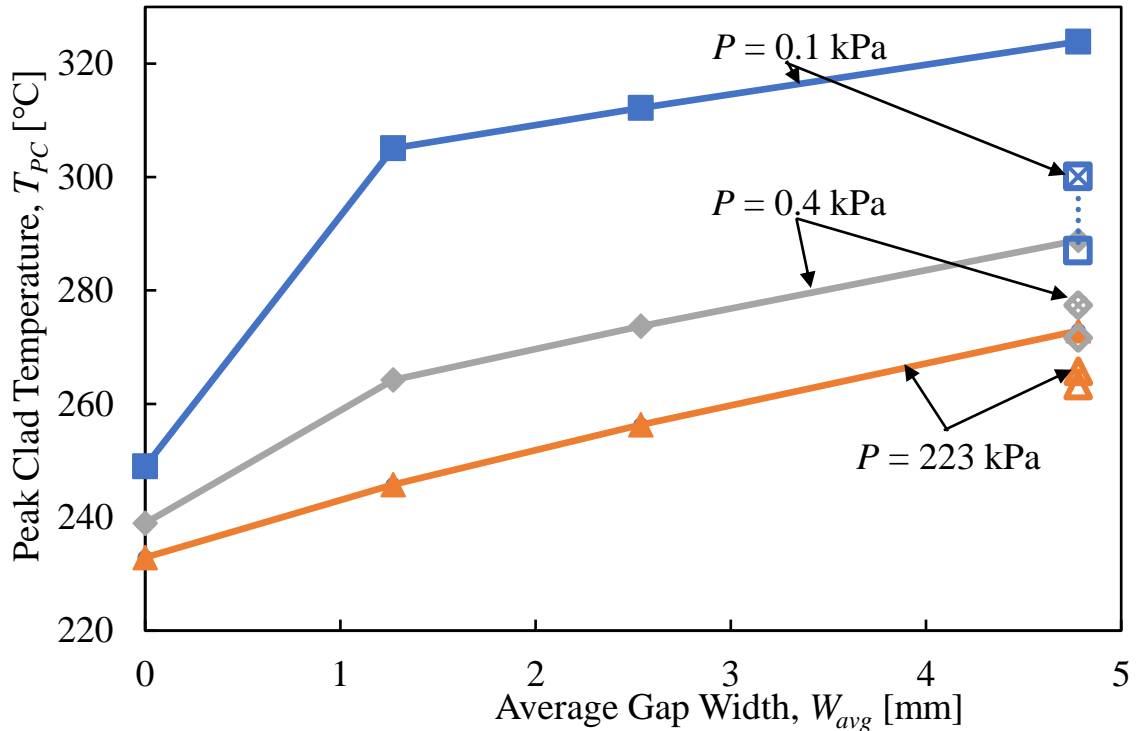


Figure 2.5. Peak cladding temperature versus average gap width for three internal pressures. The solid and open symbols show centered-basket and shifted-basket results, respectively. The open symbols with an “X” in the center are for the side-shifted configuration, while the completely open symbols are for the diagonal-shifted configuration.

Depending on the gap configuration and internal pressure,  $T_{PC}$  is predicted to be between 232°C and 324°C. This range is below the nominal limit of 400°C (NRC 2003). However, the 92°C-difference demonstrates the potential importance of the basket/rail gap (which may be affected by both unpredictable and predictable factors) and the internal pressure, on the peak cladding temperature. Additional research must be conducted to determine the best estimate and uncertainty of the gap width during storage and drying. However, Fig. 2. 5 shows that if the small gap is actually completely closed,

using the nominal gap width could overpredict  $T_{PC}$  by as much as 40 at  $P = 225$  kPa, and 75 at  $P = 0.1$  kPa.

As mentioned earlier, for all simulations performed in this work, the average surface temperature is 109°C. However, the temperature contours in Fig. 2.2 show that surface temperature is not as uniform for the shifted basket configurations as it is when the basket is centered. Figure 2.6 is a plot of the outer surface temperature variation, defined as the maximum minus the minimum surface temperature, versus the basket displacement  $D$ . Results are presented for  $P = 223, 0.4,$  and  $0.1$  kPa.

For the centered basket simulations,  $D = 0$ , for all gap widths and all pressures, . This relatively small variation is due to the uniform heat generation of the rods within the basket, the uniform gap width, the thick and relatively uniform geometry of the outer structure, and the uniform thermal environment in which the DSC is modeled to reside. Figure 2.6 shows that for all three pressures, increases with basket displacement. This is because basket shifting eliminates the conduction resistance at the basket/rail interfaces where the gap is closed, and it increases that resistance on the side where the gap is doubled. For  $D > 0$ , for a given displacement, the temperature variation increases as the pressure decreases into the rarefied regime. This is because rarefaction increases the conduction resistance across regions of the gap with finite widths, making the package surfaces near those regions cooler. However, rarefaction does not affect regions where the gap is completely closed.

Figure 2.6 shows that, compared to a centered basket, a diagonal shifted basket configuration may cause the DSC surface temperature variation to increase as much as

17°C or 21°C, at pressures of, respectively,  $P = 223$  kPa or 0.1 kPa. During actual DSCs storage or drying operations, this suggests that it may be possible to experimentally determine if the basket has shifted by measuring the non-uniformity of the surface temperature. However, to determine if that method is reliable, it would be necessary to determine if possible non-uniformity of the DSC environment and/or other uncontrolled factors could cause similar variations.

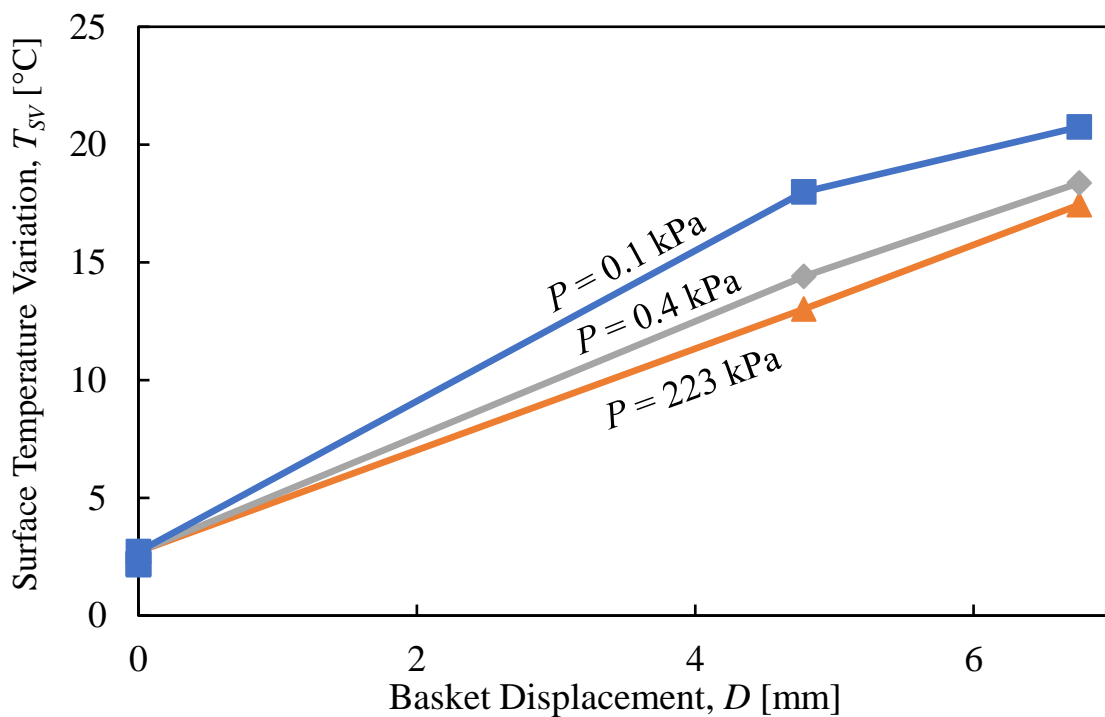


Figure 2.6. Surface temperature variation versus basket displacement for three internal pressures for all average wall spacings considered in this work.

## 5. Summary and Conclusions

Even though the basket/rail gap width is small compared to the TN-32 diameter, its high conduction resistance strongly affects the peak cladding temperature. During storage conditions when the package is filled with helium, uncertainty in its width, caused by both predictable thermal expansion, unpredictable manufacturing tolerances, or

by uncontrolled shifting of the basket relative to the outer structure, may cause the peak cladding temperature to be between 232 and 272 . During vacuum drying,  $T_{PC}$  may be between 248 and 324 . If the basket shifts relative to the outer structure, the potential variation is less. The peak cladding temperatures predicted by these two-dimensional simulations without natural convection are likely hotter than they would be in an actual TN-32, but they are all below the nominal 400 limit.

Typical SNF thermal analysis conservatively employs the nominal design gap size. The current work shows this may systemically overestimate cladding temperatures by significant amounts, which can lead to storing SNF underwater for longer periods than needed. This work shows that better estimates of the actual or probable basket/wall gap width, and its non-uniformity, would lead to significantly better prediction of the peak cladding and basket temperatures. Better estimates can be obtained by (a) performing coupled heat transfer/thermal deformation simulations, (b) statistically quantifying dimensional variation of manufactured components, and (c) determining how much the basket may shift relative to outer structure during transfer and storage processes. Additional research is also needed to predict heat transfer through rarefied moist helium. This will reduce the level of conservatism that is normally employed when packages are designed and licensed. The two-dimensional simulations presented in this paper may help guide future more complete three-dimensional calculations.

## **FUNDING**

This research is being performed using funding received from the US Nuclear Regulatory Commission (NRC) under contract 31310018M0032 and by the U.S. Department of

Energy (DOE) Office of Nuclear Energy University Program under award number DE-NE0008713.

## REFERENCES

- Akkurt, H., and A. Csontos. 2020. International Thermal Modeling Benchmark Description for a High-Burnup Used Fuel Dry Storage System: An Extended Storage Collaboration Program Activity. Palo Alto, CA: EPRI.
- ANSYS Inc. 2009. 12.0 Theory Guide. *ANSYS Inc.* 5 (5): 15.
- Areva. 2002. TN-32 Final Safety Analysis Report (FSAR), Revision 2. Virginia Electric and Power Company.
- ASTM. 2016. ASTM C1553-16, Standard Guide for Drying Behavior of Spent Nuclear Fuel. West Conshohocken, PA: ASTM International.
- Bird, GA. 1983. "Definition of mean free path for real gases." *The Physics of fluids* 26 (11):3222-3223.
- Bird, GA. 1994. "Molecular Gas Dynamics and the Direct Simulation of Gas Flows (Oxford Engineering Science Series)." *Clarendon*.
- Bracey, W, and P Smith. 2012. "Transnuclear drying experience and lessons learned." Proc. ASTM Workshop.
- Brewster, Robert A, Emilio Baglietto, Eric Volpenhein, and Christopher S Bajwa. 2012. "CFD analyses of the TN-24p PWR spent fuel storage cask." ASME 2012 Pressure Vessels and Piping Conference.

- Durbin, Samuel, and Eric R. Lindgren. 2017. Thermal-Hydraulic Results for the Boiling Water Reactor Dry Cask Simulator. ; Sandia National Lab. (SNL-NM), Albuquerque, NM (United States).
- EPRI. 2014. High Burnup Dry Storage Cask Research and Development Project – Final Test Plan. Palo Alto, California: Electric Power Research Institute.
- Fort, James A, David J Richmond, Judith M Cuta, and Sarah R Suffield. 2019. Thermal Modeling of the TN-32B Cask for the High Burnup Spent Fuel Data Project. Pacific Northwest National Lab.(PNNL), Richland, WA (United States).
- Fort, James A, David J Richmond, Ben J Jensen, and Sarah R Suffield. 2019. High-Burnup Demonstration: Thermal Modeling of TN-32B Vacuum Drying and ISFSI Transients. Pacific Northwest National Lab.(PNNL), Richland, WA (United States).
- Hadj-Nacer, Mustafa, Dilesh Maharjan, Minh-Tuan Ho, Stefan K Stefanov, Irina Graur, and Miles Greiner. 2017. "Continuum and kinetic simulations of heat transfer through rarefied gas in annular and planar geometries in the slip regime." *Journal of Heat Transfer* 139 (4).
- Hadj-Nacer, Mustafa, T Manzo, Minh Tuan Ho, Irina Graur, and Miles Greiner. 2016. "Effects of gas rarefaction on used nuclear fuel cladding temperatures during vacuum drying." *Nuclear Technology* 194 (3):387-399.
- Hall, K, and G Zigh. 2019. NUREG/CR-7260, "CFD Validation of Vertical Dry Cask Storage System". Alden Research Laboratory. Inc.

- Hall, Kimbal, Abdelghani Zigh, and Jorge Solis. "Nuclear Dry Cask Storage Container CFD Model Experimental Validation and Uncertainty Quantification." ASME 2019 Verification and Validation Symposium.
- Higley, Megan. 2019. "Effect of Geometry Variation on Temperature Prediction in the TN-32 Used Nuclear Fuel Storage Cask." University of Nevada, Reno.
- Higley, Megan, Mustafa Hadj-Nacer, and Miles Greiner. 2019a. "Effect of the Thermal Expansion of the Used Nuclear Fuel Cask's Basket on Temperature During Vacuum Drying." *Transactions* 121 (1):1721-1724.
- Higley, Megan, Mustafa Hadj-Nacer, and Miles Greiner. 2019b. "Temperature Prediction of a TN-32 Cask with Non-Concentric Basket Subjected to Vacuum Drying." *Packaging and Transportation of Radioactive Materials*.
- Holman, JP. 1997. *Heat Transfer, 8th edition, New York*. New York City, New York: McGraw-Hill.
- Kamichetty, Krishna Kumar, Venkata Venigalla, and Miles Greiner. 2014. "Development, Use, and Accuracy of a Homogenized Fuel Region Model for Thermal Analysis of a Truck Package Under Normal and Fire Accident Conditions." *Journal of Pressure Vessel Technology* 136 (2). doi: 10.1115/1.4026065.
- Large, WS. 1999. Review of drying methods for spent nuclear fuel. Savannah River Site (US).
- Lee, JC, WS Choi, KS Bang, KS Seo, and SY Yoo. 2009. "Thermal-fluid flow analysis and demonstration test of a spent fuel storage system." *Nuclear Engineering and Design* 239 (3):551-558.

- Lin, Jaw Tian, and DR Willis. 1972. "Kinetic theory analysis of temperature jump in a polyatomic gas." *The Physics of Fluids* 15 (1):31-38.
- Maharjan, Dilesh, Mustafa Hadj-Nacer, and Miles Greiner. 2020a. "Implementation and experimental validation of a computational model to predict temperatures and heat transfer of a square array of heated rods enclosed in a pressure vessel filled with rarefied dry helium." *International Journal of Heat and Mass Transfer* 158:120050.
- Maharjan, Dilesh, Mustafa Hadj-Nacer, and Miles Greiner. 2020b. "Temperature measurement of a heated rod array within a square cross section enclosure filled with dry rarefied helium." *International Journal of Heat and Mass Transfer* 148:119033.
- Maharjan, Dilesh, Mustafa Hadj-Nacer, Minh-Tuan Ho, Stefan K Stefanov, Irina Graur, and Miles Greiner. 2015. "Simulation of heat transfer across rarefied gas in annular and planar geometries: comparison of Navier-Stokes, s-model and DSMC methods results." ASME 2015 13th International Conference on Nanochannels, Microchannels, and Minichannels collocated with the ASME 2015 International Technical Conference and Exhibition on Packaging and Integration of Electronic and Photonic Microsystems.
- Manzo, Triton, Mustafa-Hadj Nacer, and Miles Greiner. 2015. "Geometrically-Accurate-Three-Dimensional Simulations of a Used Nuclear Fuel Canister Filled With Helium." Pressure Vessels and Piping Conference.
- McKinnon, MA, TE Michener, MF Jensen, and G R\_ Rodman. 1989. Testing and analyses of the TN-24P PWR spent-fuel dry storage cask loaded with

consolidated fuel. Electric Power Research Inst., Palo Alto, CA (USA); Pacific Northwest Lab ....

Miller, L, D Basu, K Das T Mintz, R Pabalan, G Walter, and G Oberson. 2013.

"Overview of Vacuum Drying Methods and Factors Affecting the Quantity of Residual Water After Drying—Public Version." *US Nuclear Regulatory Commission*.

NRC, U.S. 2003. "Cladding considerations for the transportation and storage of spent fuel." *ISG-11, Rev. 3*.

NRC, U.S. 2010. "Standard review plan for spent fuel dry storage systems at a general license facility." *NUREG-1536 Rev 1*.

Roache, Patrick J. 2009. *Fundamentals of verification and validation*: hermosa publ.

Saling, James H, and Audeen W Fentiman. 2001. *Radioactive Waste Management*. 2nd ed: Routledge.

Schaaf, SA, and PL Chambré. 1961. *Flow of Rarefied Gases*, Vol. 8. Princeton University Press, Princeton, New Jersey.

Song, S, and MM Yovanovich. 1987. "Correlation of thermal accommodation coefficient for engineering surfaces." *ASME HTD* 69:107-116.

Suffield, Sarah R, James A Fort, Harold E Adkins, Judith M Cuta, Brian A Collins, and Edward R Siciliano. 2012. Thermal modeling of NUHOMS HSM-15 and HSM-1 storage modules at Calvert Cliffs nuclear power station ISFSI. Pacific Northwest National Lab.(PNNL), Richland, WA (United States).

- Thomas, Lloyd B, and Sudarshan K Loyalka. 1982. "Determination of thermal accommodation coefficients of helium, argon, and xenon on a surface of zircaloy-2 at about 25 c." *Nuclear Technology* 57 (2):213-219.
- Unterzuber, R, RD Milnes, BA Marinkovich, and GM Kubancsek. 1982. "Spent-Fuel Dry Storage Testing at EMAD (March 1978–1982)." *Prepared for the US DOE Commercial Spent Fuel Management Program Office at the Pacific Northwest Laboratory, Paper No. B-D3339-AG.*
- Yoo, Seung Hun, Hee Cheon No, Hyeun Min Kim, and Eo Hwak Lee. 2010. "Full-scope simulation of a dry storage cask using computational fluid dynamics." *Nuclear Engineering and Design* 240 (12):4111-4122.

# Chapter 3: Uncertainty quantification of thermal gap widths on internal temperatures in the TN-32B HBU demo cask

---

## ABSTRACT

The temperatures of internal components within spent nuclear fuel (SNF) packages must be predicted to ensure they remain within specified limits. These packages have multiple millimeter-scale gaps whose widths are affected by predictable and unpredictable factors. The thermal resistance across these gaps is proportional to their width and it is relatively large because the thermal conductivity of the gas within the packages is significantly lower than that of the metal components. Prior numerical research has demonstrated that variations in gap widths can result in peak cladding temperature varying by as much as 68°C. In this work, a three-dimensional computational fluid dynamics model of the TN-32 SNF package that employs effective fuel region and gap properties is constructed. Forty steady-state simulations are performed for varying widths of nine different gaps within their possible ranges using the Latin Hypercube Sampling method. The best estimate of temperatures and their uncertainties at 63 SNF fuel locations are compared with measurements acquired from the High Burnup Spent Fuel Data project, where other researchers collected temperature data from a TN-32 SNF cask. The results showed that predicted temperatures have 95%-confidence-level interval uncertainties ranging between  $\pm 12^\circ\text{C}$  and  $\pm 21^\circ\text{C}$  due to uncertainties in the gap widths. Most of the measured temperatures, including the peak cladding temperature, are within the confidence intervals of the predicted ones. A proposed linear correlation between the simulated fuel

temperatures and gap widths recreated 95% of the simulation results within  $\pm 1.6^\circ\text{C}$ . This correlation highlighted that uncertainty in the width of the Basket/Rail gap near the package periphery accounts for approximately half of the total temperature uncertainty.

**Key Words:** *Uncertainty Quantification, Thermal Gaps, TN-32, CFD.*

## NOMENCLATURE

$a$  Sensitivity coefficient [ $^\circ\text{C}/\text{mm}$ ]

$N$  Number of samples

$T$  Temperature [ $^\circ\text{C}$ ]

$v$  Axial velocity [ $\text{m}/\text{s}$ ]

$u$  Uncertainty in Temperature [ $^\circ\text{C}$ ]

$x$   $x$ -coordinate [ $\text{m}$ ]

$w$  Width [ $\text{mm}$ ]

$y$   $y$ -coordinate [ $\text{m}$ ]

$z$  Elevation [ $\text{m}$ ]

### *Greek*

Emissivity

Thermal conductivity [ $\text{W m}^{-1} \text{K}^{-1}$ ]

Standard deviation [ $^\circ\text{C}$ ]

Stefan-Boltzmann constant (  $\sigma$  ) [ $\text{W m}^{-2} \text{K}^{-4}$ ]

### *Subscripts*

$0$  Reference

<i>avg</i>	Average
<i>BE</i>	Best Estimate
<i>C</i>	Configuration
<i>eff</i>	Effective
<i>exp</i>	Experimental
<i>G</i>	Gap
<i>gas</i>	Gas
<i>I</i>	Iteration
<i>it</i>	Iterative
<i>L</i>	Thermocouple location
<i>NG</i>	No gaps
<i>PC</i>	Peak Cladding
<i>reg</i>	Linear Regression
<i>sim</i>	Simulation
<i>total</i>	Total

**Abbreviation**

3D	Three-dimensional
B	Base
CFD	Computational Fluid Dynamics
ESCP	Extended Storage Collaboration Program
HBU	High Burnup
LHS	Latin Hypercube Sampling

R	Radial
UQ	Uncertainty Quantification

## **1. Introduction**

Following their removal from nuclear reactors, spent nuclear fuel (SNF) assemblies are cooled in water-filled pools before being transferred to dry storage canisters or casks, such as the TN-32B (Areva 2002; Notz 1988). Cask designs are reviewed, licensed, and certified, in part, for their ability to maintain SNF and other component temperatures within the specified limits under various conditions (NRC 2003, 2010; NRC 2000). Computational fluid dynamic (CFD) simulations are used to predict cask temperatures and to demonstrate regulatory compliance (Hall and Zigh 2019; Fort, Richmond, Cuta, et al. 2019). Typically, these CFD models are designed to conservatively overpredict component temperatures but by unknown margins (Fort, Richmond, Cuta, et al. 2019). This unknown conservatism has led to the extended storage of SNF in water pools beyond what may be necessary. However, reducing this conservatism requires developing accurate models that are experimentally validated and conducting uncertainty quantification (UQ) to estimate the possible variation in component temperatures due to uncertainty in input parameters (such as gap widths, material properties, component dimensions, etc.) (ASME 2009). Few full-scale instrumented experimental demonstrations of SNF casks have provided data that may be utilized to validate CFD models (Creer et al. 1987; Durbin and Lindgren 2017; Hanson 2018).

The High Burnup (HBU) Spent Fuel Data Project is one of these demonstrations that is currently collecting data on a TN-32B SNF cask through all storage operations (EPRI 2014). The TN-32B cask used in the HBU project is a multi-layered structure designed to store up to thirty-two 17×17 pressurized water reactor SNF assemblies. In this project, the cask was loaded with SNF assemblies and instrumented with thermocouple lances to collect temperature data at 63 internal locations along seven assemblies. Steady-state internal temperatures were reached and recorded after a two-week thermal soak. Attempts to use this dataset to validate CFD models have been made and several research groups have qualitatively reproduced the temperature profiles (Fort, Richmond, Jensen, et al. 2019; Fort, Richmond, Cuta, et al. 2019; Akkurt 2022; Hanson 2018; Csontos 2020; Hall and Zigh 2019). However, uncertainties in model inputs, such as decay heat, dimension of components and thermal gaps, material properties, and boundary conditions, have yielded significant variability in predicted temperatures (Hall and Zigh 2019; Mittal et al. 2014; Fort, Richmond, Cuta, et al. 2019; Akkurt and Csontos 2020; Higley, Hadj-Nacer, and Greiner 2021, 2022). To address this variability, a collaborative initiative was established through the Extended Storage Collaboration Program's (ESCP) International Thermal Modeling Benchmark Project (Akkurt and Csontos 2020). Under this project, various modeling groups were provided specific information and assumptions pertaining to the HBU Project and TN-32B cask. Different groups employed different CFD codes and had to make some assumptions about information that was not supplied (deemed to be confidential or inconsequential). However, even within this coordinated effort, a persistent disparity in temperature predictions was observed (Akkurt 2022). The large discrepancies between these studies may be attributed to representations of boundary

conditions and millimeter-scale gas-filled gaps, as well as human error and variation between utilized codes (Fort, Richmond, Cuta, et al. 2019; Akkurt 2022).

Hall and Zigh, 2019 (Hall and Zigh 2019) conducted a UQ analysis to estimate the uncertainty on temperature predictions of the TN-32B cask used in the HBU project. The study estimated temperature uncertainties stemming from spatial discretization, iterative process, and 20 input parameters using a porous fuel region CFD model. They used a local uncertainty method based on the sensitivity coefficient technique where one input parameter was varied at a time while keeping all the others at their nominal values. They found a total temperature uncertainty of 73°C, with 63°C attributed to variation in thermal gap widths (Hall and Zigh 2019). However, it is essential to recognize that the sensitivity coefficient method typically assumes that the effects of input parameters, such as thermal gap widths, are uncorrelated. In other words, it assumes that heat transfer through one gap does not affect the heat transfer through another. Nonetheless, this assumption was found to be inaccurate, particularly in the case of the TN-32B cask, as highlighted in that study. That study showed that the temperature uncertainties due to thermal gap width variations could vary between 37°C and 72°C, depending on the extent of correlation between the gaps. This represents a significant range of uncertainty considering that recent applications for new cask designs were submitted with maximum temperatures within 10 to 20°C of regulatory limits (Hall and Zigh 2019).

In this work, a full three-dimensional (3D) porous fuel region model of the TN-32B cask used in the HBU project is constructed and used to conduct a UQ analysis of the effect of uncertainty in the width of nine thermal gaps on temperature prediction at the 63 measured locations. The Latin Hypercube Sampling (LHS) method is used to sample the

nine gaps within their possible width ranges to account for the combined effect of multiple gap uncertainties on temperature prediction uncertainty. The simulations are conducted under the same conditions as the HBU experiment for direct comparison with experimental data. Forty gap configurations were simulated where each of the gaps' widths were sampled from zero to the largest considered gap width. The best estimate of temperatures and their associated uncertainties are calculated for a 95% confidence interval. A linear regression analysis is performed to determine which gap uncertainties have the most significant effects at each measurement location. The bounding cases for configurations where all gaps are closed or at their maximum values are compared with linear regression results. While this work is not a full uncertainty analysis, it is the first effort into exploring the combined effects of the thermal gaps on temperature prediction in the TN-32B cask.

## **2. Computational Model and Boundary Conditions**

Figure 3.1 shows the computational domain of the 3D CFD model of the TN-32B cask used in this work. This model was constructed in ANSYS/Fluent using geometry, dimensions, and material properties from the ESCP project (Akkurt and Csontos 2020). The fuel regions are modeled as homogenous porous heat-generating blocks with effective properties.

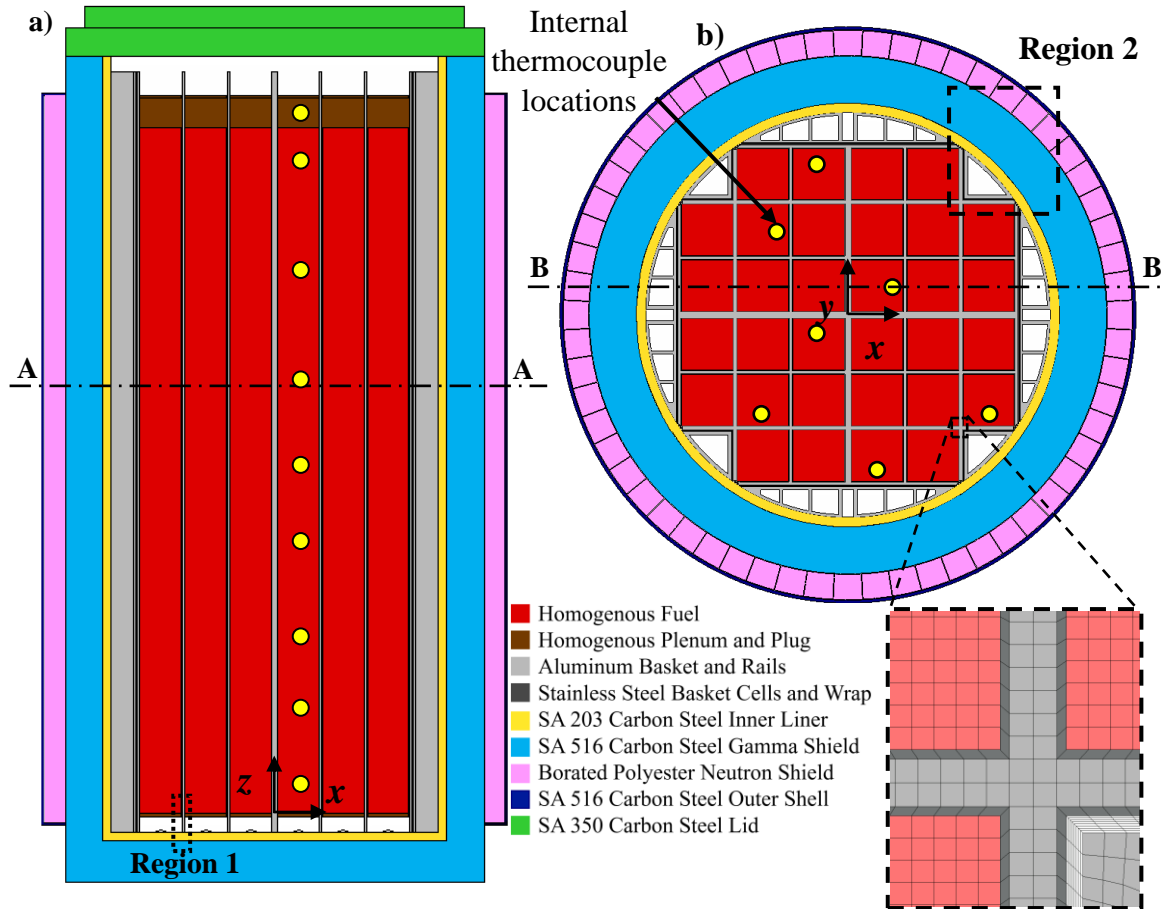


Figure 3.1. TN-32B SNF cask 3D model showing components, internal thermocouple locations, mesh, and coordinate system from (a) vertical and (b) horizontal cross-sections.

The fuel regions in the TN-32B model are contained within stainless steel tubes that are surrounded by an aluminum basket. The thin BORAL plates layered in the basket are modeled as aluminum as they have a similar thermal conductivity. An outer stainless steel wraps the basket and represents its final layer. Drain holes are cut into the bottom of the basket allowing for water draining and gas circulation. The basket is centered within a circular carbon steel inner liner. Aluminum rails are inserted between the basket and inner liner to provide support to the basket and accommodate the circular shape of the inner liner. A thick carbon steel gamma shield encloses the inner liner. Outside the gamma

shield, aluminum boxes filled with polyester resin are used to attenuate neutrons. Surrounding the aluminum boxes is an outer shell made of carbon steel and coated with a high emissivity paint to enhance heat release to the environment. At the top of the cask, a carbon steel lid is bolted to the cask body. The cask has an outer diameter of 2.48 m and a height of 4.67 m. The origin of the  $x$ ,  $y$ ,  $z$  reference frame is centered at the bottom of the fuel regions.

The mesh employed in the CFD model predominantly consists of highly structured, hexahedral cells, as shown in the detailed region of Fig. 3.1. In total, the model comprises 20.6 M cells with an average and minimum orthogonal quality of 0.98 and 0.17, respectively. Previous research conducted by the authors with two-dimensional meshes of the TN-32B (Higley 2019) and 3D meshes of the TN-24 (Trujillo 2017) has indicated small temperature uncertainties due to mesh size. Additionally, the finest mesh employed in the Hall and Zigh, 2019 TN-32B model had 19 M cells and was estimated to incur  $0.3^{\circ}\text{C}$  of uncertainty in temperature prediction; two orders of magnitude less uncertainty than that attributed to thermal gaps (Hall and Zigh 2019). Therefore, it was inferred that a mesh sensitivity analysis for the TN-32B model used in the current work is not required.

Steady-state simulations that model conduction, convection, and radiation heat transfers are conducted. The thermal conductivities used for the solid components of the cask are temperature-dependent and obtained from (Inc.). The effective porous flow properties of the fuel regions were provided by the ESCP project (Akkurt and Csontos 2020) and their radial effective thermal conductivity was obtained from the TN-32B Final Safety Analysis Report (FSAR) (Areva 2002). The fuel regions' axial effective thermal

conductivity was calculated using a parallel conduction thermal circuit analysis that uses an area-weighted average of the solid and gas region material thermal conductivities (Zigh and González 2017). Helium gas properties were calculated using the kinetic theory. Radiation heat transfer is simulated using the Discrete Ordinances radiation model. The cask is filled with helium at a pressure of 223 kPa, consistent with the HBU experiment. The TN-32B cask is stored vertically, thus gravity acts in the negative  $z$ -direction as shown in Fig. 3.1. The effect of natural convection on the predicted temperatures is investigated by conducting simulations with natural convection enabled and disabled. The natural convection flows within the cask are simulated using a laminar model as the highest Reynolds number is estimated to be  $\sim 1300$ .

The fuel assemblies in the TN-32B HBU experiment generate different amounts of heat with a non-uniform axial heat generation profile. Figure 3.2a shows the heat generation rates used in the experiment and applied in the simulations along with the numbering scheme of the fuel regions. The seven highlighted fuel regions contain thermocouple lances that were used to measure the temperature at nine axial locations. These measured data will be compared with simulation results. The solid line in Fig. 3.2b shows the actual axial heat generation profile of the fuel assembly. This profile was approximated with a polynomial function (shown with a dashed line) for ease of implementation in the simulations.

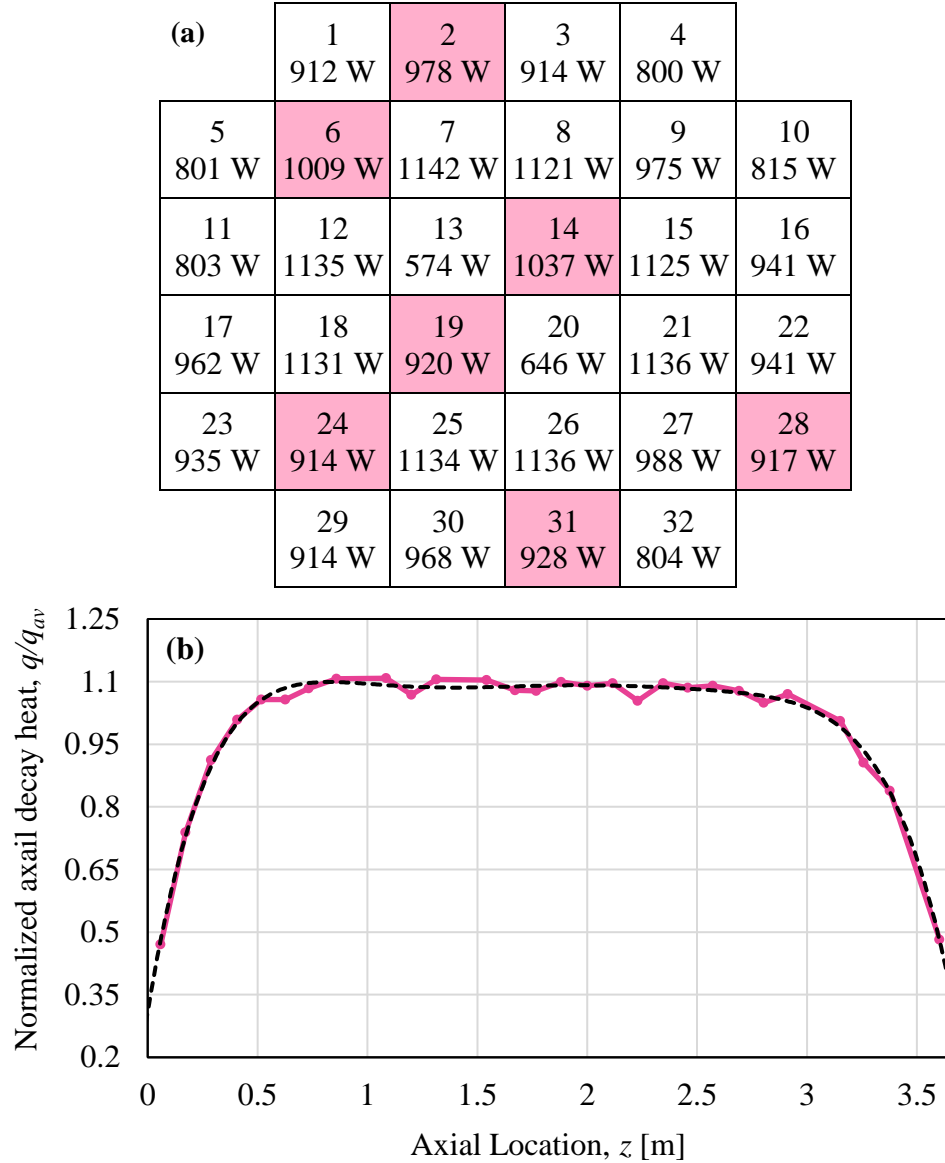


Figure 3.2. Heat generation rates and numbering convention for each of the 32 fuel assemblies of the HBU project cask. Instrumented fuel assemblies are highlighted.

The surrounding ambient temperature of the HBU experimental cask was not controlled and varied with time and elevation. In the simulations, the cask is assumed to dissipate heat to the surroundings by convection and radiation to an average 24°C measured ambient temperature. An emissivity value of 0.9 is used for the outer surfaces

of the cask, consistent with the ESCP project (Akkurt and Csontos 2020). Similar to Hall and Zigh, 2019 (Hall and Zigh 2019), constant convective heat transfer coefficients of 5 W/m<sup>2</sup>-K on horizontal upward-facing and vertical outer surfaces and 10 W/m<sup>2</sup>-K on horizontal downward-facing outer surfaces are implemented. Hall and Zigh, 2019 found that internal temperatures of the TN-32B cask are not significantly sensitive to the convective heat transfer coefficient variations (Hall and Zigh 2019).

### **a. Thermal Gaps**

The nine thermal gaps considered in this study are selected based on the local uncertainty analysis conducted by Hall and Zigh 2019. These gaps were found to have the most significant effect on temperature compared to other parameters, such as ambient conditions, emissivities, effective properties, and decay heat (Hall and Zigh 2019). In the current study, it is assumed that gap widths are independent of one another, range from completely closed to their maximum value in the TN-32B FSAR (Areva 2002), and have a uniform width. The effects of the gaps are investigated when all the gaps are perturbed simultaneously, which incurs a higher computational cost than the local uncertainty method, but allows for a more accurate estimation of temperature uncertainties because the combined effects of the gaps are considered.

The nine gaps considered in the current study are depicted in Fig. 3.3 and listed in Table 1 along with their numbering scheme, abbreviation, gas fill, and maximum considered width. These gaps are categorized into four groups: basket gaps, base gaps, peripheral gaps, and the basket/rail gap. In the basket gap group, there are two different gaps; Al/Al gaps (#1) at the interfaces between the aluminum plates within the basket,

and Al/SS gaps (#2) between the stainless-steel tubes and aluminum plates of the basket. In the base gap group, there are two different gaps; B-Basket/In-Liner gaps (#3) at the contact between the bottom of the basket and the inner liner, and B-In-Liner/Gamma (#7) between the bottom of the inner liner and the gamma shield. In the peripheral gap group, there are four different radial gaps; R-Rail/In-Liner (#5) between the supporting rails and the inner liner, R-In-Liner/Gamma gap (#6) between the inner liner and gamma shield, Gamma/Al-Box (#8) between the gamma shield and resin boxes, and Al-Box/OS (#9) between the resin boxes and outer shell. In the basket/rail gap group, there is only one gap between the basket and supporting rails, called the Basket/Rail gap (#4), which also includes the gap between the corner of the basket and the inner liner (see Fig. 3.3).

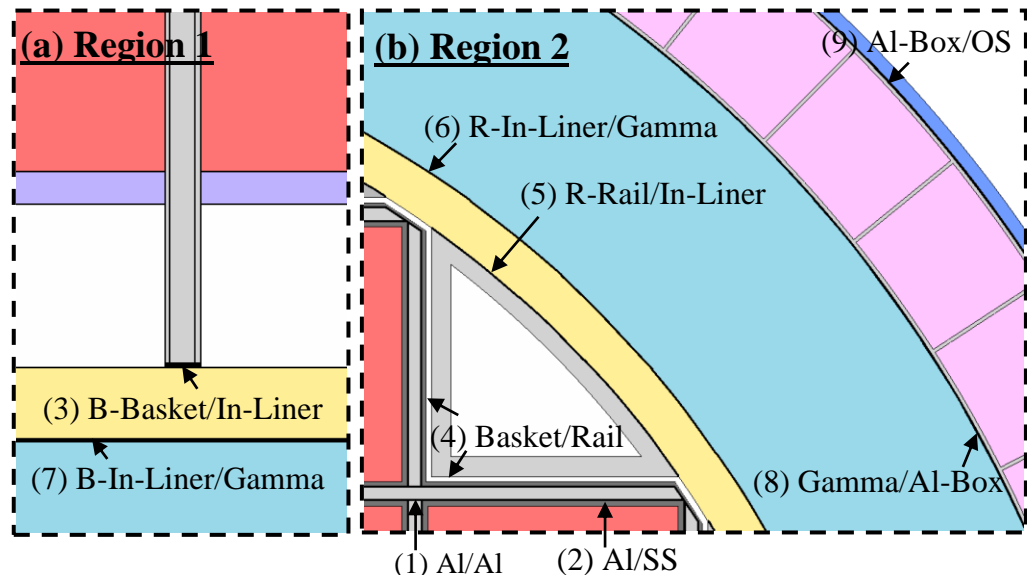


Figure 3.3. Details of (a) Region 1 and (b) Region 2 shown in Fig. 3.1, depicting the nine gaps considered in this study.

With the exception of the basket-rail gap, all gaps are modeled implicitly as thermal resistances between solid surfaces. The effective thermal conductivity of these implicit

gaps is based on a thermal resistance model that includes the effect of radiation and conduction as

$$\frac{1}{R_{cond}} = \frac{1}{L} \left( \frac{k_1}{\delta_1} + \frac{k_2}{\delta_2} \right)$$

In this expression,  $k$  is the thermal conductivity of the gas filling the gap,  $L$  is the width of the gap,  $\sigma$  is the Stefan-Boltzmann constant,  $T_{avg}$  is the average of the surface temperatures of the gap walls, and  $\epsilon_1$  and  $\epsilon_2$  are the emissivities of the two walls of the gap. Equation (1) assumes the temperature difference between the gap walls is small compared to their average temperature, which is valid for all the gaps considered in this study.

Table 3.1. Thermal gaps considered in this work (illustrated in Fig. 2) with their assigned number, description, abbreviation, fill gas, and maximum width.

Gap #, $G$	Description	Abbreviation	Fill Gas	Max. Gap Width, [mm]
1	Aluminum to Aluminum Basket Plates	Al/Al	Helium	0.508
2	Aluminum to Stainless Steel Basket	Al/SS		0.508
3	Base Basket to Inner-Liner	B-Basket/In-Liner		6.350
4	Basket to Rail	Basket/Rail		4.775
5	Radial Rail to Inner-Liner	R-Rail/In-Liner		0.254
6	Radial Inner-Liner to Gamma Shield	R-In-Liner/Gamma	Air	0.033
7	Base Inner-Liner to Gamma Shield	B-In-Liner/Gamma		3.175
8	Gamma Shield to Aluminum Resin Box	Gamma/Al-Box		0.254
9	Aluminum Resin Box to Outer Shell	Al-Box/OS		0.254

The Basket/Rail gap is explicitly modeled as a 4.78 mm gap. To vary the width of this gap for sampling purpose using the LHS technique, the temperature-dependent thermal conductivity of the helium in the gap region is modified by the ratio of the explicit width value to the sampled width value. Radiation is calculated across the Basket/Rail gap directly by ANSYS/Fluent using the radiation model. Forty gap configurations are simulated where all the nine gaps are simultaneously perturbed. We call the *nominal* configuration, the configuration in which all gap widths are set to half of their maximum width defined in Table 1.

### **3. Results**

In this section, the simulation results for the nominal configuration are first presented and discussed for convergence, temperature profiles, and the effect of including natural convection heat transfer on predicted temperatures. Then, the UQ method employed in the work is briefly described, and the results of the uncertainty analysis are discussed and compared with experimental data followed by a proposed linear regression method to predict the simulation results.

The following nomenclature is used to distinguish between the thermocouple locations within the fuel assemblies. As previously mentioned, the fuel assemblies are numbered from 1 to 32, as depicted in Fig. 2a. However, only assemblies 2, 6, 14, 19, 24, 28, and 31 contain thermocouple lances for temperature measurements. Each of the lances measures temperatures at nine different elevations, as shown in Fig. 1a. These locations are numbered 1 through 9, starting from the bottom to the top. For example, the

thermocouple A14-E6 is in Assembly #14 at elevation #6. This specific thermocouple corresponds to the location where the experimental  $T_{PC}$  is measured.

**a. Nominal Configuration**

Figure 4 shows the simulation temperatures over 1500 iterations at three thermocouple locations (A14-E6, A14-E9, and A28-E9) for the nominal configuration that includes natural convection heat transfer. The temperature at the location of the experimentally measured  $T_{PC}$  (A14-E6) displays the typical convergence behavior after ~100 iterations with very little variation over 1500 iterations. This behavior is common amongst all locations, except for those located at the highest elevation, E9 ( $z \sim 3.71$  m). At this elevation, as shown by A14-E9 and A28-E9, temperature varies with iteration over all 1500 iterations with no steady behavior. This means that increasing the number of iterations does not reduce temperature variability. The results also indicate that the unsteady behavior increases with temperature at this elevation. The variation of temperature with iterations at this elevation is caused by the upward helium flows through the assemblies mixing in the open regions above the assemblies and creating an unsteady behavior. For the case without natural convection, the temperatures at all locations converge to constant values over iterations.

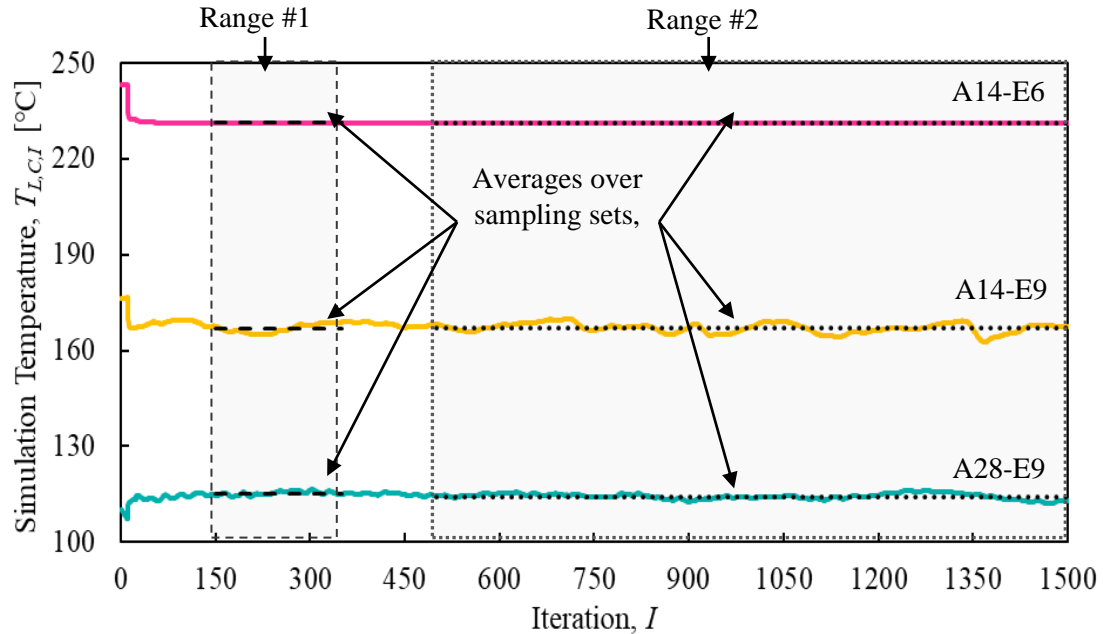


Figure 3.4. Simulation temperature at three thermocouple locations versus iteration for the nominal configuration. Dashed and dotted lines show the average temperature within two sample sets.

For the simulations that include natural convection, the temperatures from all thermocouple locations are averaged over many iterations, and their 95% standard deviation from the average value is considered as the iterative uncertainty. Average temperatures, their uncertainties, and the computational time are sensitive to and directly dependent on the number of iterations. To determine the minimum required number of iterations that reduce the iterative uncertainties and the computational time, a convergence test was performed on the nominal configuration. Average temperatures and iterative uncertainties were calculated over the two iteration ranges (#1 and #2) shown in Fig. 4. The first range considered iterations from 150 to 350, and the second considered iterations from 500 to 1500. The iterative temperature average,  $\bar{T}_{L,C,I}$ , over these ranges is calculated as

where,  $T_{i,j,k}$  is the temperature calculated at a given location,  $i$ , configuration,  $j$ , and iteration,  $k$ , and  $N$  is the number of iterations in the considered iteration range. The iterative uncertainty,  $U_{iter}$ , for each location and configuration is calculated using two population standard deviations (  $\sigma$  ) of the temperatures from the average value in each iterative range as

$$U_{iter} = \frac{\sigma_1 - \sigma_2}{\sqrt{2}}$$

For the nominal configuration, the largest difference between the temperature averages of the two iteration ranges is less than 1°C for all locations. In most of the locations (56 out of 63), this difference is below 0.2°C. The largest difference in iterative uncertainties between the two ranges is 1.6°C with most of the locations (59 out of 63) having a difference of less than 0.5°C. Therefore, it was determined that 350 iterations were sufficient for the simulations, given that the results are averaged over the last 200 iterations.

Figure 5 shows vertical (B-B) and horizontal (A-A) cross-section temperature contours at the planes passing through the location of the experimentally measured  $T_{PC}$  for the nominal configuration at the end of iteration 350. The contours show that the hottest regions are near the axial and radial cask centers, but that the maximum experimentally measured temperature is located at a higher elevation than the simulated maximum temperature. This may be due to an underprediction of the natural convection flow in the simulation as will be discussed later. Assembly 14 has the highest predicted

temperature, consistent with experimental measurements. Effects of the individual heat generation rates (shown in Fig. 2) can be seen when comparing the temperature profiles in assemblies 13, 14, 19, and 20 (centermost assemblies), with assemblies 14 and 19 displaying higher temperatures due to their higher heat generation rates. The effect of some of the thermal gaps, such as the inner liner to gamma shield gap (#7 in Fig. 3) at the bottom of the cask can be seen from the vertical temperature contour as a sharp temperature gradient at this location.

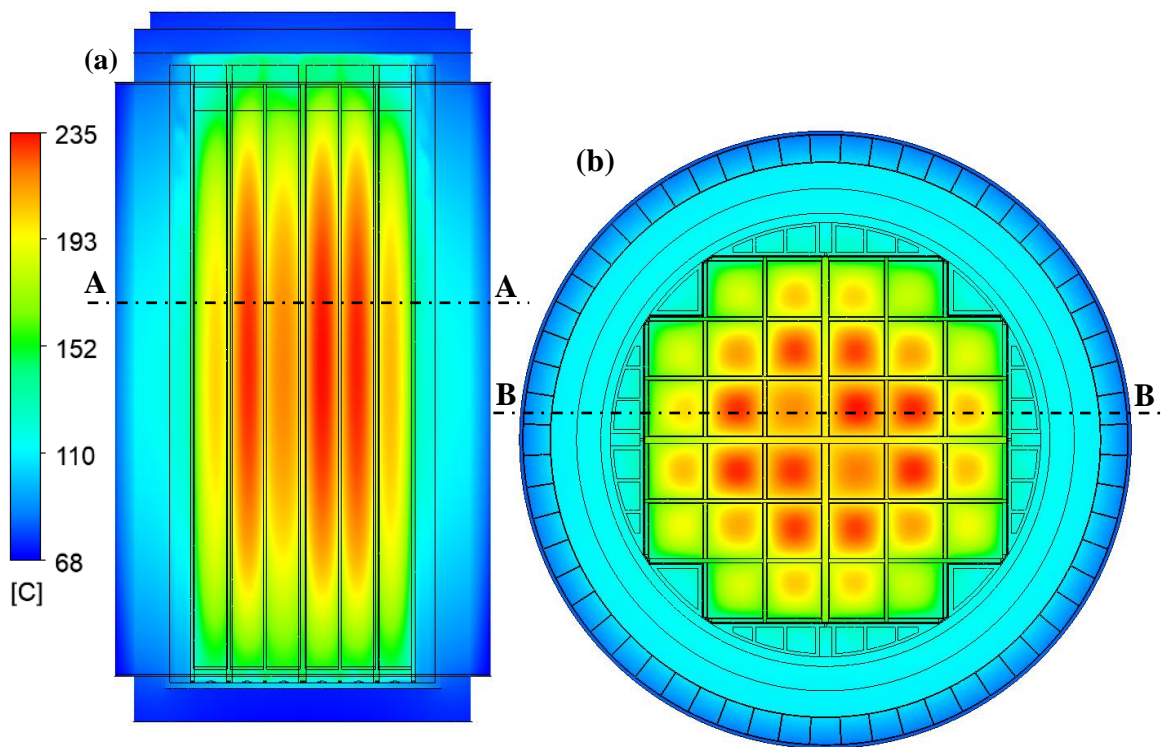


Figure 3.5. Temperature contours for the nominal gap configuration in the (a) B-B and (b) A-A planes shown in Fig. 3.1 at iteration 350.

Figure 3.6 is a 3D plot of the simulated vertical speed,  $v$ , versus  $x$  and  $y$  in the A-A plane (shown in Fig. 3.5a) for the nominal configuration that includes the effect of natural convection. The surface colors indicate the simulated local temperatures. Figure 3.6a

shows the flow in all the open regions of the cask, including the aluminum support rail openings. In this figure, the dominance of the flows in the support rail openings is clearly seen with flows as high as 0.4 m/s in the upward and downward directions, which is approximately an order of magnitude greater than the flows through the fuel assemblies. The supporting rail openings are closed at the bottom; therefore, there is a simultaneous upward and downward flow in those openings caused by natural circulation. Higher velocities occur in the downward direction where the coolest local temperatures occur. Figure 3.6b shows the helium flow in the fuel regions only. Both upward and downward flows are seen in the fuel regions, with upward flows occurring in all fuel assemblies (mostly in the centermost assemblies) and some downward flows occurring in peripheral assemblies. This flow circulation pattern is due to the explicit modeling of the drain holes at the base of the fuel basket that connect the neighboring fuel regions and allow for mass exchange between these regions. It is expected that if drain holes are modeled at the bottom of the supporting rails, higher flow velocities will occur in the fuel assemblies, which may increase the effect of natural convection on temperatures.

Previous works included the effects of natural convection in the heat transfer simulations of the TN-32B, but because of the low internal pressure of 2.2 atm and the low density of the backfill gas, i.e. helium, the authors conclude that natural convection in the TN-32B does not significantly affect  $T_{PC}$  (Fort, Richmond, Cuta, et al. 2019; Hall and Zigh 2019). In the current work, the effect of natural convection is investigated to verify if it has a significant effect on all cask temperatures, not just  $T_{PC}$ . To do this, a simulation using the nominal configuration is conducted with natural convection heat transfer disabled and results are compared to the case with natural convection enabled.

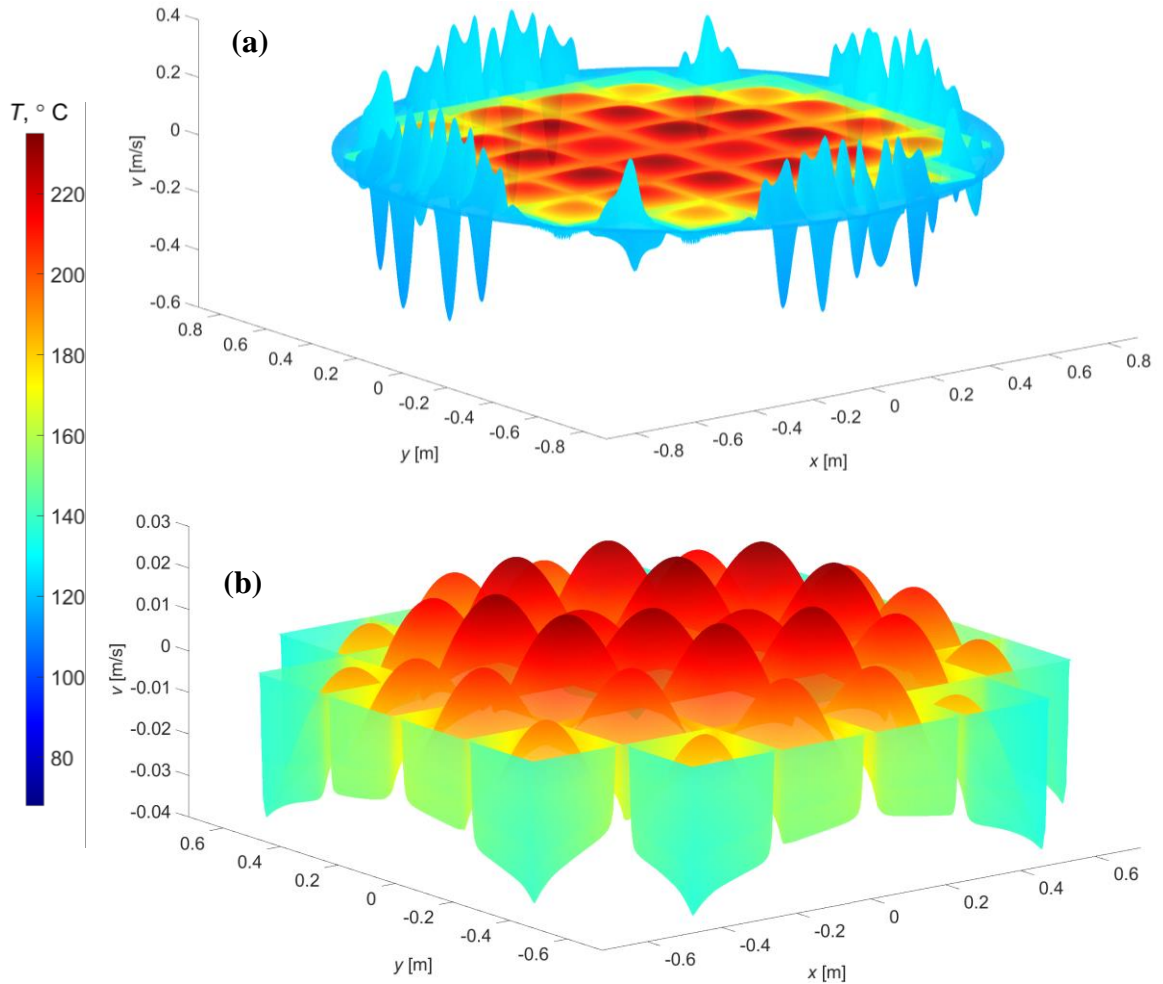


Figure 3.6. 3D Axial velocity plot with a temperature contour overlay at iteration 350 in the A-A plane shown in Fig. 1 for the nominal gap configuration for (a) all open regions and (b) only fuel regions.

Figure 3.7 shows the plot of simulated temperatures at each of the thermocouple locations without natural convection as a function of the simulated temperature at the same locations with natural convection. The results in this plot, are divided into three elevation groups according to the axial thermocouple locations: lower (0-1m), middle (1m-3m), and upper (3m-5m) elevation groups. The solid line represents the case in which the no-natural convection and the natural convection simulation results are the

same. The error bars represent the iterative uncertainty calculated using Eq. 3. For the middle and lower elevation groups and the case without natural convection, the error bars are smaller than the size of the symbols.

Figure 3.7 shows that the effect of natural convection is negligible for the middle elevation group where  $T_{PC}$  occurs. The temperature predicted by the natural convection and no natural convection cases are very similar and lie closely on the solid line. However, for the lower elevation group, the temperatures predicted by the case without natural convection are systematically higher than those predicted by the case with natural convection, with a difference as high as 19°C. For the upper elevation, the temperatures predicted by the case without natural convection were higher in the locations close to the periphery of the cask (coldest regions) and lower in the locations close to the innermost assemblies (hottest regions). These observed trends are caused by natural convection flows, which tend to reduce temperatures at lower elevations and increase them at upper elevations. This result supports the conclusion that including natural convection does not strongly affect the prediction of  $T_{PC}$ . However, it does significantly affect temperature predictions at the upper and lower elevation locations.

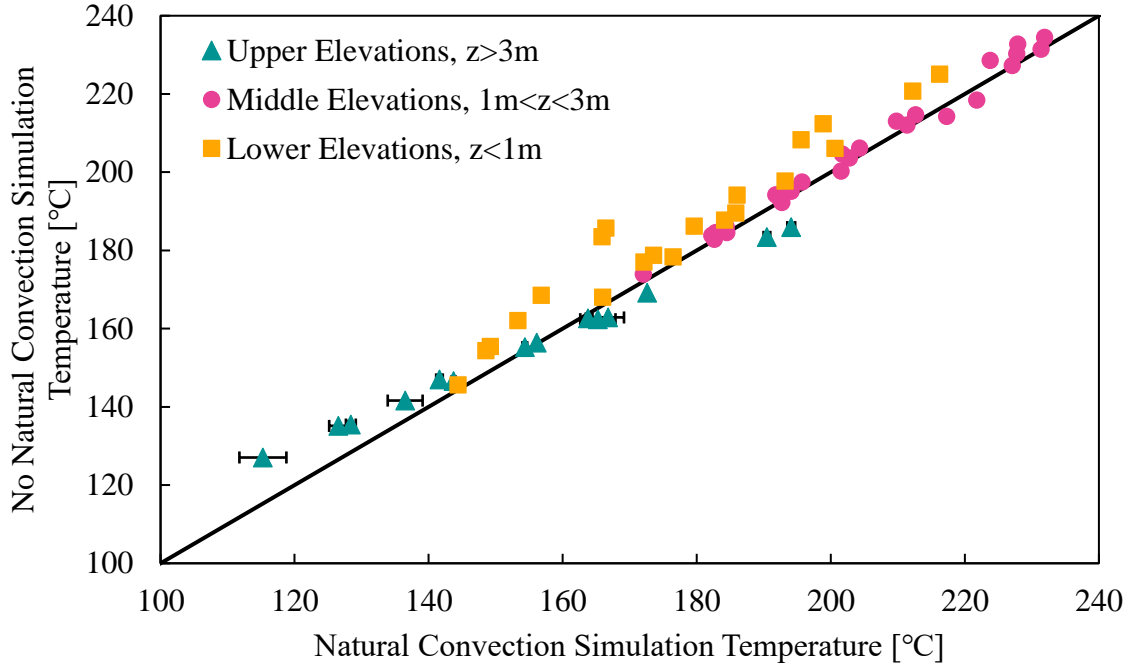


Figure 3.7. Comparison of the temperature predictions between simulations with and without natural convection at all thermocouple locations for the nominal configuration. Error bars represent the iterative uncertainties.

## b. Effects of Uncertainties

### i. Uncertainty Quantification Methods

In this work, the global UQ method is used to predict the best estimate of temperatures and their uncertainties due to thermal gap width variations at all thermocouple locations. This method considers the combined effect of all thermal gaps on temperatures by simultaneously varying their widths. The LHS technique is used to sample within individual gap width bounds. Each gap is uniformly divided into 40 equally sized intervals and a multidimensional (9D) matrix is then generated. A value is randomly selected from each interval, ensuring that the entire range of each gap is considered, which results in one sample point per interval. This process is repeated for each gap, and the sample points are randomly paired in a way that ensures that no pair of

points shares the same value for any of the variables. Essentially, the samples for each parameter are permuted to create unique combinations. This leads to 40 different configurations that provide a comprehensive coverage of the entire multidimensional input space. The LHS sampling method is used because it typically requires fewer samples for the same accuracy as Monte Carlo Sampling and guarantees that the sample space is explored uniformly (Adams et al. 2022).

Simulations are conducted for the 40 gap configurations to predict the best-estimate temperatures and their variation due to iterative and input (gap width) uncertainties. The best estimate for temperature at each location,  $T_{best}$ , is calculated as the average of the iterative temperature averages ( $T_{iter}$ , Eq. 2) over all configurations ( $N_C = 40$ ) as

---

The overall iterative uncertainty in temperature at each location due to its variation as a function of iterations,  $\sigma_{iter}$ , is calculated as the average of configuration iterative uncertainties ( $\sigma_{iter,C}$ , Eq. 3) for all configurations as

---

The input uncertainty in this work is considered only due to uncertainty in the width of thermal gaps, because in a previous work, these were shown to cause more uncertainty than any other input parameter (Hall and Zigh 2019). The input uncertainty in temperature prediction due to gap widths at each location,  $\sigma_{input}$ , is calculated as twice the population standard deviation of the iterative average temperatures,  $T_{iter}$ , from the best estimate temperature,  $T_{best}$ , over all configurations as

The total simulation uncertainty on the best estimate for the temperature at each location,  $T_{\text{total}}$ , is calculated as the square root of the sum of the squares of the overall iterative and input (gap) uncertainties. It can be shown that

because the covariance in iteration and gap uncertainty is on the order of  $10^{-15}$ . This means that uncertainties due to iteration and gap width can be considered separately.

## ii. Best-Estimate Temperature Predictions

Figure 3.8 shows the axial temperature profiles in four of the experimentally instrumented assemblies (2, 6, 14, and 28, see Fig. 3.3 for assembly numbering). The solid lines are for the best estimate of temperature predictions,  $T_{\text{best}}$  (Eq. 4), obtained from the simulations. The associated total uncertainty,  $T_{\text{total}}$  (Eq. 7), at each thermocouple location is shown with error bars. The dotted lines are the measured temperature profiles obtained from the HBU experiment (Hanson 2018) at the same assemblies. The error bars represent the experimental uncertainty, which was reported to be  $1.4^{\circ}\text{C}$  plus 0.3% of the measured temperature value (Csontos 2020).

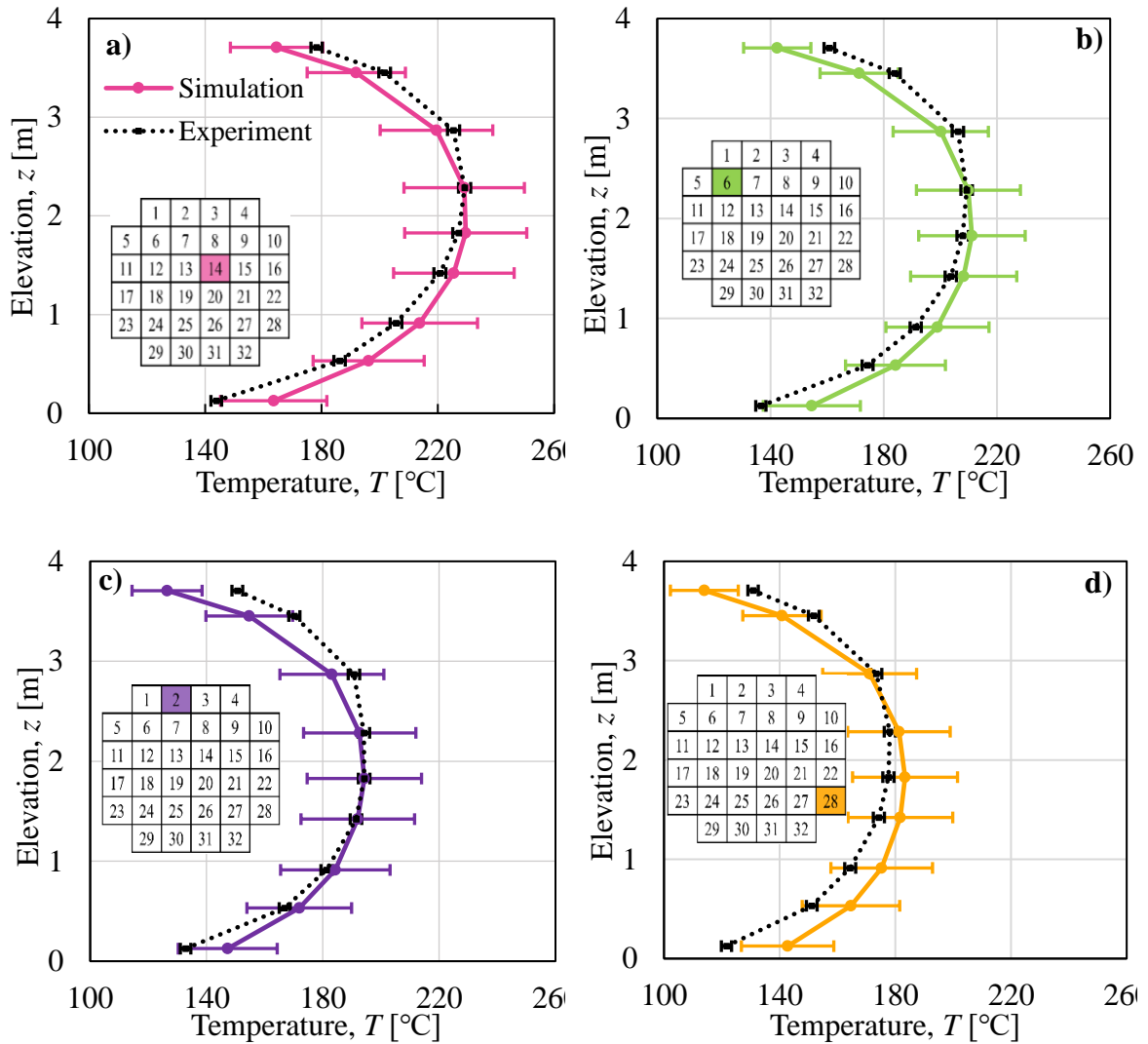


Figure 3.8. Simulated and experimental temperature profiles for assemblies a) 2, b) 6, c) 14, and d) 28. The solid line is for simulation results and the dotted line is for experimental results. The simulation and experimental uncertainties are shown with error bars.

As expected, the simulation and experimental temperature profiles have a parabolic shape. Because assembly 14 is one of the innermost with the highest heat generation, it experiences the highest temperatures compared to all other assemblies. Assembly 28 experiences the lowest temperatures among the four assemblies shown in Fig. 3.8,

because it is located on the periphery of the basket with two of its sides bordering the Basket/Rail gap. The axial location of  $T_{PC}$  in assembly 14 obtained from experimental measurements is at a higher elevation ( $\sim 2.28$  m) than simulation results ( $\sim 1.82$  m). In assembly 14, all experimental data are within the uncertainty range of the simulation results. For the other assemblies (2, 6, and 28), most of the experimental data are within the simulation uncertainty ranges, except for the highest and lowest elevations (E1 at  $\sim 0.13$  m and E9 at  $\sim 3.71$  m, respectively). Overall, the simulation results predict the experimental data within the uncertainty range for 51 of the 63 thermocouple locations, with exceptions occurring at the highest or lowest elevations.

At elevations above approximately 2.3 m, the best-estimate simulation temperatures underpredict the experimental data, while below 2 m, they overpredict them. As discussed in Sec. 4.1, this may be an indication that the natural convection effect is being underpredicted in the simulations. Enhanced natural convection would elevate the peak cladding temperature location and increase the temperatures at higher elevations and reduce them at lower elevations. Natural convection may be underpredicted due to the non-modeling of the drain holes in the support rails and the inadequate representation of the helium surrounding the assemblies in the porous effective flow properties. This may be investigated in future work.

Figure 3.9 is a direct comparison of the best-estimate simulation temperatures versus experimentally measured temperatures for all 63 thermocouple locations. Simulation and experimental uncertainties are included as error bars, but some of the bars were removed for clarity. Similar to Fig. 3.7, the thermocouple locations are divided into three groups (upper, middle, and lower) depending on their axial location. If the simulations perfectly

reproduced the experimental results, all the data points would lie perfectly on the line shown by a solid line.

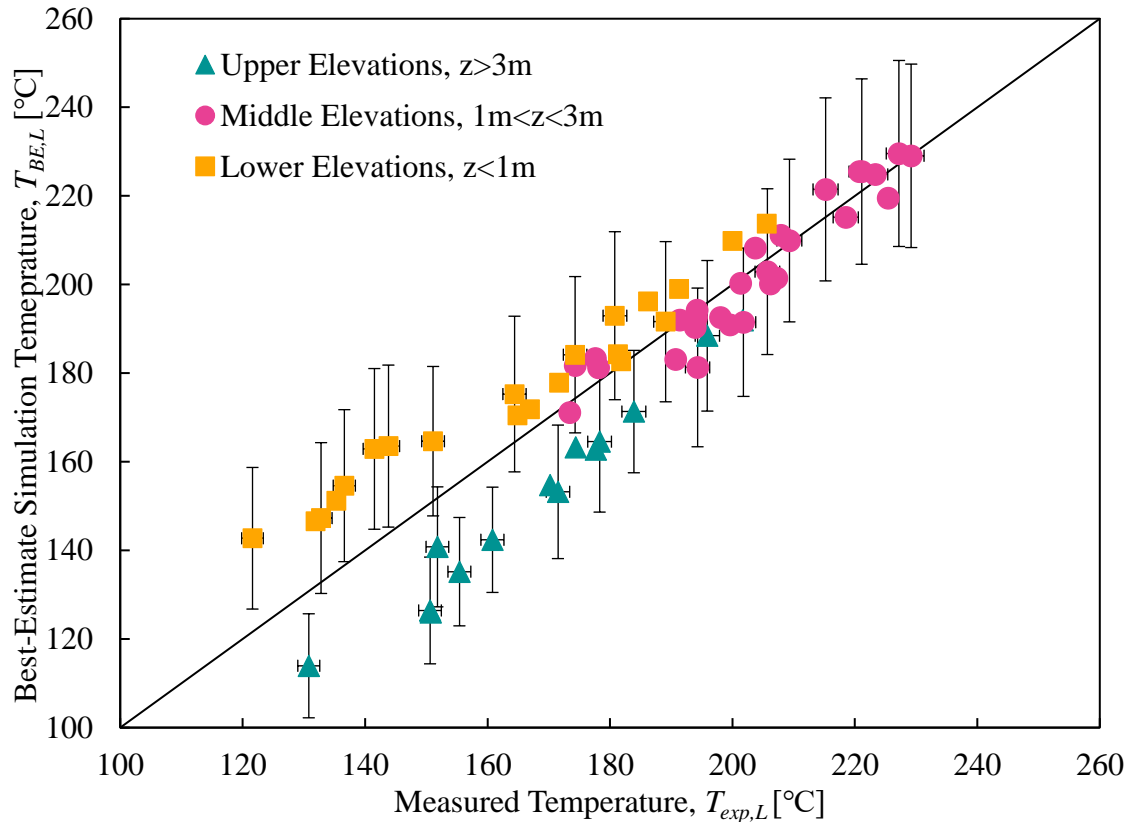


Figure 3.9. Best-estimate simulated temperatures as a function of experimental temperatures.

There is a good agreement between simulation and experiment temperatures in the middle elevation, which corresponds to the locations of the highest temperatures. At the upper elevation, all best-estimate simulation temperatures are lower than experimental ones, and at lower elevations, they are all higher. The disagreement between the simulation and experimental temperatures at these elevations increases with the decrease in temperature, leading some measurements to not be captured by simulation uncertainties.

Figure 3.10 shows the simulation uncertainty contribution of each source (iterative, , and gap, ) and the total uncertainty ( ) as a function of the best-estimate simulation temperature for all thermocouple locations. The gap uncertainties are more significant than the iterative uncertainties at all temperatures. The gap uncertainties increase primarily with temperature but decrease secondarily with elevation (not shown). This means that the gap width variations have a larger effect on the middle elevation locations than the upper and lower locations. Also, their effect is larger at the lower elevations than the upper elevations, primarily due to the base gaps (#3 and #7, see Fig. 3.3). The gap uncertainty ranges from  $\pm 12^{\circ}\text{C}$  to  $21^{\circ}\text{C}$ , with an average of  $\pm 18^{\circ}\text{C}$ . The iterative uncertainty is only significant at the highest elevation (E9), with a maximum value of  $1.5^{\circ}\text{C}$ . It is an order of magnitude smaller than the gap uncertainty and is due to the mixing of the natural convection flows at the top of the basket, as previously explained. The contribution of the iterative uncertainty to the total uncertainty is minimal compared to that of the gap uncertainty. Therefore, it may be concluded that an initial estimate of iterative uncertainty is sufficient to characterize iterative uncertainty for many configurations and that the effect of iterative uncertainty may be neglected when conducting UQ analysis of cask temperatures.

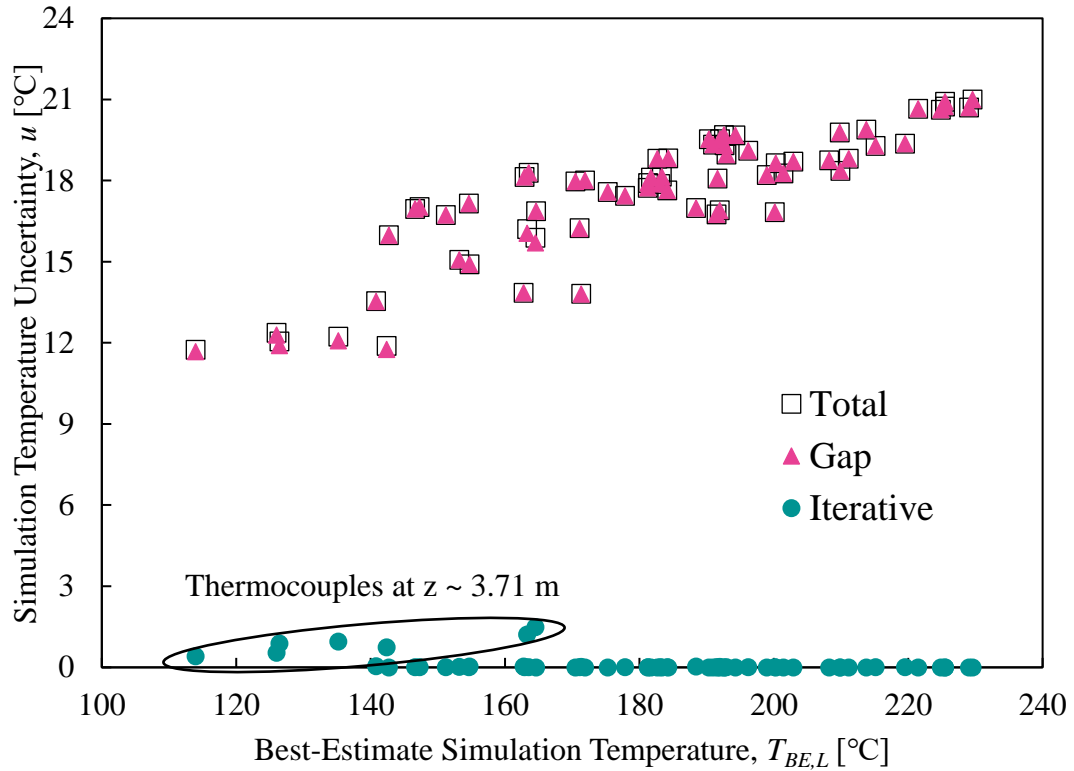


Figure 3.10. Iterative, gap, and total temperature uncertainties as a function of best estimate temperatures.

#### a. Linear Regression Analysis

Using the 40 simulation configurations as a dataset, with the nine thermal gap widths as inputs and the 63 thermocouple temperatures as outputs for each configuration, a linear regression equation for each of the thermocouple locations can be created by finding the sensitivity coefficient of each thermal gap. The linear regression equation for temperature prediction at each of the 63 thermocouple locations,  $T_{BE,L}$ , is given by

where  $T_{BE,L}$  is the temperature predicted at each thermocouple location when all thermal gaps are closed, and the product  $\sum_{i=1}^9 S_i \Delta T_i$  represents the added contribution to the

temperature by each gap at that specific location. The sensitivity coefficient,  $S_i$ , is the average temperature gradient through the gap, which is different depending on the gap and thermocouple location considered. Analysis of variance was used to determine if the sensitivity coefficients were statistically different than zero.

Figure 3.11 shows the results of the temperature predicted by linear regression models as a function of the temperature predicted by the CFD simulations at all thermocouple locations. The results of the 40 configurations used to train the linear regression models are shown as dashed lines representing two standard errors of the estimate. Three additional configurations are compared with simulations: the maximum configuration where all gaps are set to their maximum values, the nominal configuration, and the minimum configuration where all gaps are completely closed. These three configurations were not used in the training of the regression models and represent likely and bounding configurations.

The 95% standard error of the estimate for the training simulation temperatures is 1.6°C. For all the combined untrained data, the 95% standard error is 5.9°C. On average, for all the combined untrained cases, the linear regression model predicts temperatures to be 1.3°C warmer than the CFD simulations. For the nominal configuration, the linear regression model is always cooler than the CFD simulations, with an average difference of 2°C. The largest deviation for all three configurations is 11.6°C, occurring in the minimum configuration. This demonstrates that the linear regression model can be used as a tool to quickly recreate the CFD simulation results without the need to run time-

consuming simulations and for further analysis of the thermal behavior due to gap variations in the TN-32B.

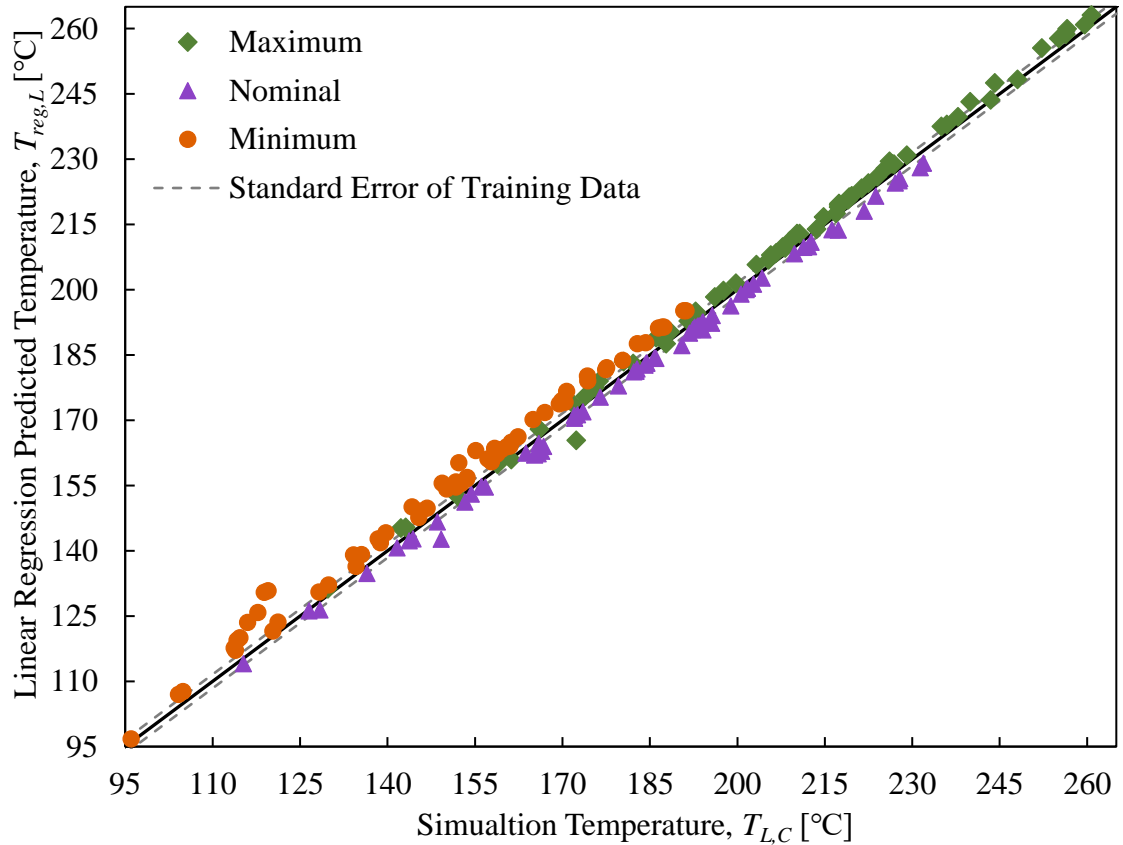


Figure 3.11. Linear regression model temperature prediction as a function of CFD simulation temperature for all gap configurations and thermocouple locations.

Using the linear regression models, contributions of each gap width on temperature prediction uncertainty can be estimated at each thermocouple location using the sensitivity coefficients. Figure 3.12 shows the contribution of temperature uncertainty,  $\sigma_{T_{reg,L}}$ , for selected gaps in selected assemblies. The Basket/Rail gap consistently has the most dominant contribution to temperature prediction uncertainty compared to all other gaps. The Basket/Rail gap contributes on average 27°C to uncertainty in temperature

prediction with a peak contribution of 31°C occurring for mid-elevation thermocouple locations (~1.83 m). This represents approximately 50% of the maximum uncertainty in predicted temperatures at all thermocouple locations. The Al/Al gaps between the aluminum basket plates are the second most significant, particularly in the innermost assemblies, with a contribution as high as 16°C. Their influence is much less significant in the peripheral assemblies. The stainless-steel to aluminum basket plate gaps (SS/Al gaps, results not shown) have similar trends to the Al/Al gaps. The Gamma/Al-Box gap has a consistent impact of approximately 5°C on temperature predictions over all locations and its impact is similar to the Al-Box/OS gap (not shown). The B-In-Liner/Gamma gap has an average contribution of 2°C but can be as high as 8°C at the lowest elevation. This base gap, like the B-Basket/In-Liner gap (not shown), is a function of elevation with its contribution decreasing with increased elevation.

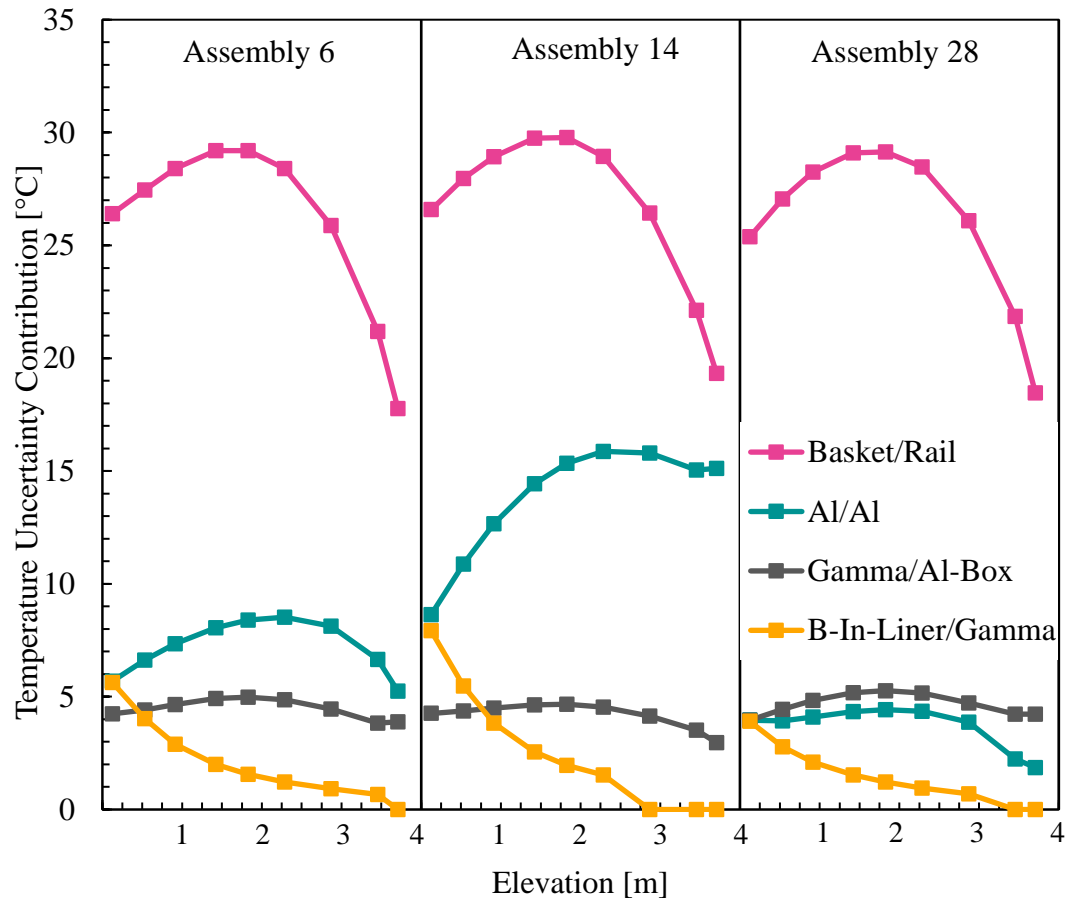


Figure 3.12. Contribution to temperature uncertainty of selected gaps at selected assemblies.

#### 4. Summary and Conclusions

In this work, a full 3D homogenous CFD model of the TN-32B cask was developed in ANSYS and simulated with Fluent code. A global UQ method was used to evaluate the effect of uncertainty of thermal gap widths in the TN-32B cask on temperature predictions. The temperature predictions at 63 locations (corresponding to experimental temperature measurement locations) from forty simulations, in which the width of nine thermal gaps are varied, were compared to experimental data obtained from the High Burnup Spent Fuel Data Project's demonstration cask.

Initial simulations that utilized a nominal gap configuration were used to determine the effects of natural convection. It was found that natural convection has a significant impact on temperatures at high and low elevations but a negligible impact on  $T_{PC}$ . Also, the inclusion of natural convection in the simulations incurred a small iterative uncertainty at the highest locations.

The UQ analysis resulted in 95%-confidence-level interval uncertainties ranging between  $\pm 12^{\circ}\text{C}$  and  $\pm 21^{\circ}\text{C}$  due to variations in the gap widths. The comparison of simulation and HBU experiment results showed that the simulations accurately predicted 51 of the 63 measured temperatures when iterative, experimental, and input uncertainties are accounted for. The disagreement between the simulation and experimental results occurred at the highest and lowest elevations. This is believed to be due to improper modeling of some of the experimental conditions in the simulations.

Using the data from the UQ analysis, a linear regression model was proposed to estimate the TN-32B model temperatures for a given set of thermal gap widths without the need for additional time-consuming CFD simulations. This model also provided information on the effect of individual gaps on predicted temperatures. It showed that uncertainty in the Basket/Rail gap width accounted for roughly 50% of the uncertainty of cask temperatures. This model is found to be extremely powerful for thermal analysis of SNF storage systems as it can assist in the design, operation, and regulation of these systems.

## **FUNDING**

This research is being performed using funding received from the US Nuclear Regulatory Commission (NRC) under contract 31310018 M0032 and by the U.S. Department of Energy (DOE) Office of Nuclear Energy University Program under award number DE-NE0008713.

## **REFERENCES**

- Adams, B.M., W.J. Bohnhoff, K.R. Dalbey, M.S. Ebeida, J.P. Eddy, M.S. Eldred, R.W. Hooper, P.D. Hough, K.T. Hu, J.D. Jakeman, M. Khalil, K.A. Maupin, J.A. Monschke, E.M. Ridgway, A.A. Rushdi, D.T. Seidl, J.A. Stephens, L.P. Swiler, and J.G. Winokur. 2022. Dakota, A Multilevel Parallel Object-Oriented Framework for Design Optimization, Parameter Estimation, Uncertainty Quantification, and Sensitivity Analysis: Version 6.16 User's Manual. *Sandia National Laboratories*.
- Akkurt, H. 2022. International Thermal Modeling Benchmark Project - Phase I Results: An Extended Storage Collaboration Program Activity. Palo Alto, CA: EPRI.
- Akkurt, H., and A. Csontos. 2020. International Thermal Modeling Benchmark Description for a High-Burnup Used Fuel Dry Storage System: An Extended Storage Collaboration Program Activity. Palo Alto, CA: EPRI.
- Areva. 2002. TN-32 Final Safety Analysis Report (FSAR), Revision 2. Virginia Electric and Power Company.
- ASME. 2009. "Standard for Verification and Validation in Computational Fluid Dynamics and Heat Transfer." *V&V 20-2009*.

- Creer, JM, TE Michener, MA McKinnon, JE Tanner, ER Gilbert, and RL Goodman. 1987. "The TN-24P PWR spent fuel storage cask: testing and analyses." *Pacific Northwest National Laboratory, Richland, WA, Report No. PNL-6054.*
- Csontos, A. 2020. High-Burnup Used Fuel Dry Storage System Thermal Modeling Benchmark: Round Robin Results. Palo Alto, CA: EPRI.
- Durbin, Samuel, and Eric R. Lindgren. 2017. Thermal-Hydraulic Results for the Boiling Water Reactor Dry Cask Simulator. ; Sandia National Lab. (SNL-NM), Albuquerque, NM (United States).
- EPRI. 2014. High Burnup Dry Storage Cask Research and Development Project – Final Test Plan. Palo Alto, California: Electric Power Research Institute.
- Fort, James A, David J Richmond, Judith M Cuta, and Sarah R Suffield. 2019. Thermal Modeling of the TN-32B Cask for the High Burnup Spent Fuel Data Project. Pacific Northwest National Lab.(PNNL), Richland, WA (United States).
- Fort, James A, David J Richmond, Ben J Jensen, and Sarah R Suffield. 2019. High-Burnup Demonstration: Thermal Modeling of TN-32B Vacuum Drying and ISFSI Transients. Pacific Northwest National Lab.(PNNL), Richland, WA (United States).
- Hall, K, and G Zigh. 2019. NUREG/CR-7260, "CFD Validation of Vertical Dry Cask Storage System". Alden Research Laboratory. Inc.
- Hanson, Brady. 2018. "High Burnup Spent Fuel Data Project & Thermal Modeling and Analysis." NWTRB Meeting, Albuquerque, NM.
- Higley, Megan. 2019. "Effect of Geometry Variation on Temperature Prediction in the TN-32 Used Nuclear Fuel Storage Cask." University of Nevada, Reno.

- Higley, Megan, Mustafa Hadj-Nacer, and Miles Greiner. 2021. "Modeling and Sensitivity Analysis of the TN-32 UNF Cask: Comparison With the HBU Project Data." ASME 2021 Pressure Vessels & Piping Conference.
- Higley, Megan, Mustafa Hadj-Nacer, and Miles Greiner. 2022. "Sensitivity Analysis and Modeling of the HBU Cask." Waste Management Symposia, Phoenix, Arizona.
- Inc., Transnuclear. NUHOMS®-24PTH DSC Thermal Evaluation for Storage and Transfer Conditions In *Project No. NUH24PTH*.
- Mittal, K, ZH Han, J Li, HC Tsai, and YY Liu. 2014. "Temperatures of Interest for the TN-32 Cask during Storage of High Burnup Fuel." INMM 55th Annual Meeting, Atlanta, Georgia, USA.
- Notz, KJ. 1988. "Characteristics of spent fuel, high-level waste, and other radioactive wastes which may require long-term isolation." Proceedings of the international topical meeting on nuclear and hazardous waste management.
- NRC, U.S. 2003. "Cladding considerations for the transportation and storage of spent fuel." *ISG-11, Rev. 3*.
- NRC, U.S. 2010. "Standard review plan for spent fuel dry storage systems at a general license facility." *NUREG-1536 Rev 1*.
- NRC, US. 2000. 10CFR Part 72—Licensing Requirements for the Independent Storage of Spent Nuclear Fuel, High-Level Radioactive Waste and Reactor-Related Greater than Class C Waste. Nuclear Regulatory Commission.
- Trujillo, Corey. 2017. "Computational Fluid Dynamics Thermal Simulations of a Nuclear Fuel Canister During Drying." University of Nevada, Reno.

Zigh, Ghani, and Sergio González. 2017. *Validation of Computational Fluid Dynamics Methods Using Prototypic Light Water Reactor Spent Fuel Assembly Thermal-Hydraulic Data*: United States Nuclear Regulatory Commission, Office of Nuclear Regulatory ....

# Chapter 4: Detailed and Homogenous Modeling of the TN-32B Spent Nuclear Fuel Demo Cask

---

## ABSTRACT

Due to the complexity of modeling spent nuclear fuel casks and canisters, the homogenous method (i.e., modeling the fuel regions as porous blocks with effective properties) is often utilized to conduct computational fluid dynamics simulations. This method allows for reducing the computational effort required by the detailed modeling method. However, no comprehensive comparison between the homogenous and detailed methods in a full cask has been reported in the literature. Moreover, recent modeling efforts of the TN-32B cask, employed in the High Burnup Demonstration project, showed significant discrepancies from the measured temperature data. These discrepancies were attributed to uncertainties in gap sizes. Many of the models employed the homogenous method, and the error arising from the homogenous assumption was not quantified.

In this Part I paper, a detailed model of the TN-32B spent nuclear fuel cask with a detailed representation of the fuel assemblies is compared to a model that uses the homogenous method under storage conditions. The same input parameters and computational mesh are used in both models. Effective thermal conductivities and porous flow coefficients in the radial and axial directions are developed and applied to the homogenous model. Temperature and axial velocities obtained from the detailed and homogenous models are compared on a point-to-point basis within the fuel regions. The

results indicate that the homogenous model accurately predicts temperatures relative to the detailed model, with the most notable differences observed at lower elevations within the fuel regions. 95% of fuel region temperature data are within 2°C between the models. Furthermore, temperatures at 63 locations obtained from both models are compared to data from the High Burnup Demonstration project and the results showed a difference ranging from -7°C to +10°C.

**Key Words:** *Detailed Fuel Assembly, Homogenous Fuel Assembly, TN-32B, CFD.*

## NOMENCLATURE

$C$	Inertial resistance factor [ $\text{m}^{-1}$ ]
$h$	Convective heat transfer coefficient [ $\text{W m}^{-2} \text{K}^{-1}$ ]
$k$	Thermal conductivity [ $\text{W m}^{-1} \text{K}^{-1}$ ]
$K$	Permeability [ $\text{m}^2$ ]
$L$	Characteristic length [m]
	Mass flow rate [ $\text{kg s}^{-1}$ ]
$P$	Pressure [Pa]
$Q$	Heat generation rate [W]
$r$	Radial location [m]
$S$	Standard error [°C]
$T$	Temperature [°C]
$V$	Axial velocity [m/s]
$x$	$x$ -coordinate [m]

$w$	Width [mm]
$y$	y-coordinate [m]
$z$	Elevation [m]

### ***Greek***

	Inertial coefficient [ $\text{kg m}^{-4}$ ]
	Viscous Coefficient [ $\text{kg m}^3 \text{s}^{-1}$ ]
	Difference
	Dynamic viscosity [ $\text{kg m}^{-1} \text{s}^{-1}$ ]
	Density [ $\text{kg m}^{-3}$ ]

### ***Subscripts***

95	95%
$a$	Axial
$D$	Detailed
$eff$	Effective
$exp$	Experimental
$H$	Homogenous
$in$	Inlet
$NC$	Natural convection
$PC$	Peak Cladding
$r$	Radial
$S$	Stagnant
$w$	Wall

***Abbreviation***

3D	Three-dimensional
CFD	Computational Fluid Dynamics
DSC	Dry storage canisters/casks
ESCP	Extended Storage Collaboration Program
FSAR	Final Safety Analysis Report
HBU	High burnup
PNNL	Pacific Northwest National Laboratory
SNF	Spent nuclear fuel
UQ	Uncertainty Quantification

**1. Introduction**

Spent nuclear fuel (SNF) in the United States is initially stored in water pools and then transferred to dry storage canisters/casks (DSCs). DSC designs are evaluated, licensed, and certified, in part, based on their ability to maintain SNF and other component temperatures within specified limits during all storage operations, including loading, draining, drying, pressurization, and long-term storage (NRC 2003).

Computational Fluid Dynamics (CFD) simulations are commonly employed to predict DSC temperatures and demonstrate regulatory compliance under storage operations for DSC designs (Areva 2002). However, conservative and simplified modeling techniques are often employed to reduce the computational effort required to simulate detailed full-scale DSCs and build safety margins for regulatory compliance (Areva 2002). These conservative modeling techniques have led to significant overpredictions in DSC temperatures compared to the limited available experimental data

in Full DSCs. This overprediction is expected to be more significant in new advanced DSCs designed for higher heat generations and burnups but by unknown margins (Csontos 2020).

The most commonly used conservative technique is the homogenous modeling of the fuel assemblies that was introduced by Bahney et al. (Bahney and Lotz 1996) and later extended by Zigh & Solis (Das et al. 2010). Bahney et al. (Bahney and Lotz 1996) proposed to model the fuel regions (assemblies) as solid heat-generating blocks (instead of distinct fuel rods) with effective radial and axial thermal conductivities. Zigh & Solis (Das et al. 2010) included flow through the fuel regions by modeling those regions as porous blocks with effective flow properties. This technique has been widely accepted for modeling storage conditions in DSCs due to its simplicity and computational efficiency (Fort et al. 2016; Higley, Greiner, and Hadj-Nacer 2024; Akkurt and Csontos 2020; Fort, Richmond, Cuta, et al. 2019). Computational efficiency is significantly improved through the reduction in computational mesh and fluid-solid interfaces leading to far fewer radiation and fluid flow calculations. Effective thermal and flow properties for the homogenous fuel regions are developed from detailed sub-models of the fuel assemblies. These properties are specific to the conditions they were developed for, including pressure, gas fill, and fuel assembly geometry and properties.

Brewster et al. (Brewster et al. 2012) investigated the effects of homogenous modeling of the fuel regions, including spacers and nozzles, by homogeneously modeling the TN-24 fuel assemblies and replacing the hottest assembly with a highly detailed assembly. While small differences in temperature predictions were observed, significant differences in flow patterns in the nozzle region were observed (Brewster et al. 2012).

Hernandez-Avellaneda et al. investigated the impact of assembly nozzles on temperature predictions in the ESTII-32P cask and found them to be largely negligible (Hernandez-Avellaneda et al. 2023). Researchers from the Pacific Northwest National Laboratory (PNNL) have employed thermal-hydraulic (using COBRA-SFS), homogenous, and/or detailed modeling techniques to investigate the thermal behavior of several DSC designs (TN-32B, MAGNASTOR with a TSC-37 canister, and NUHOMS AHSM with a 32PTH2 canister) (Fort et al. 2016; Fort, Richmond, Jensen, et al. 2019; Suffield et al. 2012). Their findings generally indicated that the homogenous modeling technique is more conservative than the detailed technique (Fort, Richmond, Jensen, et al. 2019). Yoo et al. (Yoo et al. 2010) used thermal-hydraulic and detailed techniques to model the TN-24 and compared the results to experimental data. Overall, a good agreement between the detailed model and experimental data was observed. However, deviations in velocity predictions between the detailed and thermal-hydraulic models were observed. In the above works, direct comparisons between homogenous modeling and the detailed modeling techniques were limited and did not provide a full picture of the effect of the homogenous assumption.

Experimental data on the thermal performance of DSCs has been gathered for older cask designs and low burnup SNF such as the VSC-17 ventilated cask (McKinnon et al. 1992), MC-10 cask (McKinnon et al. 1987), Castor-V/21 (Dziadosz et al. 1986), TN-24P cask (Creer et al. 1987), and the HI-STORM 100 (Cuta and Adkins 2014), as well as non-radioactive experiments like the Dry Cask Simulator (Durbin and Lindgren 2017). With the increase in fuel burnups, the need for a confirmatory dry storage demonstration with high burnup SNF became clear. The high burnup (HBU) demonstration cask has been

conducted to strengthen the technical justification for the extended storage of high burnup SNF in DSCs (EPRI 2014). In this experimental demonstration, a TN-32B SNF cask was instrumented with 63 fuel region thermocouples and loaded with 30.4 kW of high burnup SNF assemblies. After initial loading and drying, a two-week thermal soak operation was conducted to provide data for comparison with thermal models.

In a blind benchmark, four submissions of best-estimate thermal modeling of the TN-32B were compared with experimental data from the thermal soak. Overall, these models overpredicted temperatures by typically 20 to 50°C, but as high as 95°C (Csontos 2020). The overprediction was largely attributed to the overestimation of gap sizes and assembly heat generation rates. Hall and Zigh (Hall and Zigh 2019) conducted a local CFD uncertainty quantification (UQ) of many of the parameters affecting the thermal behavior of the TN-32B cask used in the HBU experiment. They used the homogenous fuel region assumption to model the full cask. They found that gap sizes accounted for 63°C in temperature uncertainty out of a total of 73°C. Using a global uncertainty quantification method and a similar full homogenous model of the TN-32B, the current authors estimated that the thermal gaps account for a maximum of  $\pm 21^\circ\text{C}$  in temperature uncertainty (Higley, Greiner, and Hadj-Nacer 2024). They also showed that the homogenous model accurately predicted 51 out of the 63 measured temperatures. PNNL created a detailed and a homogenous model of the TN-32B, however, it was not used in storage simulations or directly compared with a homogenous form of the same model (Fort, Richmond, Jensen, et al. 2019). This leaves uncertainty in the ability of the homogenous model, relative to a detailed model, to predict cladding temperatures

throughout the fuel region of a DSC filled with high burnup pressurized water reactor assemblies during storage conditions.

In this Part I paper, detailed and homogenous three-dimensional (3D), full-length, one-eighth CFD models of the TN-32B demonstration cask are constructed and simulations are carried out in ANSYS/FLUENT under storage (thermal soak) conditions. The same highly structured mesh is used in both the detailed and homogenous models to eliminate the effect of mesh-induced discrepancy on the results and to conduct a direct comparison between the modeling techniques on a mesh-element basis. The temperature results are compared with experimental data from the HBU demonstration cask at the 63 measured locations. All fuel region temperatures and flow velocities are monitored and compared between the two models for comprehensive effects of homogenous modeling under storage conditions. In Part II paper, a comparison between the detailed and homogenous modeling techniques will be conducted for vacuum drying conditions.

## **2. Computational Model**

Figure 4.1 shows a color-coded computational domain of the TN-32B developed in the ANSYS package for both the detailed and homogenous models. It represents a one-eighth cross-section of a full 3D TN-32B cask with symmetry boundary conditions. The one-eighth symmetry assumption was used to reduce the computational effort, especially for the detailed model. The domain was constructed based on dimensions and material properties obtained from the Extended Storage Collaboration Program (ESCP) International Thermal Modeling Benchmark Project (Akkurt and Csontos 2020) and the TN-32B Final Safety Analysis Report (FSAR) (Areva 2002). For more details on the

model dimensions and materials, please refer to the author's previous paper, Ref (Higley, Greiner, and Hadj-Nacer 2024).

The model domain in Fig. 4.1 consists of five fuel assemblies (three full and two half) within stainless steel cells surrounded by aluminum plates, representing the fuel basket. The fuel assemblies are represented as porous heat-generating blocks in the homogenous model or arrays of  $17 \times 17$  fuel rods (including pellets and cladding) in the detailed model. The Boron plates within the fuel basket are not modeled distinctly from the aluminum plates as they have similar thermal properties. The basket is centered within a carbon steel inner liner serving as the inner confinement barrier. Aluminum support rails are placed between the basket and the inner liner. A thick gamma shield envelops the inner liner, which is surrounded by aluminum boxes filled with a polyester neutron shield. An outer stainless steel shell surrounds the main cask body, and a lid is bolted to the top of the cask.

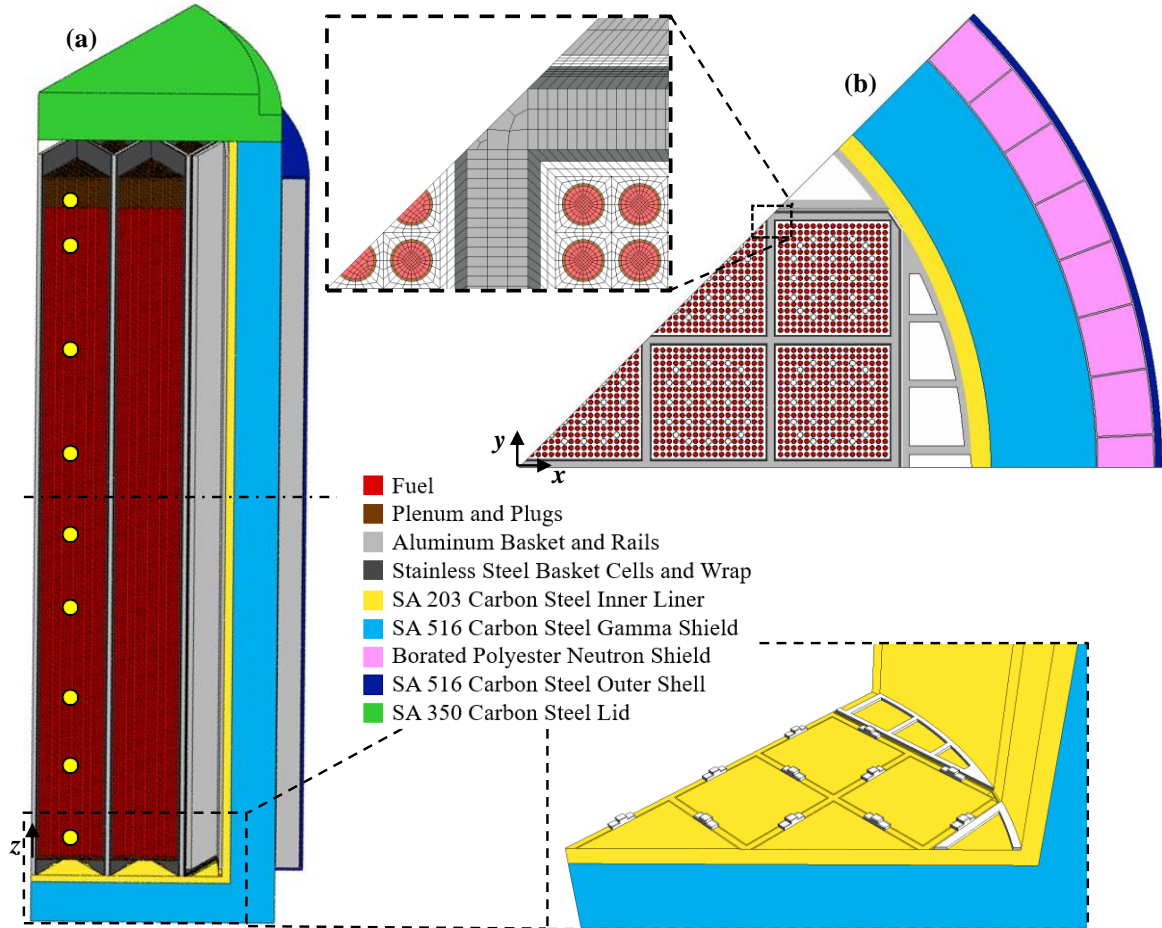


Figure 4.1. Color-coded computational domain of the TN-32B detailed model. (a) Isometric view of the 3D model with a detailed region of drain holes, and (b) a horizontal cross-section with a detailed region showing the mesh. Indicators of the axial position of the thermocouples in the instrumented assemblies are shown in (a).

As previously mentioned, the current authors conducted a global UQ analysis to determine the effect of variation in the size of nine gaps located between the TN-32B cask components on temperature prediction (Higley, Greiner, and Hadj-Nacer 2024). They showed that average values of the cask gap widths (half the FSAR values (Areva 2002)) can be used as reasonable approximations of their widths for comparison with the HBU demonstration cask experiment results. These values are used in the current work

except for the basket-rail gap (between the aluminum basket and support rails), where a gap of 2.54 mm is used as a reasonable estimation (Higley, Greiner, and Hadj-Nacer 2024)(Fort, Richmond, Jensen, et al. 2019).

The detailed region in Fig. 4.1a shows the drain holes at the base of the basket, which are important to accurately model natural convection within the cask. These holes are represented as rectangles (instead of triangles in the actual TN-32B model) for meshing purposes while maintaining the same flow area. The drain holes in the supporting rails, whose dimensions and locations are unknown (proprietary), are modeled by retracting the rails to half the height of the basket drain holes (6.5 mm). The retracted space is modeled as helium, however, with a thermal conductivity of aluminum. This allows helium to circulate underneath the supporting rail while maintaining the axial conduction through the rails. Likely, this method of modeling the drain holes in the support rails would slightly overestimate the flow circulation within the supporting rails and underestimate it from the rails to the fuel assemblies as the supporting rail drain holes are likely larger. However, it is not expected to affect the cask temperatures significantly.

The same highly structured mesh is used in the homogenous and detailed models, which allows for element-by-element comparison between the models. The mesh consists of 40.8 million elements with a minimum orthogonality of 0.15 and a maximum skewness of 0.85. The fuel assembly regions account for 27.8 million elements, with 10.5 million of those being for the helium surrounding the rods. This mesh was constructed based on previous research by the authors in two-dimensional meshes of the TN-32B (Higley 2019) and 3D meshes of the TN-24 (Trujillo 2017), as well as mesh sensitivity

results from Hall *et al.* modeling of the TN-32B (Hall and Zigh 2019) and Yoo *et al.* modeling of detailed assemblies in the TN-24P (Yoo *et al.* 2010). It is inferred that a mesh sensitivity analysis for the TN-32B model used in the current work is not required and is resolved enough that the results are insensitive to further refinement.

### 3. Simulation Conditions

Similar simulation and boundary conditions to those used in the previous paper (Higley, Greiner, and Hadj-Nacer 2024) were employed in the current work, and are considered to be representative of the demonstration cask thermal soak operation (Csontos 2020). In summary, steady-state simulations that account for conduction, natural convection, and radiation heat transfers are conducted. The cask is filled with helium gas at a pressure of 223 kPa and is oriented vertically, with gravity acting in the negative  $z$ -direction (see Fig. 4.1a). The effect of natural convection was explored by enabling and disabling it. A laminar helium flow within the cask is assumed due to low Reynolds number ( $\approx 1300$ ) and low Rayleigh number ( $\sim 4.2 \times 10^8$  for an assumed characteristic length of the fuel rod) which is consistent with flow found in bolted cask designs. For the homogenous model, effective thermal and flow properties are developed (see next section). Emissivities of 0.2, 0.3, 0.45, and 0.8 are used for aluminum, stainless steel, carbon steel, and zircaloy cladding, respectively. Temperature-dependent material properties obtained from the ESCP project are used. A constant ambient temperature around the cask of 24°C is employed. The cask dissipates heat to the surroundings via convection and radiation, with an outer wall emissivity of 0.9. Temperature-dependent convective heat transfer coefficients of  $h_{\text{up}}$  for upward-facing surfaces,

– for downward-facing surfaces, and – for vertical surfaces are employed on the outer surface of the cask (Holman 1997).

Figure 4.2a shows a map of the heat generation of the fuel assemblies used in the TN-32B HBU demonstration cask experiment, which totals 30.46 kW. Since the model developed in this work is one-eighth of the full model cross-section, averaging schemes that are representative of the full heat loading must be developed. Because the HBU demonstration cask heat loading does not have one-eighth symmetry, several averaging schemes were considered. 1) A uniform loading using the average of all assemblies' heat generations. This scheme drastically underestimates the heat loading of the innermost fuel assemblies and leads to an underestimation of the temperatures in these assemblies. 2) A positioned average loading where the heat generations of the assemblies at the same distance from the radial center of the cask are averaged. This scheme results in a greater underestimation of the innermost assemblies' heat generations than the uniform loading and leads to even lower temperatures. 3) An assembly of interest averaging scheme, where the heat generation of the instrumented assemblies containing thermocouples (highlighted in Fig. 4.2a) are averaged and the average values are applied to the corresponding assemblies in the one-eighth model (see Fig. 4.2b). For example, the heat generations of assemblies 14 and 19 (see Fig. 4.2a) were averaged and applied to the innermost assembly A in the one-eighth model (see Fig. 4.2a), and the heat generation of assemblies 6 and 24 were averaged and applied to assembly D in the one-eighth model. Assembly B in the one-eighth model does not correspond to any instrumented assembly. Therefore, its heat generation was calculated so that the total heat generation (when symmetry is accounted for) is consistent with that of the HBU demonstration cask. This

scheme was adopted in the current work as it showed that it gives similar temperature results to the full-loading model.

Figure 4.2c illustrates the axial heat generation profile applied to both homogenous and detailed models. The solid line represents the actual profile, while the polynomial function, depicted by a dashed line approximates this profile and is used in the simulations. The heat generated by the fuel assemblies is applied in the simulations as a volumetric heat generation. For the homogeneous model, it is applied to the entire volume of the fuel regions, and in the detailed model, it is applied to the uranium dioxide pellets.

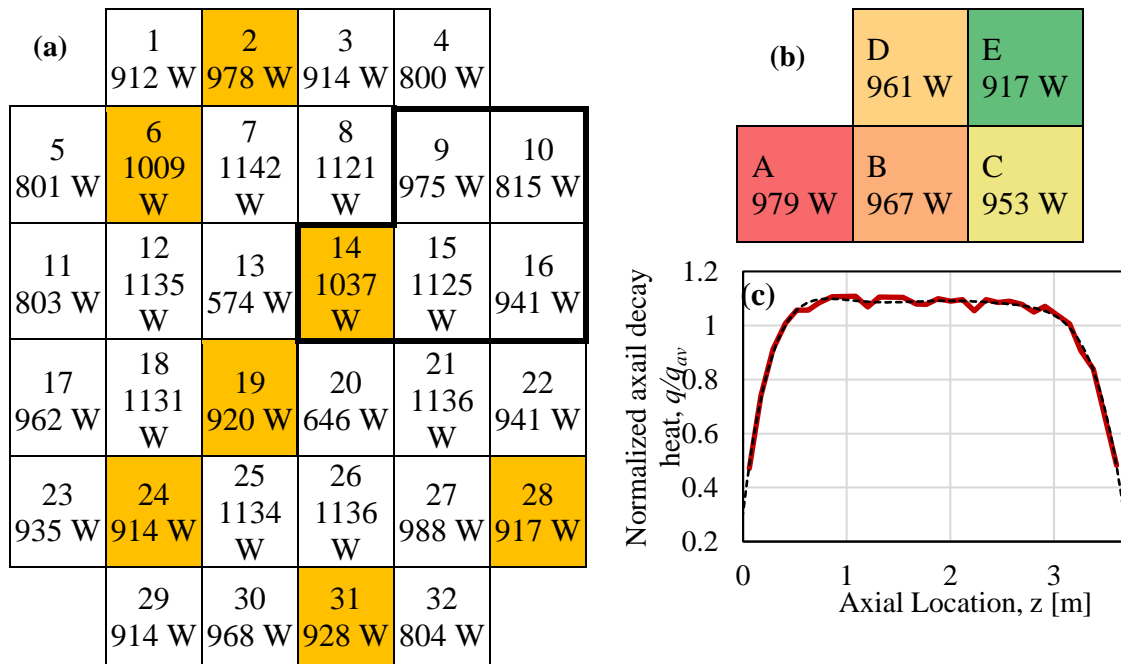


Figure 4.2. Heat generation rates and labeling scheme for (a) the HBU demonstration cask loading, (b) symmetric one-eight loading used to approximate the HBU loading, and (c) normalized axial heat generation profile. The instrumented assemblies are highlighted in (a).

### a. Homogenous Model Properties

For the homogenous model, radial and axial effective thermal conductivities and porous flow coefficients for the fuel regions are developed. These properties are derived from detailed sub-models of a single assembly. The effective radial thermal conductivity, which is used for both radial conduction and radiation heat transfers in the homogenous assembly, is derived from a detailed two-dimensional cross-sectional CFD model of a 17×17 fuel assembly. Simulations using this model were carried out for several heat generations,  $\beta$ , and boundary wall temperatures,  $T_{cl}$ , while monitoring the peak cladding temperature,  $T_{cl,peak}$ . The effective radial thermal conductivity,  $k_{eff,r}$ , is then calculated as

$$k_{eff,r} = \frac{Q_{rad}}{A_{cl} \Delta T_{cl}} \quad (4.3)$$

where  $L_{act}$  is the active length of the fuel (~3.66 m). Figure 4.3a shows the effective radial thermal conductivity plotted as a function of  $T_{cl}$ . The dashed line is the polynomial fit function used in the simulations. The effective radial thermal conductivity derived in this work is very similar to the one reported in the TN-32B FSAR (Areva 2002).

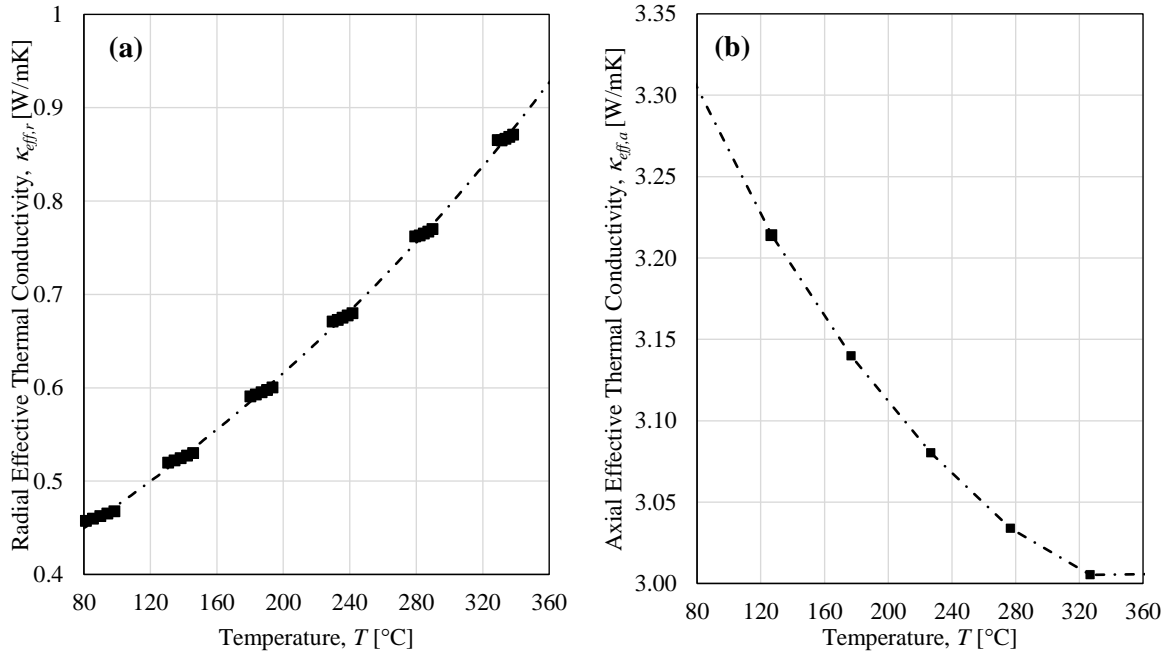


Figure 4.3. (a) Radial effective thermal conductivity and (b) axial effective thermal conductivity of the homogenous fuel regions.

Figure 4.3b shows the effective axial thermal conductivity of the fuel assembly as a function of temperature. It is analytically calculated using a parallel thermal circuit, based on the cross-sectional area-weighted average of the thermal conductivities of helium, cladding, and fuel pellets. The effective axial thermal conductivity in Fig. 4.3b is higher than the values reported in the literature (Fort et al. 2016; Akkurt and Csontos 2020). This is because the thermal conductivity of the fuel pellets is usually not accounted for in the literature to introduce conservatism. However, it is expected that this will have a minor effect on temperatures as the axial heat conduction is relatively insignificant compared to the radial heat transfer.

Effective porous flow coefficients allow modeling of buoyancy-induced natural convection and fluid flow through the fuel assemblies in the homogenous model. The effective porous flow coefficients are derived using a 3D CFD model of a  $17 \times 17$  fuel

assembly. Boundary mesh layers were used on fuel rod surfaces to better capture the effect of the velocity boundary layer. Helium is assumed to flow axially along the length of the fuel assembly with the inlet being at the bottom and the outlet at the top of the assembly. Flow simulations were carried out for several inlet velocities and a constant outlet gauge pressure. The axial and radial pressure drop per length,  $\Delta p/L$ , across the fuel assembly is plotted as a function of the inlet velocity,  $v$ , and fitted to an equation of the form,

$$\Delta p/L = a v^2 + b v$$

where  $a$  is the inertial coefficient and  $b$  is the viscous coefficient. These coefficients are provided in Table 4.1 for both radial ( $x, y$ ) and axial ( $z$ ) directions.

Table 4.1: Porous flow coefficients of the homogenous fuel region.

Direction	[kg/m <sup>4</sup> ]	[kg/m <sup>3</sup> -s]
x, y	0.81	9.0E-04
z	0.11	10.7

For implementation as isotropic porous media characteristics in the simulations, the inertial resistance factor,  $\beta$  [1/m] and the viscous resistance (inverse of absolute permeability),  $\alpha$  [1/m<sup>2</sup>] are calculated as

$$\beta = \frac{a}{\rho} \quad \alpha = \frac{b}{\mu}$$

where  $\rho$  is the fluid density and  $\mu$  is the fluid viscosity. The axial viscous and inertial coefficients obtained in this work are in the same order of magnitude as the literature values. However, the radial coefficients are an order of magnitude different from the values found in the literature (Brewster et al. 2012; Fort et al. 2016). It should be noted

that radial flows within the assemblies are relatively insignificant because of the vertical orientation of the cask.

#### **4. Results**

The results are divided into two sections. The first section presents a comparison between the results obtained from the detailed model and the measured temperature data from the HBU demonstration cask, including a discussion of the effect of modeling natural convection. The second section provides a comparison between the homogenous and detailed models and discusses the strengths and limitations of the homogenous assumption.

##### **a. Detailed Model Results and Comparison with Experimental Data**

Figure 4.4 shows the temperature profiles obtained from the detailed model along the seven instrumented assemblies (see Fig. 4.2a), compared to the experimentally measured temperatures obtained from the HBU demonstration project. Due to the model's symmetry, temperature profiles for assemblies 2 and 31 are in the same position, while the profiles for assemblies 6 and 24, and assemblies 14 and 19 are in different positions within each symmetry assembly. Both the experimental data and simulation profiles display a parabolic shape characteristic of SNF cask systems. The innermost assemblies (#14 and #19) exhibit the highest temperatures and the temperature decreases as the radial distance from the center increases, with the outermost assembly (#28) having the lowest temperatures. The axial location of the peak temperature in each assembly is consistent between the measured and simulated temperatures, occurring at ~2.28 m from the bottom of the assemblies. Below the elevation of ~ 3 m, the detailed model slightly

overpredicts the measured data in most assemblies, except assembly 31, where the opposite behavior is observed. This may be due to the heat generation used for the symmetry assembly C (see Fig. 4.2b) being lower than the actual value of assembly 31 (See Fig. 4.2a). Above the elevation of 3.66 m, the parabolic trend of temperature is disrupted due to the mixing of helium flows in the open space above the fuel assemblies.

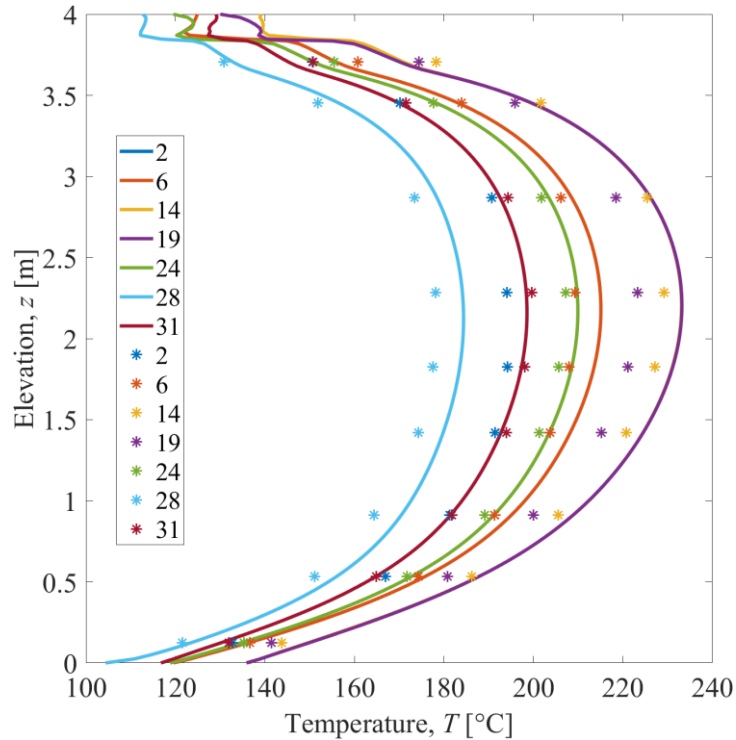


Figure 4.4. Detailed model predicted temperature profiles compared with experimentally measured temperatures along the instrumented assemblies.

Figure 4.5a shows the experimental temperature residuals for the detailed model, defined as the difference between the temperatures predicted by the detailed model and the experimental data at each thermocouple location, plotted as a function of elevation. The residuals are within a narrow range of  $-7^{\circ}\text{C}$  to  $10^{\circ}\text{C}$ , with assembly 19 having the highest residuals. This may be, in part, due to the heat generation value used in the symmetry model at assembly A (see Fig. 4.2b), which is 59W higher than the actual

value of assembly 19 (see Fig. 4.2a). However, this does not explain the overprediction at assemblies 6 and 14 for which the heat generations of their symmetry assemblies (i.e., D and A, respectively) are lower than their actual values. Additionally, Fig. 4.5a shows that at the highest elevation, the detailed model underpredicts the measured temperatures in all assemblies, except assembly 28. This underprediction may be caused by an overestimation of the upward flow mixing above the assemblies due to the absence of the nozzles, which increases the heat transfer at those locations and reduces temperatures. In assembly 28, however, a significant downward flow occurs, which brings hot helium from other central assemblies, causing the temperature to rise.

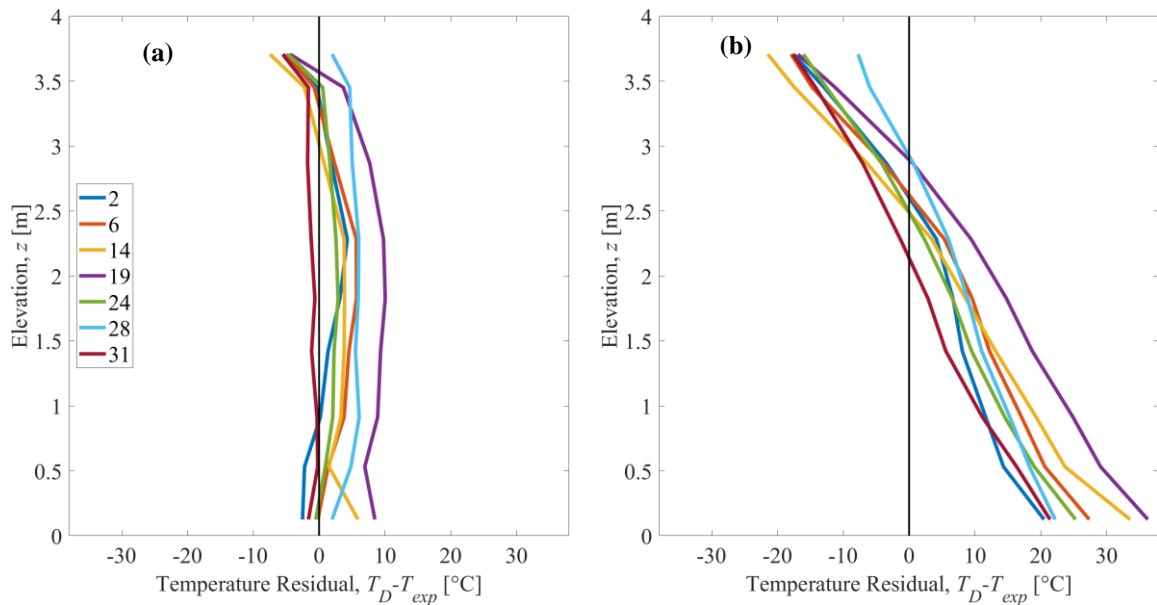


Figure 4.5. Temperature residual from the experimental data for the (a) detailed model with natural convection, and (b) detailed model without natural convection.

The small magnitude of the residuals and the absence of an apparent systematic error suggest that the detailed model can accurately capture the thermal behavior of the TN-32B cask even when employing a one-eighth symmetry model. Even though this is not a

full validation of the detailed model, it gives confidence in the use of this model to verify the homogenous modeling technique. It is important to emphasize that the choice of the heat generation averaging scheme is critical. In this work, the use of an assembly-of-interest averaging scheme is reasonable because of the availability of experimental data. If another scheme is used, it would result in different thermal behavior and may not capture the actual data as closely.

The significance of modeling the effect of natural convection on the temperature profiles along the seven instrumented assemblies is investigated by disabling the buoyancy effect in the detailed model and comparing the results to the case with natural convection enabled. In a previous study (Higley, Greiner, and Hadj-Nacer 2024), the authors examined the effect of natural convection on the temperature profiles using a homogenous model that did not account for the drain holes in the support rails. The results showed a moderate effect of natural convection. However, following a discussion with the TN-32B manufacturer, the authors were informed of the presence of drain holes at the bottom of the support rails, but no dimensions were provided. Therefore, as was explained in the introduction, the drain holes were modeled by retracting the support rail 6.5 mm from the bottom cavity.

Figure 4.6 shows the net mass flow rate induced by natural convection in each of the five symmetry assemblies (A to E) and the two support rails on the periphery of the basket, labeled corner and side rails, plotted as a function of the radial distance from the axis for the detailed model (displayed as a solid line). The mass flow rates of the half assemblies (A and D) are doubled to match the flow area of the full assemblies for comparison. The net mass flow rates in the assembly regions are positive, which indicates

a predominantly upward helium flow. However, they are negative in the support rails, which indicates a predominantly downward flow. The innermost assembly (A) exhibits the largest flow rate, whereas the outermost assembly (E) has the lowest flow rate. This behavior is expected as natural convection intensifies with the increase in temperature. The side rail has a significantly greater mass flow rate than the corner rail due to a larger available flow area through the rails and drain holes. The sum of all net flow rates, including the flow through the basket/rail gap (not shown in Fig. 4.6), equals zero, indicating mass conservation.

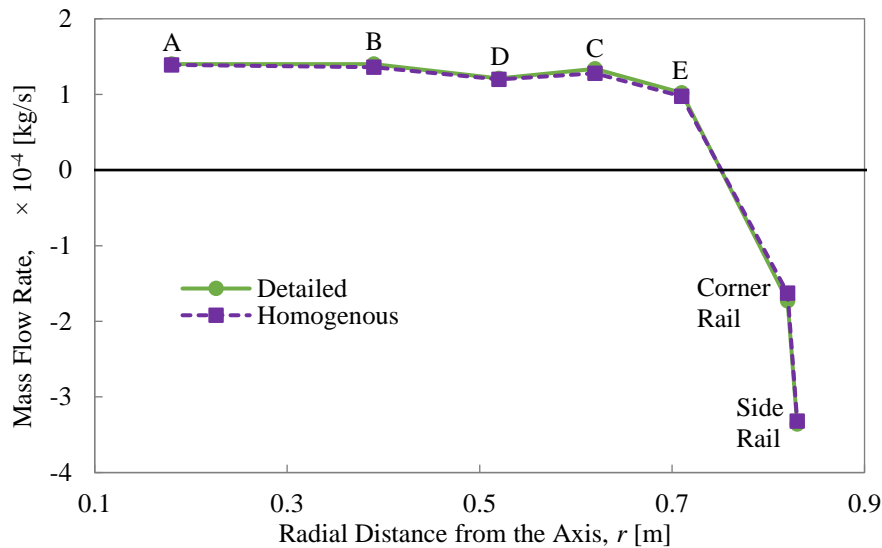


Figure 4.6. Assembly and supporting rail mass flow rates versus radial distance for the detailed and homogenous models.

Figure 4.7a shows the axial velocity contour along the plane passing through the axial center of the fuel assemblies for the detailed model. Velocities in the support rails are not shown to accentuate the profiles within the assembly regions. The velocity at the solid components of the assemblies (fuel pellets and claddings) is zero. Relatively high positive velocities are obtained at the center of the assemblies, between the fuel rods and

within the hollow guide tubes. In assemblies A and B, the velocities are positive (upward flow), while they are mostly positive in assemblies C, D, and E, with some negative (downward) flow at the surfaces and corners near the rails. Assembly E, which is farthest from the axis, has the most significant downward flow occurring at the two surfaces adjacent to the rails, due to the lower temperatures at those locations. The flows within the support rails (not shown) are mostly downward, with positive upward flows near the surfaces adjacent to the fuel assemblies. Figures 4.6 and 4.7a indicate consistent natural convection flows within the fuel assemblies and support rails. The impact of these flows on temperatures is discussed in subsequent paragraphs.

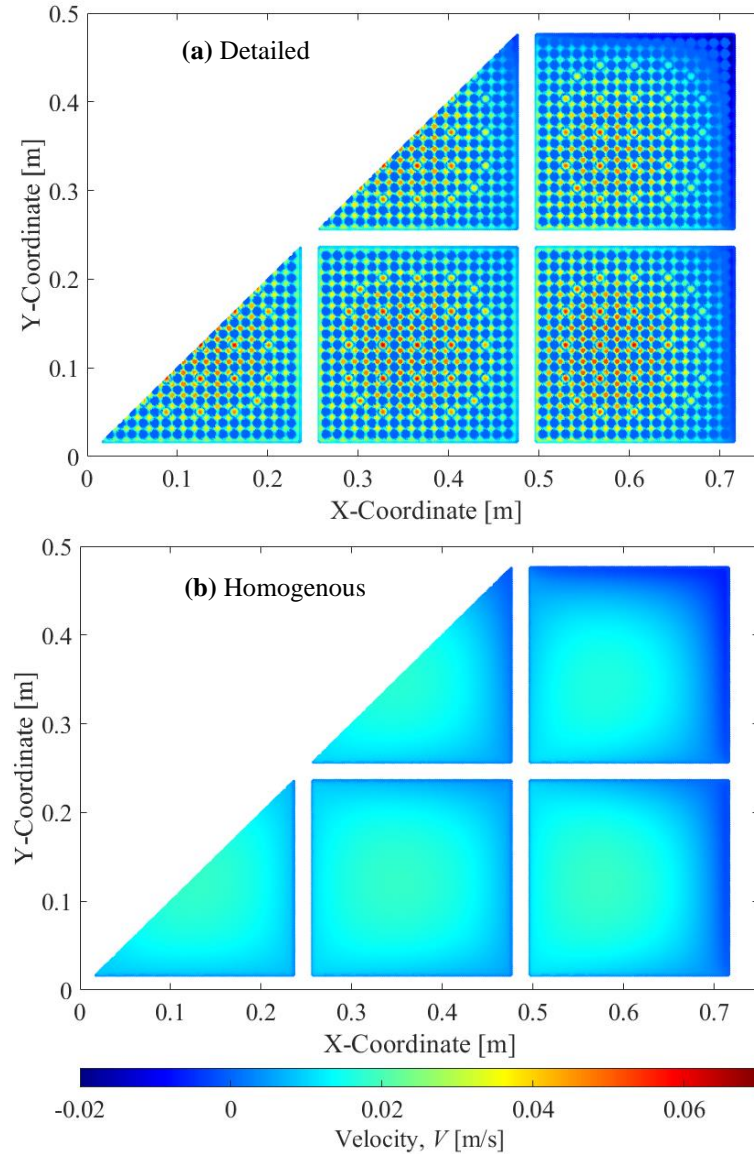


Figure 4.7. Mid-plane ( $z = 2.134$  m) axial velocity profiles for (a) the detailed and (b) the homogenous models.

Figure 4.5b shows the residuals from the detailed model when natural convection is disabled in the simulations. A significant sloping behavior in the residual profiles is observed in all assemblies, resulting in a wider residual range of  $-15^{\circ}\text{C}$  to  $+30^{\circ}\text{C}$ . The detailed model systematically underpredicted the measured temperatures at elevations above  $\sim 2.5$  m and overpredicted them at elevations below it. This result demonstrates that

natural convection has a significant effect on temperature profiles even in storage systems that do not rely much on convective heat transfer, like the TN-32B. While some studies (Hall and Zigh 2019)(Fort, Richmond, Cuta, et al. 2019) suggested that natural convection has a minor effect on cask temperatures, these works usually considered only that effect on the peak cladding temperature. Figure 4.5b shows that the effect of natural convection on peak cladding temperature is indeed small. However, when considering other axial and radial locations, the natural convection effect becomes significant.

The comparison presented in Fig. 4.5b on the effect of natural convection is limited to the 63 measured locations. To conduct a more comprehensive study of this effect on temperatures, a point-to-point comparison between temperatures obtained from the detailed model with natural convection enabled and disabled is presented in Fig. 4.6. This figure includes 5 million temperature data points extracted from 27 cross-sectional planes within the fuel regions. This includes 24 planes through the active fuel region, spaced 6 inches apart, as well as planes through the center of the top and bottom plugs and the plenum region. This data set represents approximately one-fifth of the total data in the fuel regions. The temperature data in Fig. 4.6 is colored by elevation (axial location) and the solid diagonal line represents the equality line.

The results in Fig. 4.8 confirm those discussed in Fig. 4.5b where the natural convection model systematically overpredicts temperatures at elevations above  $\sim 2.5$  m and underpredicts them below that point. The data in Fig. 4.8 seem to be arranged in lines, with each line corresponding to one of the 27 cross-sectional planes. These lines are nearly linear for all planes, except for the lower planes below 0.5 m elevation and the highest plane through the top plug. At these particular planes, there is no consistent

relationship between the temperature data obtained from the models with and without natural convection. This is because the helium flows at the lowest elevations are not yet fully developed, and at the highest elevation, the mixing of the flows above the fuel regions causes inconsistency. However, in the middle fuel regions, as the flows develop, a linear relationship between the predicted temperatures emerges, with slopes slightly varying as a function of elevation.

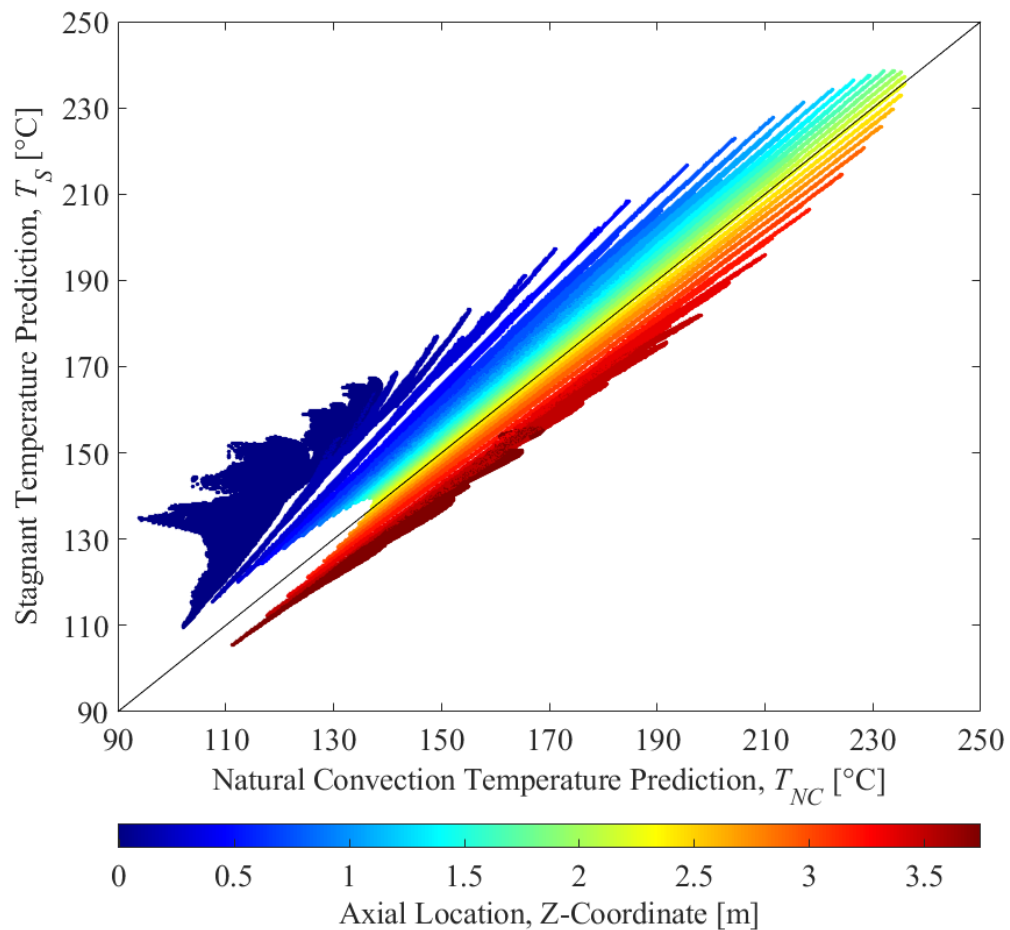


Figure 4.8. Point-to-point comparison of temperature predicted by the detailed model without natural convection versus temperature predicted by the detailed model with natural convection.

### **b. Comparison of Homogenous and Detailed Model Results**

Figure 4.6 shows the mass flow rates in the assemblies and supporting rails predicted by the homogenous model and compared to the detailed model. Nearly the same mass flow rates are predicted by both the detailed and homogenous models in all assemblies and rails, with the largest differences of ~5% observed in assemblies C and E, and in the corner rail. The close agreement in predicted mass flow rates is likely due to the porous flow coefficients calculated for the homogenous model being based on replicating the average pressure drop along the assemblies, and due to also the close attention given to the boundary layers.

Figure 4.7b shows the axial velocity contour through the mid-plane of the fuel assemblies for the homogenous model. The global behavior is similar to that obtained with the detailed model (see Fig. 4.7a), i.e., the highest velocities are obtained within the center of the fuel assemblies, with assemblies A and B having positive velocities and assemblies C, D, and E having predominantly positive velocities with negative values at the locations closer to the rails. Because of the absence of solid components (fuel pellets and claddings) in the homogenous model, the effective flow area is larger than in the detailed model. Consequently, with the mass flow rates through the assemblies being similar between the two models, the velocities in the homogenous model are lower than those in the detailed model.

Figure 4.9 shows the contours of the temperature difference between the detailed and homogenous models within the fuel assembly regions at three cross-sectional planes through the bottom plug, the middle of the active fuel region, and the top plug. At the lowest elevation (Fig. 4.9a), there is a random difference between the temperatures for

the detailed and homogenous models. This randomness is caused by the flow patterns at the bottom regions of the assemblies predicted by the two models, which are not yet fully developed and have significantly different velocities due to the difference in flow areas. In the detailed model, solid components restrict the flow area, and the instrument tubes offer the largest hydraulic diameter through the fuel assemblies. These two aspects of the assemblies are not captured in the homogenous model, because of its lack of solid components. This leads to the homogenous model overpredicting temperatures at lower elevations.

At mid-elevation (Fig. 4.9b), consistent patterns of temperature differences between all assemblies are observed. Very small temperature differences between the models are obtained in the center of the assemblies with the largest differences seen along the periphery of the assemblies. This may be because the homogenous model equally distributes the heat generation throughout the fuel assemblies, while the detailed model confines the heat generation to the fuel pellets with the guide tubes being hollow and not generating heat. There are more guide tubes in the central portion of the assembly than in the periphery (see Figure 4.1a) leading to less heat density in the center and more on the periphery of the detailed model compared to the homogenous model. The higher local heat generation in the periphery of the fuel assemblies in the detailed model leads to higher temperature predictions in the fuel rods.

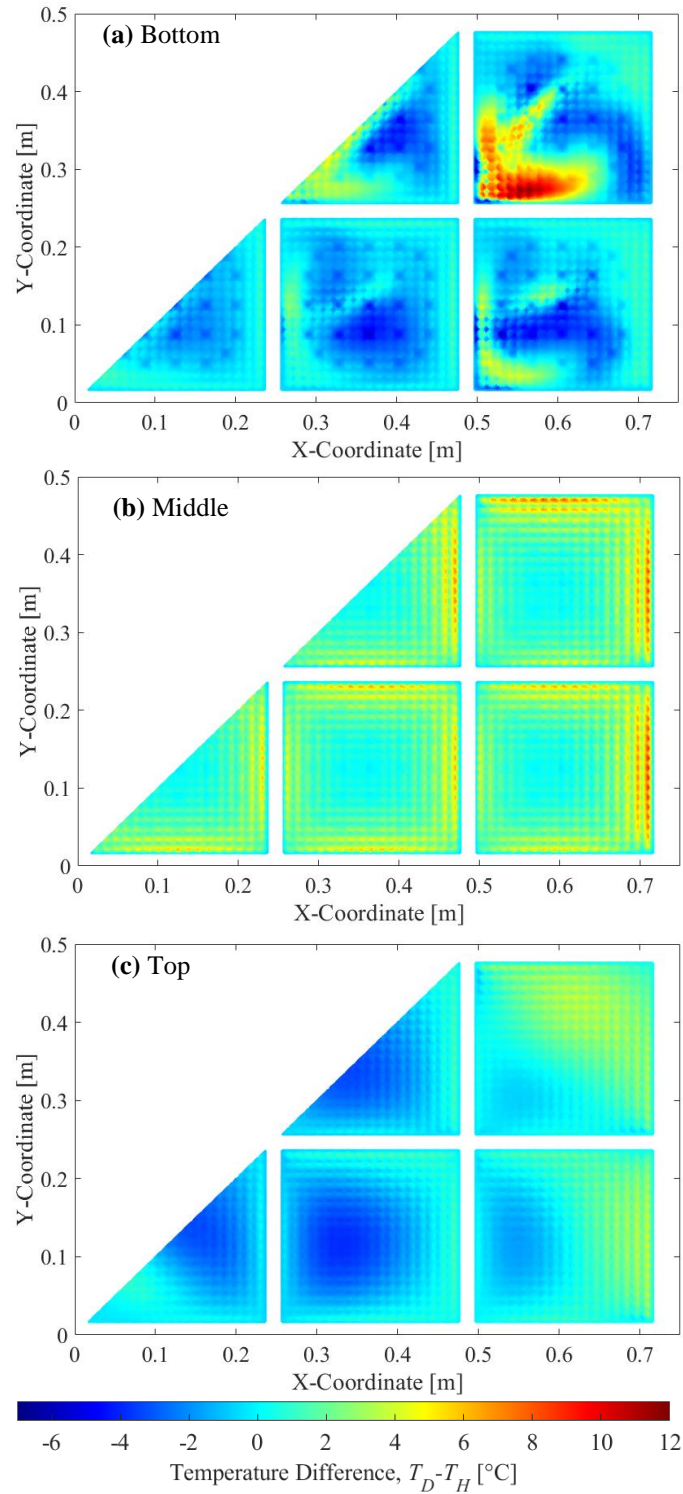


Figure 4.9. Contours of the temperature difference between the detailed and homogenous models at three axial locations, (a) bottom ( $z = -0.007$  m), (b) middle ( $z = 2.134$  m), and (c) top ( $z = 3.745$  m).

At the top elevation (Fig. 4.9c), temperatures are relatively similar between the modeling techniques, because the flows at this location are developed and there are several inches of space between the active fuel region and the plug. This causes a more uniform distribution of temperature in the detailed model similar to the homogenous model.

The temperature differences of the mid-elevation plane are the most representative of the differences seen throughout the majority of the length of the fuel assemblies because the active fuel region represents 95% of the assemblies' axial length and the small hydraulic diameter of open flow regions (in the spaces between the rods) leads the flow to develop quickly.

Figure 4.10 shows a point-to-point comparison of temperature prediction in the homogenous model as a function of temperature predicted in the detailed model. These temperatures are plotted for the 5 million data points extracted from the 27 axial planes. The points are colored by axial location and the best-fit line equation with the 95% standard error of the estimate is shown. If there was perfect agreement between the models, all points would lie on the  $T_D = T_H$  diagonal solid line. Dashed horizontal and vertical lines for the middle 50% of the data are shown for each model. The best-fit line and standard error indicate that the homogenous model recreates the results of the detailed model very closely, with a slope value close to 1, and a 95% standard of the estimate of 3.2°C. There are larger deviations associated with the undeveloped flow structures at the lowest elevations and temperatures, which represents a very small portion of the data. There is a significant amount of data overlap around  $T_D = T_H$  across all elevations and temperatures. The spread of the data narrows with the increase in

temperature, signifying that the homogenous model predicts even more closely the detailed model results at higher temperatures.

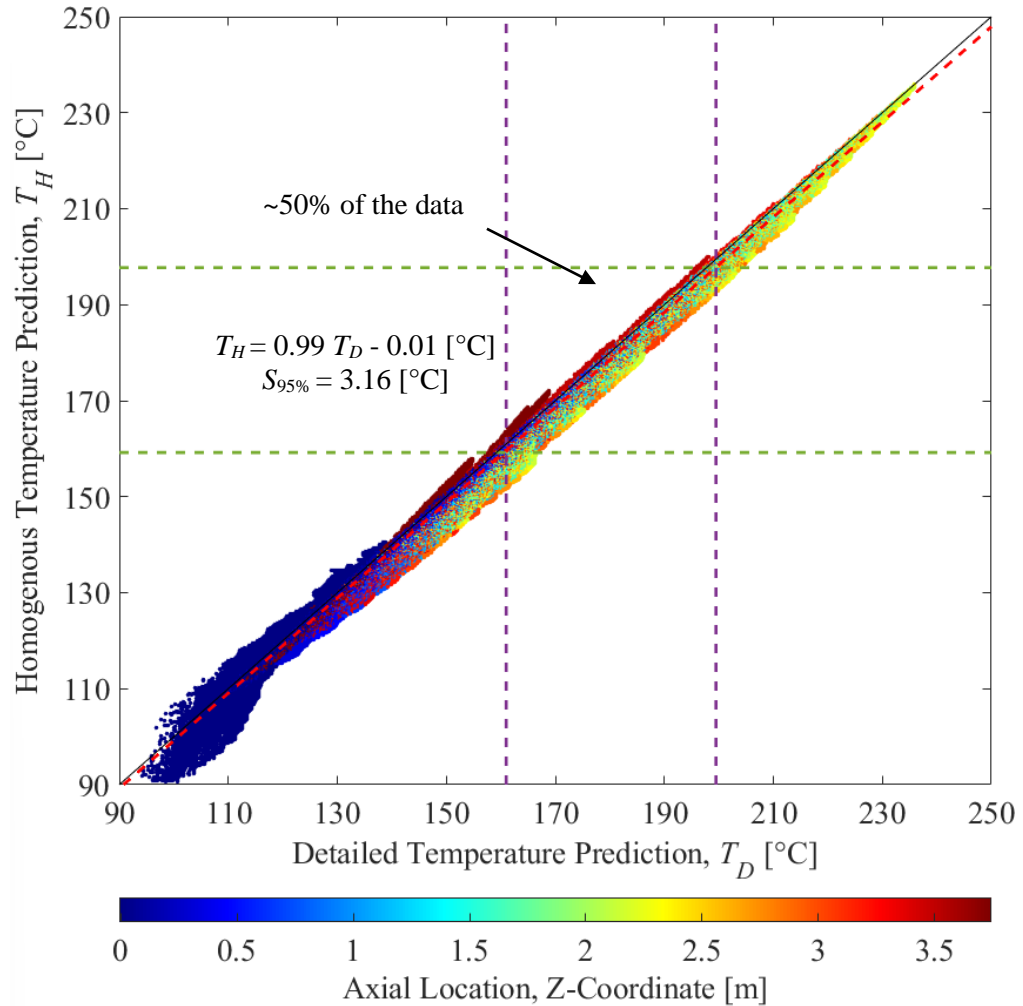


Figure 4.10. Domain point-to-point temperature comparison between detailed and homogenous models.

Figure 4.11 shows the probability distribution functions (PDFs) of each fuel region component (fuel, cladding, or helium) for the detailed and homogenous models. These PDFs encompass all the temperature data points of the fuel regions (not just the 27 planes) for both models. The distinction between the different fuel region components in the homogenous model is made possible because the same mesh is used for both the

detailed and the homogeneous models. However, when using the homogenous technique, this distinction is often not possible. This comparison on a component basis is conducted to show how the homogenous technique can predict the temperatures at different locations. The temperatures in Fig. 4.10 are grouped into 5°C bins with the temperature attributed to the upper bin for clarity. For the homogenous model components, the temperature is attributed based on the location of where the component would be relative to the detailed model. The temperature distributions of each component are similar, both within the models and between models. The elements attributed to the fuel are more likely to predict higher temperatures than cladding or helium in both models and are most apparent in the temperature range of 170 to 210°C. This is more pronounced in the detailed model than the homogenous model, likely because the heat generation is concentrated in the fuel rods. The shape of the distributions is roughly normal, though slightly skewed left, with a median of 181.5°C in the detailed model and 179.8°C in the homogenous model. The detailed model predicts that the middle 50% of temperatures fall between 161.0 and 199.5°C, while the homogenous model predicts that same range to be between 159.2 and 197.7°C. Extending that range to cover the middle 95% of data yields to ranges of 124.5 to 223.9°C and 123.6 to 223.0°C for the detailed and homogenous models, respectively.

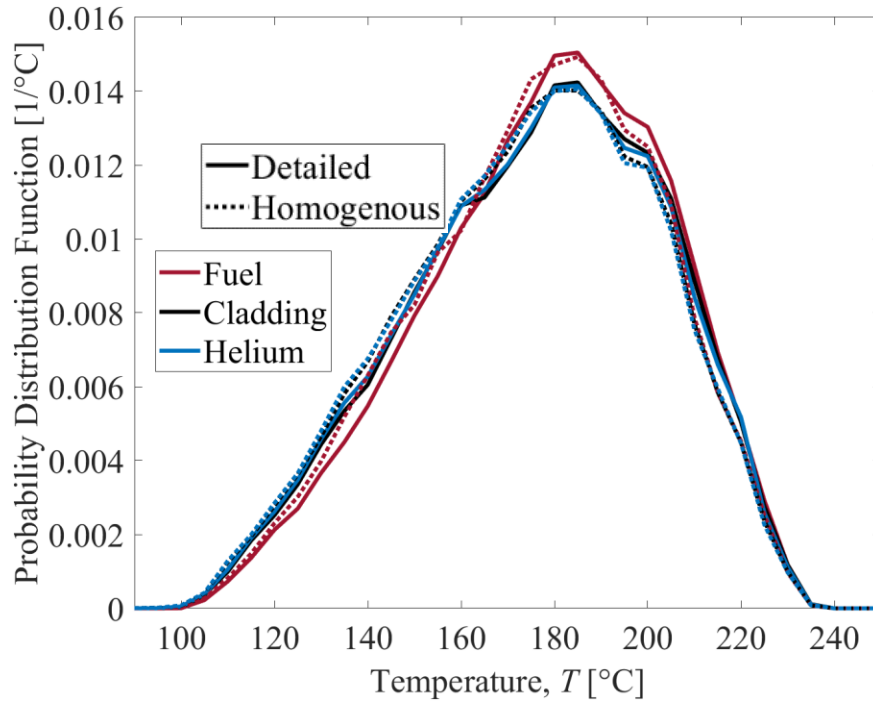


Figure 4.11. Probability distribution functions for each fuel region component (fuel, cladding, or gas), for both model types (detailed and homogenous).

## 5. Conclusion

In this work, a one-eighth 3D model of the TN-32B demonstration cask was constructed in the ANSYS package. The model accurately represented the fuel assemblies' components, i.e., the fuel pellets, claddings, instrument tubes, and helium regions. The same model mesh was used to represent the fuel assembly regions as heat-generating porous blocks. The properties of the homogenous model were derived from sub-models of a single, detailed assembly. The same highly structured, 40.8 million element mesh was used in both models and the only difference between the models was the representation of the fuel assemblies. The results from the detailed model were compared with data from the HBU demonstration project at 63 thermocouple locations within seven assemblies. The results showed that the detailed model predicted measured

temperatures within  $\pm 10^{\circ}\text{C}$  when buoyancy-induced natural convection was modeled. The effect of natural convection was also investigated, and it was found that it does not affect the peak cladding temperature greatly, but it does impact the temperature at high and low elevations within the fuel assemblies significantly. The results from the homogenous model were compared to the detailed model. The difference between models was characterized on an element-to-element basis in the fuel region. Temperature and flow prediction differences were found to vary with elevation and radial location within the assemblies. The 95% standard error of the estimate between models is  $3.2^{\circ}\text{C}$  with the largest deviations between models occurring at the bottom of the fuel assemblies where helium flow is undeveloped. Both models approximate the bounds for the middle 50% and 95% of data to be within  $2^{\circ}\text{C}$  of each other. This study showed that homogenous modeling of the fuel assemblies can accurately reproduce the fuel region temperatures predicted by detailed models without being overly conservative. The second part of this paper series will investigate if the homogenous modeling technique can be used to predict temperatures under vacuum drying conditions with the same accuracy compared to detailed modeling.

## **FUNDING**

This work was supported by the U.S. Department of Energy Office of Nuclear Energy University Program under award number DE-NE0008713 and by the United States Nuclear Regulatory Commission (NRC) under Contract NRC-HQ-84-16-G-0033. Ms. Nancy Hebron-Israel serves as the NRC award program manager.

## **REFERENCES**

- Akkurt, H., and A. Csontos. 2020. International Thermal Modeling Benchmark Description for a High-Burnup Used Fuel Dry Storage System: An Extended Storage Collaboration Program Activity. Palo Alto, CA: EPRI.
- Areva. 2002. TN-32 Final Safety Analysis Report (FSAR), Revision 2. Virginia Electric and Power Company.
- Bahney, RH, and TL Lotz. 1996. "Spent nuclear fuel effective thermal conductivity report." *Prepared for the US DOE, Yucca Mountain Site Characterization Project Office by TRW Environmental Safety Systems, Inc., July 11.*
- Brewster, Robert A, Emilio Baglietto, Eric Volpenhein, and Christopher S Bajwa. 2012. "CFD analyses of the TN-24p PWR spent fuel storage cask." ASME 2012 Pressure Vessels and Piping Conference.
- Creer, JM, TE Michener, MA McKinnon, JE Tanner, ER Gilbert, and RL Goodman. 1987. "The TN-24P PWR spent fuel storage cask: testing and analyses." *Pacific Northwest National Laboratory, Richland, WA, Report No. PNL-6054.*
- Csontos, A. 2020. High-Burnup Used Fuel Dry Storage System Thermal Modeling Benchmark: Round Robin Results. Palo Alto, CA: EPRI.
- Cuta, Judith M, and Harold E Adkins. 2014. Preliminary Thermal Modeling of HISTORM 100 Storage Modules at Diablo Canyon Power Plant ISFSI. Pacific Northwest National Lab.(PNNL), Richland, WA (United States).
- Das, Kaushik, Debashis Basu, Jorge Solis, and Ghani Zigh. 2010. "Computational Fluid Dynamics Modeling Approach to Evaluate VSC-17 Dry Storage Cask Thermal Designs." CFD for Nuclear Reactor Safety Applications, Workshop Proceedings, CFD4NRS-3, Bethesda, Maryland, USA.

- Durbin, Samuel, and Eric R. Lindgren. 2017. Thermal-Hydraulic Results for the Boiling Water Reactor Dry Cask Simulator. ; Sandia National Lab. (SNL-NM), Albuquerque, NM (United States).
- Dziadosz, D, EV Moore, JM Creer, RA McCann, MA McKinnon, JE Tanner, ER Gilbert, RL Goodman, DH Schoonen, and M Jensen. 1986. "The Castor-V/21 PWR Spent-Fuel Storage Cask: Testing and Analyses." *Electrical Power Research Institute, EPRI NP-4887, Project:2406-4*.
- EPRI. 2014. High Burnup Dry Storage Cask Research and Development Project – Final Test Plan. Palo Alto, California: Electric Power Research Institute.
- Fort, James A, Thomas E Michener, Sarah R Suffield, and David J Richmond. 2016. Thermal Modeling of a Loaded Magnastor Storage System at Catawba Nuclear Station. Pacific Northwest National Lab.(PNNL), Richland, WA (United States).
- Fort, James A, David J Richmond, Judith M Cuta, and Sarah R Suffield. 2019. Thermal Modeling of the TN-32B Cask for the High Burnup Spent Fuel Data Project. Pacific Northwest National Lab.(PNNL), Richland, WA (United States).
- Fort, James A, David J Richmond, Ben J Jensen, and Sarah R Suffield. 2019. High-Burnup Demonstration: Thermal Modeling of TN-32B Vacuum Drying and ISFSI Transients. Pacific Northwest National Lab.(PNNL), Richland, WA (United States).
- Hall, K, and G Zigh. 2019. NUREG/CR-7260, "CFD Validation of Vertical Dry Cask Storage System". Alden Research Laboratory. Inc.
- Hernandez-Avellaneda, Andres, Gonzalo Jimenez, Luis Rey, and Juan Carlos Martinez-Murillo. 2023. "Modelling fuel assembly flow nozzles in a spent nuclear fuel dry

cask using CFD codes." *Annals of Nuclear Energy* 181:109540. doi:  
<https://doi.org/10.1016/j.anucene.2022.109540>.

Higley, Megan. 2019. "Effect of Geometry Variation on Temperature Prediction in the TN-32 Used Nuclear Fuel Storage Cask." University of Nevada, Reno.

Higley, Megan, Miles Greiner, and Mustafa Hadj-Nacer. 2024. "Uncertainty quantification of thermal gap widths on internal temperatures in the TN-32B HBU demo cask." *Progress in Nuclear Energy* 169:105064. doi:  
<https://doi.org/10.1016/j.pnucene.2024.105064>.

Holman, JP. 1997. *Heat Transfer, 8th edition, New York*. New York City, New York: McGraw-Hill.

McKinnon, MA, JM Creer, CL Wheeler, JE Tanner, DP Batalo, DA Dziadosz, EV Moore, DH Schooner, MF Jensen, and JH Browder. 1987. The MC-10 PWR spent fuel storage cask: Testing and analysis. Pacific Northwest Lab., Richland, WA (USA); Virginia Power Co., Richmond ....

McKinnon, MA, RE Dodge, RC Schmitt, LE Eslinger, and G Dineen. 1992. Performance testing and analyses of the VSC-17 ventilated concrete cask. Electric Power Research Inst.

NRC, U.S. 2003. "Cladding considerations for the transportation and storage of spent fuel." *ISG-11, Rev. 3*.

Suffield, Sarah R, James A Fort, Harold E Adkins, Judith M Cuta, Brian A Collins, and Edward R Siciliano. 2012. Thermal modeling of NUHOMS HSM-15 and HSM-1 storage modules at Calvert Cliffs nuclear power station ISFSI. Pacific Northwest National Lab.(PNNL), Richland, WA (United States).

Trujillo, Corey. 2017. "Computational Fluid Dynamics Thermal Simulations of a Nuclear Fuel Canister During Drying." University of Nevada, Reno.

Yoo, Seung Hun, Hee Cheon No, Hyeun Min Kim, and Eo Hwak Lee. 2010. "Full-scope simulation of a dry storage cask using computational fluid dynamics." *Nuclear Engineering and Design* 240 (12):4111-4122.

## Chapter 5: Summary and Conclusions

---

The TN-32 dry storage cask is used to store thirty-two heat-generating spent nuclear fuel assemblies. It consists primarily of a basket that supports the assemblies within a 2.5 m diameter outer structure. The cask is designed to have a 4.78-mm helium-filled gap in between those components to facilitate assembly and to accommodate manufacturing tolerances and thermal expansion. Most of the heat generated by the SNF transfers through this gap, and its thermal conductivity is low compared to that of other cask components. As a result, temperature difference across this gap can be significant and strongly affect the peak cladding and other temperatures within the basket.

The thermal resistance across the gap is linearly proportional to its width. However, that width is difficult to predict due to uncontrolled manufacturing tolerances and potential shifting of the basket relative to the outer structure, as well as thermal expansion and other effects. Moreover, vacuum drying may cause the helium gas in the gap to become rarefied. This increases the conduction thermal resistance and temperature difference across the gap.

Two-dimensional simulations that accurately model the TN-32B cross section, including individual fuel rods, with a range of gap widths and gap non-uniformities were conducted. The simulations showed that, under storage (continuum) conditions, if the gap is effectively eliminated, or if the basket shifts relative to the containment boundary, the respective peak cladding temperatures decrease by as much as 40°C and 10°C compared to the design gap. Under vacuum drying (rarefied) conditions, these respective temperature decreases are 75°C and 37°C. These are important effects, especially when

considering the small size of the gap compared to the overall package diameter. This work indicates that uncertainty in the gap size leads to significant uncertainty in temperature prediction and that temperatures and their uncertainties increase for vacuum drying conditions.

Next, the same cask was modeled as a 3-D full, homogenous fuel region model. Simulation conditions provided by the ESCP HBU experiment project were employed. A global uncertainty quantification was used to estimate the uncertainty in temperature prediction at all experimental thermocouple locations due to uncertainty in the gap width of nine thermal gaps. Consistent overprediction of temperatures at lower elevations and underprediction at higher elevations indicated that some of the natural convection effects were not completely captured. Temperature was captured at 51 of the 63 thermocouple locations by the 95% confidence intervals with an average uncertainty of  $\pm 18^{\circ}\text{C}$ . Linear regression analysis was used to reveal the impacts of individual gaps on temperature prediction at each location.

Finally, the 3D full, homogenous fuel region model was modified into a one-eighth model with a detailed representation of the fuel regions. Information about flow paths between the supporting rails and the fuel assemblies was received and approximated by the model. The detailed model temperature predictions were compared with experimental data at all thermocouple locations. The temperature differences were within a narrow range of  $\pm 10^{\circ}\text{C}$ . Effective properties for the porous fuel region were derived from sub-modeling of a single assembly and used to homogenize the fuel regions for comparison with the detailed model. Temperature and flow predictions were compared throughout the fuel regions on an element-to-element basis at 5 million

locations. The data indicates that agreement between the detailed and homogenous model varies with axial and radial location due to the relative importance of heat transfer mechanisms. The standard error of the estimate between models is 3.16 [°C], indicating that the homogeneous model accurately predicted the temperatures of the detailed model.